Star Formation Rates and Metallicities in GOGREEN/GCLASS Clusters at $z \sim 1$

by

David Tibben

A thesis
presented to the University of Waterloo
in fulfillment of the
thesis requirement for the degree of
Master of Science
in
Physics

Waterloo, Ontario, Canada, 2026

© David Tibben 2026

Author's Declaration

I hereby declare that I am the sole author of this thesis. This is a true copy of the thesis, including any required final revisions, as accepted by my examiners.

I understand that my thesis may be made electronically available to the public.

Abstract

Star formation rate and metallicity are fundamental diagnostics for understanding galaxy evolution. The star formation rate traces how the stellar mass is changing over time, while the metallicity traces the chemical composition of the stellar mass and how far along the galaxy is through its evolution. With the stellar mass, star formation rate, and metallicity, one can measure the fundamental relation between those parameters and better understand the processes occurring in and around a galaxy.

In this thesis, I present follow up NIR spectroscopy of cluster galaxies at $0.8 < z < 1.4$ from the GOGREEN and GCLASS samples obtained with Keck/Gemini. We observe $\gtrsim 500$ galaxies, and visually identify and measure the Hα and [*N* II] emission lines. I am able to infer the star formation rates and metallicities for ~ 120 galaxies and determine cluster membership using distance and velocity dispersion. By comparing metallicity, SFR, and stellar mass between the field and cluster members, I am able to distinguish between different environment-driven quenching mechanisms.

I compare the sample with field galaxies at a similar redshift from the 3D-HST and MOSDEF surveys. I find consistent Hα equivalent widths and star formation rates relative to the field and a scatter about the SFMS of ~ 0.3 dex. I find that our cluster galaxies show enhanced $\log([\mathrm{N\,II}]/\mathrm{H}\alpha)$ ratios compared to our field sample of 0.083 ± 0.035 dex and an enhancement compared to literature field samples of 0.155 ± 0.043 dex at a fixed stellar mass of $10^{10.2}$ $\mathrm{M}_\odot$. At a fixed star formation rate of 10 $\mathrm{M}_\odot\, yr^{-1}$, I measure an offset in the $\log([\mathrm{N\,II}]/\mathrm{H}\alpha)$ ratio residuals of 0.09 ± 0.05 dex and 0.15 ± 0.04 dex between our field and the literature field samples respectively.

I interpret our measured enhancement of cluster line ratios and therefore metallicities compared to their field counterparts for evidence that the dominant quenching method may be a slow process such as strangulation. Furthermore, I compare our measured offsets with other samples across a range of redshifts of $0 < z < 2.5$. I find that other literature samples measured enhanced metallicities between $1 < z < 2$ and interpret this as evidence that strangulation may be the dominant environmental quenching mechanism in this epoch. At higher redshifts, the offset is flipped which can be explained by more pristine gas accretion in overdensities at $z > 2$ which would reduce the average cluster metallicity. At local redshifts, faster quenching processes such as ram pressure stripping become dominant, leading to a smaller enhancement in cluster metallicities.

Acknowledgements

First and foremost, I would like to thank my thesis supervisor for supporting me financially, mentally, and emotionally throughout the last two years. I appreciate the words of affirmation when I was not feeling proud, the mental support through traumatic events, and the opportunity to attend CASCA 2026 in Montreal.

This research has made use of data obtained from the Gemini South Observatory on Cerro Pachón, Chile and Keck II Observatory on Mauna Kea, Hawaii. I would like to thank the support staff who made those observations possible and I am grateful for the privilege of observing the Universe from places of great astronomical quality and cultural significance. I would also like to thank our collaborators within the GOGREEN collaboration who aided with interpretations and who provided me the opportunity to remotely observe using the Keck observatory.

I would like to thank the dense network of friends and colleagues at the University of Waterloo who provided a lovely community to work and research. I am proud of the community at the University of Waterloo who have created a welcoming and excellent research environment.

Dedication

This thesis is dedicated to the people who have supported me through my entire academic career: my love Alyssa, my amazing parents Jeff and Lianne, my two siblings Emily and Christopher, and my friends throughout my undergraduate and graduate careers. Thank you for your continued love and support.

Table of Contents

Author's Declaration ii

Abstract iii

Acknowledgements iv

Dedication v

List of Figures ix

List of Tables xvi

List of Abbreviations xvii

1 Introduction 1

1.1 General Background 1

1.2 Observables of Galaxy Evolution 1

1.2.1 Star Formation Rate 3

1.2.2 Metallicity 4

1.3 Measuring Star Formation Rate and Metallicity 5

1.3.1 Star Formation Rate 5

1.3.2 Measuring Metallicity 6

1.4 The $z \sim 1-2$ Epoch . . . 9
1.5 Galaxy Trends and Observations . . . 10
1.6 Environment . . . 12
1.7 Previous Work . . . 12
1.8 GOGREEN/GCLASS . . . 14
1.9 Outline . . . 15

2 Observations **16**
2.1 Data and Reduction . . . 16
2.1.1 Target Justification . . . 16
2.1.2 Data Acquisition . . . 17
2.1.3 Reduction Process . . . 17
2.1.4 Analysis Methods . . . 18
2.1.5 Cluster Membership and Selection . . . 22
2.1.6 Field Comparison Samples . . . 22
2.2 Results . . . 25
2.2.1 Consistent Equivalent Widths . . . 25
2.2.2 Consistent Star Formation Rates . . . 27
2.2.3 Enhanced Cluster Metallicities . . . 29
2.3 Discussion . . . 31
2.3.1 No Environmental Dependence with Hα EW and SFR . . . 31
2.3.2 Evolution in the Cluster Metallicity offset relative to Field . . . 34
2.3.3 Interpretation . . . 36
2.4 Conclusion . . . 37

References **39**

APPENDICES **62**

A Additional Plots **63**

A.1 Supplementary Informational Plots 63

A.2 Cluster Selection 66

A.3 Alternative Plots 70

A.4 Redshift Dependence within our Sample 74

B Aperture Corrections **76**

B.1 Continuum Corrections 76

B.2 Flux and EW Corrections 80

List of Figures

2.1 Information card generated for each galaxy with an $H\alpha$ detection. Top Left: Information about the galaxy, including measured flux information. Top Right: Image of the galaxy (K-band) with the axes being the position on the CCD. Middle: 1-dimensional spectrum which shows flux as a function of wavelength. The Hα and [N II] detections are clear in the spectra, and lie centred in the plot. Bottom: 2-dimensional spectrum from *Pypeit* with the Hα shown at the red vertical line with [N II] on either side of it. This image is in units of pixels, where the y-axis is the spatial pixel and the x-axis is the spectral pixel. The dark features on above and below the emission arise from the ABBA dither pattern used for sky subtraction. With this pattern, the "A" and "B" nod positions are differenced such that the source signal adds constructively at the central trace, while each position contributes a negative residual above and below. 19

2.2 We show the rest-frame velocity difference relative to the cluster, as a function of distance from the cluster centre for our work. Velocities are measured from the emission line redshifts obtained from our spectroscopy. The galaxies within the red box with dimensions ΔV = 3000km/s and $D = 1Mpc$ we define to be cluster members, while galaxies outside this box we define as field galaxies. 23

2.3 We show the redshift distribution for each dataset to which we compare our sample. Each data set covers a broad redshift range, which we limit for our comparison. 3D-HST has a maximum redshift of $z \sim 6$, so for readability we limit the axis ranges even though 3D-HST continues to $z = 0$ and higher than $z = 3$. Similarly, the data from ref. [94] spans a redshift range of $0 < z < 3.4$. The red, vertical dashed lines show the minimum and maximum redshift of our sample, so for most of the samples we limit to the hashes between these lines. Note that for ref. [94] and our data, we mark in red the cluster members determined by the velocity dispersion and distance from the cluster centre. MOSDEF has very few low redshift objects, and the field is dominated by $z > 2.0$ galaxies. On other plots in this paper, we limit the MOSDEF data to $z < 1.4$. 24

2.4 We show rest-frame Hα equivalent width as a function of stellar mass and compare our data to that of MOSDEF and KMOS-3D. We show the data points in the background, where the large red stars are our selected cluster sample, the small purple stars are our field sample, the blue diamonds are the KMOS-3D sample, and the blue triangles are the MOSDEF sample where KMOS-3D and MOSDEF are redshift limited ($z < 1.4$). The large foreground points represent the rolling means of each dataset, with KMOS-3D and MOSDEF combined into the large, blue diamonds. The error bars and shaded regions represent the 1σ errors on the means of the 4 mass bins. At all masses, there is no significant offset between our cluster and any field sample. 26

2.5 We show star formation rates as a function of stellar mass. Our cluster population is represented by the stars with black outline and a colourbar showing the galaxy redshift. Our field galaxies are represented by the gray stars, the MOSDEF sample at $z < 1.4$ as the blue triangles, and KMOS-3D ($z < 1.4$) as the blue diamonds. The green and purple lines are lines of best fit from ref. [154] which are field star formation rates calculated using $L_{UV} + L_{IR}$ observations. The darker purple line represents the redshift range $0.5 < z < 1.0$ while the green is $1.0 < z < 1.5$. As our Hα fluxes were corrected for dust, we applied a similar dust correction to MOSDEF and KMOS-3D with the same method. Our sample shows increasing star formation rates with increasing redshift and increasing stellar mass, and are fully consistent with both field comparison samples. We calculate the scatter of both our field and cluster samples to be ~ 0.3 dex, consistent with literature values. 28

2.6 We show our [N II] /Hα ratio as a function of stellar mass. Our cluster is represented by the red stars while our field sample are the smaller purple stars. We again show MOSDEF and KMOS-3D as the blue triangles and diamonds respectively, and combine the best fits together as the blue line. We show the lines of best fit and the associated 1σ errors. At low masses, our cluster data exhibits higher line ratios (metallicity) than our field sample, as well as the MOSDEF+KMOS-3D field sample. The significance of the offset with MOSDEF+KMOS-3D is $\sim 3.5\sigma$ and 2σ compared to our field sample at a fixed stellar mass of $10^{10.2}$M$_\odot$. 30

2.7 We show the difference between the KMOS-3D field model and our cluster and field samples as a function of star formation rate. In red, we show our cluster sample and in purple we show our field sample. The lines represent the lines of best fit and the 1σ confidence interval as the shaded region. We find significant (3.5σ) evidence for enhanced metallicities relative to the field MZR at a SFR of 10 M$_\odot$ yr^{-1}. Note that Hα is present on both axis and therefore produced correlated uncertainties. However, uncertainties on the measured SFR are small. 32

2.8 We show $[N\,\textsc{ii}]/H\alpha$ as a function of stellar mass, but we instead split the samples into different bins of Hα equivalent width. The colouration is the same as the previous plots, but we also introduce a $z \sim 0$ sample (SDSS) to increase the overall redshift range to observe any significant redshift dependence as redshift decreases. Hα equivalent width ranges of each bin are listed on the top of each plot. By splitting the data into equivalent width bins, we effectively eliminate the dependence of metallicity on equivalent width. MOSDEF is dominated by high equivalent width objects, and in the largest equivalent width bin we do see an offset. We find evidence of an offset in $[N\,\textsc{ii}]/H\alpha$ in each bin, with the significance increasing with increasing equivalent width. 33

2.9 We show the offset between $[N\,\textsc{ii}]/H\alpha$ in the field and cluster as a function of redshift for different samples over a wide redshift range of $0 < z < 2.5$. For each dataset, the offset was measured at a fixed mass of $M = 10^{10.2} M_\odot$. 35

A.1 Redshift parameter fit as a function of the GOGREEN catalogue redshift. Objects in black have spectroscopic redshifts from GOGREEN; blue points have a redshift measured from HST Grism; and red points have only photometric redshifts. The photometric redshifts have relatively large redshift uncertainties and have a scatter about the 1-to-1 line of $\sigma = 0.071$, while the grism and spectroscopic redshifts have a scatter of $\sigma = 0.004$ and $\sigma = 0.008$, respectively (excluding a spectroscopic extreme outlier at $z \sim 1.05$). 64

A.2 We show [O II] fluxes from [111] as a function of our measured Hα fluxes. The large scatter is likely dominated by differences in extinction [47]; the [O II] emission line also depends on metallicity. We show a measurement from [47], where they calculated $[O\,\textsc{ii}]/H\alpha = 0.48$, shown as the black dotted line. We compare with [111] in the discussion. 65

A.3 Histogram of the number of galaxies within various velocity bins. There is a modest population of galaxies with ΔV < 2000 km/s. We infer that using a ΔV ≤ 3000 km/s cut is a reasonable estimate for cluster members. 67

A.4 We examine the magnitude and significance of the offset in log([N II]/Hα) as a function of cut used. We show the magnitude and significance as the colour bar, with each grid square indicating a different cut. For example, for our cuts at x = 1.0 and y = 3000, the magnitude and significance of the offset is larger than if the cuts were at a larger value of x and y. 68

A.5 We examine the magnitude and significance of the offset in the residuals plot (Figure 2.7) as a function of cut used. We use the same colouration method as the previous plot. For both, our cuts at x = 1.0 and y = 3000 show a fairly large significance and offset. 68

A.6 We show the fit to our log([N II]/Hα) data for a variety of cuts. In red, we show our cluster with the current cuts. In purple, we show galaxies that we would expect to be part of the field; galaxies that have $D < 0.6$ Mpc *and* $\Delta V > 5000$ km/s. In green we show what we are currently using as the field, so everything not included in the red sample. The black shows transition galaxies, so galaxies that do not fit into the red or the purple. In blue we show the KMOS fit, and the cyan shows the fit we compare our results to. No matter the choice, we always see an offset between models and the error bars all overlap. 69

A.7 We show rest frame Hα + [N II] equivalent width as a function of stellar mass. Our cluster sample is shown with the red stars, while our field sample is shown in purple. We compare to the 3D-HST field sample shown as the gray background points, which is limited to the same redshift and mass range as our sample. We also show the data from [94] in blue, where we limit their sample to only cluster galaxies using the velocity dispersion. . . 71

A.8 We show Hα luminosity (uncorrected for dust extinction) as a function of stellar mass for our data, MOSDEF, 3D-HST, and work from [154] - which was calculated using 3D-HST data. The coloured stars with red outlines are our data, with the blue triangles representing the $z < 1.4$ MOSDEF sample. The green and blue lines are the Hα luminosities for two different redshift ranges from [154]. The results were consistent with the conclusions of [94], but [94] had a slight elevation of SFR. We find that our Hα luminosities are consistent with all the field samples. Furthermore, the redshift effect present in the lines from [154] is also present within our sample, with the higher redshift objects on average possessing slightly higher Hα luminosities than the low redshift galaxies. 73

A.9 We show $[N\,\textsc{ii}]/H\alpha$ as a function of stellar mass in two different redshift bins on either side of $z = 1$ and colour-coded by cluster membership. The red points are cluster galaxies while the purple points are field galaxies. We see an offset between $[N\,\textsc{ii}]/H\alpha$ for the field and cluster samples at higher redshifts of 0.13 ± 0.06 measured at $10^{10.2}$ $M_\odot$. We see a similar offset to that of [89]. 74

A.10 We show SFR as a function of stellar mass in two different redshift bins on either size of $z = 1$ and colour-coded by cluster membership. The red points are galaxies within the cluster while the purple points in the field. We see no evidence for an offset in SFR width between the cluster and field galaxies in either redshift bin within our sample. 75

B.1 We show our continuum magnitudes at $H\alpha$ measured directly from the spectra as a function of broad-band total magnitudes from GOGREEN. The points in red correspond to galaxies with Hα lies in the H-band. On the x-axis is the corresponding H-band magnitude for these points, while the rest of the points in black we use the corresponding J-band magnitudes. GOGREEN does not have H-band magnitudes, so we converted to H-band by fitting a line to a colour-colour diagram ($H_{grism} - J_{grism}$ vs $J_{grism} - K_{GG}$ and using the J and K magnitudes of GOGREEN to predict the H-magnitude. Dashed line is the 1-to-1 line. The continuum flux (c_D) was calculated using the linear MCMC fit of the continuum around Hα, and converted to an AB magnitude. When excluding the extreme outliers, the ground-based magnitudes from GOGREEN are systematically ~ 0.20 magnitudes larger than the continuum magnitudes measured at Hα with a scatter of $\sigma = 0.366$. We attribute this difference to the effect of our bright emission lines within the transmission window of the filters used for the ground-based magnitudes. In other words, because Hα is extremely bright compared to the continuum, this would inflate the magnitudes such that the broadband magnitude is larger than our magnitudes calculated using the continuum flux at Hα. 77

B.2 We show our continuum flux correction factor as a function of broadband magnitude. The mean continuum correction factor is $\beta_c = 1.32$ with a standard deviation about this mean of $\sigma = 0.53$. We interpret this correction as the contribution from the large flux added to the broadband magnitude by the Hα emission line and therefore scale by a factor of $1/(1 + EW/\Delta\lambda)$. We show $f_{BB}/f_c(1 + EW/\Delta\lambda)$ on the y-axis, which should be scattered around 1 if this is the only correction needed. We decide to apply the mean correction factor to every galaxy, which will shift our equivalent widths down by a factor of $1/\beta_c$. 78

B.3 We experimented with various methods of measuring the continuum. This plot shows the broad-band continuum estimated with *synphot* compared with the continuum fit at Hα we obtain from MCMC (Figure B.1) For spectra with large skyline residuals or other systematic uncertainties, *synphot* produced larger deviations from the photometric magnitudes. However, for the objects that were successful with *synphot*, the measurements were consistent between the methods, as demonstrated with the strong correlation in this plot, with a scatter of $\sigma = 0.15$. 79

B.4 When comparing our Hα+[N II] fluxes with the Grism sample from [94] for duplicate objects, our flux is lower. We interpret this as an aperture effect.On average, the fluxes from [94] are higher by factor of $\bar{\beta}_{H\alpha} = 1.52$, or ~ 0.5 mag. The scatter is $\sigma = 0.242$. 81

B.5 Our Hα+[N II] line flux is shown after applying the flux aperture correction as a function of blended line flux from the HST grism data.We multiply our fluxes by $\bar{\beta}_{H\alpha} = 1.52$ to scale our fluxes to match that of the HST Grism fluxes. By definition, the difference in the means is now zero, while the scatter is unchanged. We show an orange line to indicate the old mean of the fluxes, while the 1-to-1 line is the new mean after applying corrections. 82

B.6 Our observed Hα+[N II] equivalent widths (uncorrected for any aperture effects) are lower than those measured from the HST grism data by a factor of $\bar{\beta}_{EW} = 1.16$ (without excluding outliers). Since Figure B.4 shows our slit-based line fluxes would need to be multiplied by an average factor of $\bar{\beta}_{H\alpha} = 1.52$, this implies that the aperture correction is larger enough to correct for this offset, potentially with some slight over correction. With the outliers included, we measure a dispersion of $\sigma = 0.248$. 83

B.7 We show our measured equivalent width after applying the continuum corrections and the flux corrections to our data. We multiply by $\bar{\beta}_{H\alpha}/\beta_c$ which shifts our equivalent widths up to closely align with the 1-to-1 line against the equivalent widths from [94]. 84

List of Tables

2.1 Summary of observations for Keck MOSFIRE and Gemini Flamingos 2. Higher cluster redshifts were observed in a longer wavelength filter, such that any $H\alpha$ detections will fall on the detector. 17

2.2 We show a summary of the parameters fit with *emcee* with the priors used and any additional comments about the fitting process. 20

List of Abbreviations

AGN active galactic nuclei 6, 10, 22

FMR Fundamental Metallicity Relation 4, 11, 13, 31

GCLASS Gemini Cluster Astrophysics Spectroscopy Survey 14

GOGREEN Gemini Observations of Galaxies in Rich Early Environments 14

Hα hydrogen alpha 5, 6, 10

IMF initial mass function 5, 6, 21

IR infrared 5, 6, 10, 14

ISM interstellar medium 4, 10, 12

KMOS K-band Multi Object Spectrograph 13

MOSDEF MOSFIRE Deep Evolution Field 13

MOSFIRE Multi-Object Spectrometer For Infra-Red Exploration 14

MZR mass-metallicity relation xi, 4, 11, 14, 32

SFMS star forming main sequence 27

SFR star formation rate xi, 5, 6, 10–14, 21, 31, 32

SpARCS Spitzer Adaptation of the Red-sequence Cluster Survey 14

UV ultraviolet 5, 6

Chapter 1

Introduction

1.1 General Background

A galaxy is a system of stars, gas, dust, and dark matter bound together by gravity. Galaxies come in many different sizes and shapes, and can form over a wide range of stellar masses. Most galaxies have somewhere around 100 million to 1 billion stars, but they can be much smaller or much larger than this. While we can only observe galaxies by looking at the emitted light, most of the mass ($\sim 85 - 90\%$) within a typical galaxy is in the form of dark matter, with everything else making up the remaining fraction (e.g. stars, gas, dust, black holes).

Studying galaxy evolution allows us to look back through cosmic time and get snapshots of galaxies in every stage of evolution. We can observe galaxies far away and long ago and trace how they evolved to become the galaxies we see today, including our home galaxy, the Milky Way.

1.2 Observables of Galaxy Evolution

At the highest level, galaxies are characterized by their shape and structure, or morphology, such as spirals, ellipticals or irregular galaxies. Inside these classifications, there are subclasses based on the shape such as the presence of an extended bar-like central bulge (barred spirals) or the ellipticity of an elliptical galaxy (ratio of minor and major axes). While the estimate of the number of galaxies in the Universe is on the order of trillions, each galaxy is governed by the same physical laws and processes.

Structure and morphology are just some of the key measurable characteristics of galaxies. Beyond the shape of a galaxy, galaxies are also characterized by their luminosity and surface brightness, which describes how much light they emit. Galaxies emit light across the entire range of the EM spectrum, so galaxies have luminosities for each band such as X-ray luminosity and optical luminosity. These bands can be further divided into sections of wavelength. For example, the optical spectrum is divided into colours from red to violet. In astronomy, colour usually refers to different filters which have a specific wavelength of light they let through to the detector. For example, the filter "F814W" is a wide filter that lets through a range of wavelengths centred on 814nm (700nm $\lesssim \lambda \lesssim$ 950nm) and is a red - near-infrared filter. A colour index can be obtained by subtracting the magnitude measured through one filter from the magnitude measured through another. For example, if you measure a galaxy's magnitude through a blue filter and a red filter, the difference between the two $(B - R)$ tells you how blue or red the galaxy appears. The colour can be an important observable for stellar evolution as it is directly related to temperature and age when combined with the luminosity, and also galaxy evolution as there are general trends with observables and colour. For example, galaxies that emit more blue emissions are generally more active, younger, and spiralled than redder galaxies which are older, less active, and generally elliptical. [64]

The mass of a galaxy is crucial for understanding its formation and evolution. The mass is split into different components; stellar mass, gas and dust, and dark matter with the latter dominating the total mass. To measure the stellar mass, we measure the total spectral energy distribution of the galaxy. Combined with the total luminosity (which also requires the distance) of the galaxy, we can fit to models to infer the mass to light ratio and obtain a stellar mass [32, 38]. When measuring the mass of the gas within a galaxy, there are different methods for the various phases and temperatures the gas can be in. The phases of gas within a galaxy are molecular (H_2), atomic (H), and ionized (H^+). Dense, cold ($\sim 10 - 20$K) molecular hydrogen in star forming regions is extremely difficult to detect at these temperatures, so tracers like CO must be used [16]. For atomic, neutral hydrogen, the 21cm hydrogen line is the primary method of measurement [63]. Ionized gas can be detected through hydrogen recombination lines and at higher temperatures, the gas itself emits detectable emissions such as X-ray Bremsstrahlung radiation in extreme ($10^6 - 10^7$K) environments [103]. Measuring the amount of dust within a galaxy relies on the absorption of UV/optical starlight and subsequent re-emission in the mid- to far-infrared wavelengths. This dust absorption can also be a significant challenge for other measurements that depend on optical/UV light [44]. The mass of the dark matter halo can be calculated using a galaxy's interaction with the environment, such as through an orbit with another galaxy or through gravitational lensing which occurs when a background

galaxy's light gets bent around a massive foreground galaxy which allows the measurement the lens's mass [83]. One could also use rotation curves to measure the mass of a galaxy. For a rotating system such as a galaxy, we would expect the orbital velocity to decrease with increasing distance, similar to the planets in our solar system. However, this velocity does not drop off but instead remains roughly constant. This cannot be accomplished by stars and gas alone, so this effect is attributed to dark matter [152]. This works for spiral galaxies, but for elliptical galaxies the stars are in random orbits so we instead use the velocity dispersion of the stars' orbits and use models based on the virial theorem to calculate how much mass is present to keep those stars gravitationally bound [19].

Not only is the total mass important, but also the rate at which the mass is changing and the chemical composition of the mass. The mass of a galaxy can change either through star formation or through mergers with other galaxies. At $z < 2$, in situ star formation is widely believed to be the dominant growth mode for galaxies [84], so measuring the rate of star formation is a tracer of the evolution of stellar mass through time, or the evolution of the galaxy. Metallicity is the chemical composition of the galaxy, where anything heavier than hydrogen and helium is considered a metal. Metals are generated primarily through the deaths of stars, so metallicity is a "cosmic clock" which tracks how far along the galaxy is throughout its evolution, as more metals indicates more generations of stars have been born and subsequently died.

1.2.1 Star Formation Rate

Star formation is the process by which dense regions collapse to form stars. In a simple model, an interstellar cloud of gas will remain in hydrostatic equilibrium as long as the energy resisting collapse (thermal/kinetic) is in balance with the gravitational potential energy. This is known as the Virial Theorem [31]. If the outward energy and gravity of a cloud of gas are balanced, the cloud is said to be in virial equilibrium and is stable. If the outward energy dominates, the cloud will disperse and suppress star formation. If gravity dominates, the cloud may collapse and potentially form stars which also requires the energy transferred from the gravitational potential to be radiated away. This is under the assumption that the only energy resisting collapse is the thermal/kinetic energy. In real systems, there are more effects at play. Turbulent motions within the gas add to the kinetic energy that resists collapse, while magnetic fields caused by the movement of charged particles within the cloud can resist compression [139, 155].

The most favourable place for star formation to occur is within the cores of giant molecular clouds. These clouds are extremely cold ($10-30$K) meaning there is already very

little thermal pressure resisting gravitational collapse [135]. While the turbulent motion within a cloud generally resists collapse, these motions can locally create overdensities which can trigger collapse in pockets within the cloud.

1.2.2 Metallicity

Metallicity can refer to the chemical composition of individual stars (stellar metallicity) or the metallicity of the gas within a galaxy (gas-phase metallicity). While the gas-phase and stellar metallicity are closely related, they are different from one another [160]. The gas-phase metallicity traces the current state of the gas being used for star formation, while the stellar metallicity integrates the entire star formation history. For faint, distant galaxies, the stellar metallicity is difficult to measure so we must measure the gas-phase metallicity instead.

Metallicity arises from the products of nucleosynthesis. Throughout a star's life on the main sequence, they fuse hydrogen and helium into heavier elements via nuclear fusion. Generally, stars produce all the elements below iron on the periodic table through this method, as elements past iron are no longer favourable for this reaction to occur [46, 99]. When stars die, they release all these heavy elements into the interstellar medium (ISM) where it gets recycled into new stars. The later generations of stars will have more metals than previous generations, and can be characterized by their metallicity [60, 75]. Because iron is the final element in main sequence nucleosynthesis, stellar metallicity is commonly shown as the ratio of iron to hydrogen, or Fe/H.

Within galaxies, the gas-phase metallicity is a sensitive tracer of the baryon cycle [42, 157, 30]; the cycle of gas and dust in and around a galaxy. Star formation within the galaxy uses up gas and produces metals. Energy injection from supernovae and AGN jets can heat gas significantly and expel it from the galaxy through outflows. Gas can also be accreted into the galaxy by gravity through inflows, which can be pristine gas or even the re-accretion of the metal-rich gas expelled by the outflows [11, 112]. The processes that drive the baryon cycle can all affect the gas-phase metallicity in different ways, whereby star formation enriches the interstellar medium (ISM) over time, inflows and outflows can enrich or dilute the ISM depending on the metallicity of the gas going in or out. The strength of these processes are strongly dependent on the stellar mass and star formation rate which gives rise to two relations: the mass-metallicity relation (MZR) and the Fundamental Metallicity Relation (FMR). More on this in Section 1.5.

1.3 Measuring Star Formation Rate and Metallicity

1.3.1 Star Formation Rate

There are various ways to trace and estimate star formation rate observationally. Each diagnostic has its own advantages and disadvantages and more accurate results are obtained using a combination of various methods, although this is often impractical.

Ultraviolet Radiation

The most direct indicator of star formation is ultraviolet (UV) radiation. O-type, B-type and some A-type stars have peak emissions in the UV and have main-sequence lifetimes on the order of $\sim$ 100Myr. Therefore, the number of O and B type stars and consequently the UV luminosity of a galaxy is directly proportional to the current star formation rate. This traces star formation rate on the same timescales as the star's lifetime, so on the order of $\sim$ 100Myr.

While most of the UV luminosity is dominated by massive, short-lived stars, the total mass of newly born stars is dominated by stars with lower masses. Therefore, the conversion from UV luminosity to star formation rate (SFR) is sensitive to the assumed initial mass function (IMF) [67, 87]. In addition to the dependence on the unknown IMF, UV is highly sensitive to dust extinction [23]. UV is easily absorbed by dust, where the light gets re-emitted in the mid- and far-infrared bands. Because of this re-emission, the sum of the UV and IR luminosities can provide a robust measure of star formation rates [87]. Furthermore, the UV radiation that is attenuated by dust also photoionizes surrounding hydrogen, which later recombines and can also trace the star formation rate [67].

Hydrogen Recombination Lines

The most massive of these stars, O-type and massive B-type stars produce UV radiation with sufficient energy to ionize hydrogen, creating H II regions [66]. The ionized hydrogen can later recombine through well-defined emission pathways, the brightest of which is hydrogen alpha (Hα) at 6563 Å [69]. The lifetimes of the most massive stars are shorter than the general population of stars emitting UV radiation, so the Hα emission line traces star formation rates associated to the main-sequence of the largest of stars, on a timescale of $\sim$ 10Myr. Hα is also well-calibrated [e.g. 66], making Hα emission one of the best tracers of near-instantaneous star formation rate [67].

Hα shares similar disadvantages to UV radiation. Because only the largest O-type and massive B-type stars produce enough energy for photoionization of hydrogen, Hα is more sensitive to the shape of the IMF. For very small galaxies, the chosen IMF could predict very few massive stars, leading to larger uncertainties in the SFR-Hα relation [26, 81]. Hα is also significantly affected by dust. For both UV and Hα, the H II regions producing the ionizing radiation and consequently the Hα emissions are inherently within dusty environments [24, 28].

Ionizing radiation can also be produced from sources not associated with star formation. One common source is from the active galactic nuclei (AGN) which can significantly increase the Hα emission of a galaxy [6]. For non-spatially resolved galaxies, this is difficult to distinguish from the emissions in star forming regions [73]. AGN widen the spectral lines of Hα due to Doppler broadening caused by the rapid movement of gas around the galactic centre where it can blend with the flanking [N II] doublet which complicates spectral fitting [6, 117]. The [N II] doublet can also be problematic for low-resolution spectroscopy, as the flux from both [N II] lines and the Hα line are blended together. For low-resolution Hα studies, this must be accounted for [148].

Other Emission Lines

As the Hα emission line is at a very red wavelength of 6563 Å, the emission feature could be redshifted out of an atmospheric transmission window and into the infrared [66, 102]. If other indicators are unavailable, sometimes other emission lines can be used as tracers for SFR. A strong emission feature that is blueward of Hα is the [O II]λ3727 forbidden line doublet [53, 68]. While the luminosities of forbidden lines do reflect the UV radiation, they also depend on the ionization state and metallicity of the interstellar medium and therefore do not directly measure the UV luminosity produced by the massive stars [72]. Although not as robust as the other indicators, [O II] emission can be calibrated against Hα to trace the SFR. However, since the SFR-[O II] relation is calibrated through Hα, the uncertainties associated with the Hα relation are compounded along with intrinsic uncertainties associated with [O II], including significant dust attenuation [72, 102, 54].

1.3.2 Measuring Metallicity

There are various ways to trace and estimate the metallicity within galaxies, each with its own advantages and disadvantages. Following hydrogen and helium, oxygen is the third most abundant element in the Universe. Because oxygen is created through stellar

nucleosynthesis, the [O/H] ratio is often used as a measure of the metallicity within galaxies [91, 74].

The physical process that allows metallicity to be measured is the same for every method. Within the H II regions of galaxies, the electrons released by the ionization of hydrogen can strike other atoms nearby. These electrons can excite bound metallic electrons (such as oxygen), which eventually decay back into a ground state, releasing a photon through a forbidden transition. Through these transitions, one can estimate the metal abundances within H II regions, where the intensity of the forbidden line indicate higher metallicities [114, 113].

The Direct Method

The most direct method of measuring the metallicity of galaxies is using the electron temperature, or the T_e method. The photoionization of the gas heats it, while the collisional excitation of metal ions by electrons and subsequent photon emission from de-excitation cools the gas. The more metals present, the cooler the gas will become [71].

The direct method takes advantage of auroral line emissions within H II regions [61]. One common auroral line used is of doubly ionized oxygen at 4363 Å. The ratio of this line to other emission lines from oxygen gives

$$R \equiv \frac{[O\textsc{iii}]\lambda 4363}{[O\textsc{iii}]\lambda 4959, 5007} \quad .$$

However, auroral lines are extremely faint in most galaxies. This is the main limitation of the direct method. The direct method is most accessible in low-metallicity, high-temperature systems, but it fails in metal-rich systems where the auroral line becomes too faint as the gas cools more efficiently at higher metallicity [71, 4]. For $z > 0.5$, these lines are shifted into the near-IR, making direct measurements of metallicity far more difficult. Despite this limitation, when T_e is measurable it provides a direct measurement of the metallicity and is used to calibrate other tracers of metallicity. JWST has also allowed for the direct method to be applied more easily [36, 132].

When the direct method is unavailable, we use strong line metallicity proxies that trace O/H.

R23

The $R23$ method was first introduced by Pagel et al. (1979) and Alloin et al. (1979) [114, 3]. It is defined as:

$$R_{23} \equiv \log\left(\frac{[O\,\textsc{ii}]\lambda 3727 + [O\,\textsc{iii}]\lambda(4959, 5007)}{H\beta}\right) \quad .$$

The R23 method attempts to capture the total oxygen emission in an $H\textsc{ii}$ region. The ratio is normalized by Hβ because $[O\,\textsc{ii}]$ scales with both oxygen abundance and the ionizing photon flux, while $H\beta$ is a recombination line that traces only ionizing flux. This normalization cancels the contributions from the ionizing photons, and leaves only the signal from oxygen abundance [95]. This method is sensitive across a wide range of metallicities due to the strength of the lines used, which makes it a great method for large surveys [145] and to higher redshifts [134, 37]. This method does have some significant downfalls. R23 spans a long baseline of over 1200 Å, so it is susceptible to differential reddening and dust extinction effects [71]. While these issues are significant, the main limitation of this method is that it is double valued, meaning a value of R23 can correspond to two different metallicities. At low metallicities, R23 monotonically tracks the metallicity, whereby increasing metallicity corresponds to more oxygen emissions [76, 70]. However, there is a turnover point where the relationship flips and decreasing R23 corresponds to increasing metallicity. At high metallicity, efficient cooling lowers the electron temperature, suppressing the collisional excitation and therefore lowering the emission line fluxes despite increasing oxygen abundances [71]. Much calibration work has been done to break this degeneracy, and the R23 is well-used and characterized throughout the literature across a wide range of redshift [145, 134, 35, 37].

N2

Another commonly used proxy for metallicity is N2 defined as

$$N2 \equiv \log\left(\frac{[N\,\textsc{ii}]\lambda 6584}{H\alpha}\right) \quad .$$

The N2 method traces the abundance of ionized nitrogen rather than oxygen directly. The ratio is again normalized by a Balmer line to cancel the effects of the ionizing photons on the ratio. Furthermore, $[N\,\textsc{ii}]$ and Hα are separated by only ~ 20 Å, making the ratio invariant to the flux calibration as well as dust. $[N\,\textsc{ii}]$ also has a lower ionization energy

than [O II], meaning that N2 is better suited for the lower temperature, high metallicity environments. The largest problem with using the $[N\,\textsc{ii}]/H\alpha$ ratio to infer the O/H ratio is that it requires assuming that the N/O ratio is roughly constant [118]. At low metallicities, nitrogen is primarily produced through the triple-α process independent of the initial metallicity, and $[N\,\textsc{ii}]/H\alpha$ becomes insensitive to changes in O/H [59, 149]. At higher metallicities, despite a lower ionization energy than [O II], the $[N\,\textsc{ii}]/H\alpha$ ratio gets "saturated," as more efficient cooling in high metallicity environments suppresses the collisional excitation of [N II] even if the nitrogen abundance is increasing [70]. As a consequence of saturation, the $[N\,\textsc{ii}]/H\alpha$ ratio is also double valued such that the same $[N\,\textsc{ii}]/H\alpha$ ratio can correspond to two different metallicities on either side of a turnover [71]. As a result, $[N\,\textsc{ii}]/H\alpha$ is only reliable at intermediate metallicities ($8.3 \lesssim 12 + \log(\mathrm{O/H}) \lesssim 8.7$), where the ratio is still tracking O/H and where [N II] remains collisionally excited [118, 71]. The relationship to O/H is roughly linear for $\log([\mathrm{N\,II}]/\mathrm{H}\alpha) < -0.4$ [118].

O3N2

At higher metallicities, the strength of OIII decreases with increasing metallicity while $[N\,\textsc{ii}]$ saturates. To break this degeneracy, we can combine the N2 and R23 methods with O3N2 [3, 118].

$$\mathrm{O3N2} \equiv \log\left(\frac{[\mathrm{O\,III}]\lambda5007/\mathrm{H}\beta}{[\mathrm{N\,II}]\lambda6584/\mathrm{H}\alpha}\right)$$

Because each ratio pairs with an emission line with a spectrally adjacent Balmer line, the O3N2 relation is fairly invariant to dust extinction and flux calibration errors [118]. O3N2 is sensitive to metallicity over a wide metallicity range because it combines the ranges of two different ratios. O3N2, however, is very sensitive to the ionization conditions, meaning that two H II regions with the same metallicity but different ionization parameters will have different O3N2 measurements which introduces a lot of scatter in the relation to metallicity [131, 74, 91]. Nevertheless, the O3N2 method is a useful diagnostic for determining the metallicity in H II regions.

1.4 The $z \sim 1 - 2$ Epoch

For this work, I am interested in redshift $z \sim 1$. The epoch up to $z \sim 2$ is an important time in the Universe's development. The redshift range corresponds to approximately $8 - 10$

billion years ago, and it is a time when the star formation rate density of the Universe was at its peak. From $1 \lesssim z \lesssim 2$, the star formation rate density decreased by roughly one full magnitude, so this epoch contains the decline in that star formation rate. For metallicity, the ISM is being enriched over this epoch, so the evolution from $z \sim 2$ to the Universe today shows the integrated history of gas feedback, accretion, and outflows [87].

In this epoch, there are different challenges with making measurements of both SFR and metallicity. One significant challenge is dust attenuation which can be corrected for, but at higher redshift the dust distribution may have different geometries. The calibration of both metallicity indicators and SFR indicators also depend on the initial mass function, which also may vary with redshift. Furthermore, AGN activity peaks in this epoch can contribute large amounts of Hα, UV, and IR luminosity and inflate the apparent SFR of a galaxy. Most higher redshift surveys are flux-limited, meaning they preferentially detect massive, bright galaxies which can cause systematic bias in galaxy samples [66, 71].

At $z \sim 1$ in particular, some diagnostic lines are weak and/or shifted out of the optical spectrum. At this redshift, a common method is using near-IR spectroscopy to infer star formation rate through Hα and metallicity through N2, or $\log([\mathrm{N\,II}]/\mathrm{H}\alpha)$. Near-IR spectroscopy utilizes the wavelengths of light just outside the red visual spectrum in the infrared (from 780nm to 2500nm). The Earth's blackbody radiation peaks around 10,000nm, making ground based observations in the near-IR more difficult due to the luminosity of the Earth. In the spectrum, the brightest skylines are caused by short-lived hydroxyl radicals in the upper atmosphere. To combat this, we nod the telescope by arcseconds so the source falls on different spatial parts of the detector between exposures. The different exposures can then be subtracted from one another, subtracting off the skylines that remained in the same place and isolating the signal from the galaxy. The isolated signal can then be stacked, boosting the signal and removing most of the skylines.

While the atmosphere emits in the near-infrared, it also absorbs specific wavelengths through molecular absorption. These bands of absorption define the boundaries for near-IR filters which fill transmission windows within the atmosphere. This can be corrected by a telluric correction, whereby a standard star is observed through similar atmospheric conditions as your target. This allows for a correction to the target's spectrum based on the known spectrum of the standard star.

1.5 Galaxy Trends and Observations

Through the measurement techniques described above, we can study the evolution of galaxies by measuring the change in their stellar mass, star formation rate, and metallicity with

redshift. One such observation is that the distribution of star formation rate at a fixed stellar mass is bimodal. Actively star-forming galaxies have star formation rates that correlate well with stellar mass, defining a "main sequence" [20, 109, 125]. The second population consists of galaxies with negligible SFR ("quenched" galaxies). The SF main sequence has been observed out to $z > 2$, and this evolution is characterized primarily by an increase in normalization with redshift [140, 133, 121]. The fraction of quenched galaxies has been built up steadily over cosmic time [104, 141], though quenched galaxies have been observed to exist at redshifts as high as $z \sim 5$ [25, 41, 130]. At all redshifts, the fraction of quenched galaxies correlates strongly with stellar mass. However, the reason for this is still unknown. Some proposed mechanisms for quenching star formation are AGN feedback [43, 119, 15] and halo quenching (or virial shock heating) [14, 52, 161] which are likely to be more efficient in more massive galaxies. However, quenched fractions also correlate with the environment whereby the fraction of quenched galaxies at fixed stellar mass is higher in the cluster environment. The locus and spread of the SF main sequence itself shows at most a weak dependence on environment in the local Universe [7].

As mentioned previously, star formation rate traces the evolution of stellar mass through time, and metallicity tracks how far along a galaxy is through its evolution. Mass and metallicity are well-known to evolve together through what's known as the mass-metallicity relation (MZR). The MZR is well established in the local Universe, whereby more massive galaxies are more metal-enriched [145, 71]. For a galaxy, the total mass determines how effectively a galaxy can retain gas against the outward pressure of supernovae and stellar winds. More massive galaxies may exhaust their gas reservoirs faster, but also can retain the recycled, metal-enriched gas more easily. This depends on how SFR and gas fractions scale with stellar mass. The total scatter about the MZR is intrinsic and correlates with SFR [92], and is defined as the Fundamental Metallicity Relation (FMR). In the local universe, the FMR is well characterized ([92, 37], primarily through local large scale surveys such as the Sloan Digital Sky Survey [1] and studies suggest it holds without significant evolution out to $z \sim 2.5$ [92, 34]. The shape of the FMR is not uniform with mass but instead at low stellar mass, metallicity decreases sharply with increasing SFR, while at high stellar mass, metallicity depends less on SFR [92]. The proposed equilibrium model [18, 40, 82] describes a balance between inflowing gas, outward stellar feedback, and consumption of material whereby a galaxy maintaining this balance lies on the star-forming main sequence and the FMR. Therefore, a galaxy's position on the FMR can be a powerful diagnostic for determining if the galaxy is in equilibrium or if that equilibrium is being disrupted, for example by external (environmental) influences.

1.6 Environment

There are various environmental mechanisms that may effect a galaxy's equilibrium. Ram pressure stripping occurs when a galaxy moves through the hot intracluster medium, and hydrodynamic drag strips the cold ISM gas needed for star formation from the galaxy. Typically, ram pressure stripping can efficiently strip on relatively short timescales of ≤ 1 Gyr ([129, 144, 86]). For low mass galaxies, the stripping time can occur on even smaller timescales ($\sim 100-200$ Myr) due to the shallow gravitational potential [101, 93, 143]). This effect is very strong in dense clusters, and could completely quench a galaxy if the structure, orbit, and stellar mass are favourable for this to occur [56, 17]. Slower effects, such as strangulation occur when the hot gas halo that feeds future star formation is stripped away as a galaxy falls into a group or cluster [80]. The galaxy continues to form stars at a declining rate out of its cold gas reservoir, but no new gas is added, so the galaxy slowly runs out of material for star formation. This quenches the galaxy on longer timescales ($\sim 1-2$ Gyr) [9]. While strangulation is an external gas removal process, quenching could also occur through internal mechanisms without the need for violent, external stripping of hot gas through a process known as overconsumption [96]. Overconsumption relies on the halting of accretion because of the galaxy now being within the halo of a larger group or cluster, rather than the forceful removal of gas. As the galaxy continues to form stars, star formation drives outflows which actively eject gas and with no inflow to compensate, the galaxy quenches when the internal reservoir is expended. This can lead to faster quenching timescales than strangulation due to the presence of the outflows.

1.7 Previous Work

Numerous studies and surveys have aimed to measure star formation rate and metallicities across a wide range of redshifts. 3D-HST [148] is a low spectral resolution, near-IR spectroscopic survey with the Hubble Space Telescope that surveyed 600 square arcminutes of various well studied extragalactic survey fields with WFC3/G141 grism coverage. The survey is optimally designed for the study of galaxy evolution over $1 < z < 3.5$ to study star formation, the role of environment in galaxy evolution, and resolving the growth of disks and bulges. These observations have been used in various studies such as in ref. [154] who measure the star formation main sequence down to a stellar mass of $10^{8.4} M_{\odot}$ and across a redshift range of $0.5 < z < 2.5$ using Hα inferred from the 3D-HST data and UV + IR SFRs. They found that star formation correlates with stellar mass, with a slope that is steeper for $\log(M_*/M_{\odot}) \lesssim 10.2$. They also compare these Hα SFR with those derived from

IR/UV to infer that dust extinction at Hα is strongly mass and redshift dependent.

Many studies have aimed to characterize the FMR, but few papers have looked at the effects of environment on the FMR for high-redshift samples, with some exceptions such as MOSDEF [29] and KMOS-3D [158, 89]. The MOSFIRE Deep Evolution Field (MOSDEF) survey [79, 124] is a moderate-resolution near-IR spectroscopic survey which obtained rest-frame optical spectra for $\sim$ 1500 galaxies at $1.37 \leq z \leq 3.80$ in three CANDELS fields. Within MOSDEF, ref. [29] studied the environmental dependence of gas-phase metallicities at $1.4 \leq z \leq 2.6$. They find that at $z \sim 1.5$, the average metallicity in overdense environments across the intermediate mass range ($10^{9.8} - 10^{10.8}$ M$_\odot$) is higher relative to their field counterparts. However, this metallicity enhancement is negligible at higher redshift, $z \sim 2.3$. Their results suggest that the variation of the mass-metallicity relation with local environment is small and reverses at $z \sim 2$. This supports the hypothesis that galaxies residing in overdensities host a higher fraction of pristine gas at $z \sim 2.3$, while at $z \sim 1.5$ shock-heated gas in overdensities cannot cool down efficiently leading to the suppression of pristine gas and the re-accretion of metal-enriched outflows. Another high-redshift sample, the KMOS-3D survey ref. [156] is an integral field survey of 739, $\log(M_*/M_\odot) > 9$, galaxies at $0.6 < z < 2.7$ using the K-band Multi Object Spectrograph (KMOS) at the Very Large Telescope. KMOS-3D provides a population-wide census of kinematics, star formation, outflows, and nebular gas conditions both on and off the star-forming galaxy main sequence through resolved analysis of the Hα, [N II] , and [S II] emission lines. Using data from KMOS-3D, ref. [158] present measurements of $[N\,\textsc{ii}]/H\alpha$ as a probe of the gas-phase oxygen abundance for a sample of 419 star forming galaxies. They find no significant dependence of the $[N\,\textsc{ii}]/H\alpha$ ratio on galaxy environment although they did not cover a wide range of environments. They also find no significant dependence on SFR at fixed redshift and stellar mass, even while probing deep below the star forming main sequence with deep observations.

Ref. [89] also use KMOS to measure gas-phase metallicities and star formation rates for star-forming galaxies in a massive cluster at $z \sim 1.5$, with the aim of detecting environmental signatures in chemical enrichment at $z > 1$. They measure individual metallicities for ten confirmed cluster members and found that galaxies in the inner half of R_{200} have $[N\,\textsc{ii}]/H\alpha$ ratios and resultant oxygen abundances $\sim 0.1 - 0.2$ dex higher than both infalling and field galaxies. They interpret this as evidence for a strangulation quenching model.

1.8 GOGREEN/GCLASS

While ref. [89] present results for a single cluster, ref. [94] observed targets from the Gemini Cluster Astrophysics Spectroscopy Survey (GCLASS) [106] using HST/WFC3 G141 grism. GCLASS is a spectroscopic survey of 10 rich clusters at $0.85 < z < 1.34$ carried out by the GMOS instrument. The cluster sample was drawn from the Spitzer Adaptation of the Red-sequence Cluster Survey (SpARCS) and produced a spectroscopic sample of 797 cluster and field galaxies, used to evaluate the effects of environment and stellar mass on galaxy properties at $z \sim 1$. Ref. [94] used these observations of spectroscopically confirmed star-forming cluster galaxies to construct spatially resolved Hα maps, with the goal of directly measuring environmental quenching at high redshift. By comparing the spatial extent of Hα emission to the stellar continuum, they found evidence for rapid outside-in quenching, consistent with ram-pressure stripping, in cluster galaxies that had recently quenched. However, their grism observations could not spectrally resolve Hα from [N II] , precluding any estimates of the gas-phase metallicity.

The GOGREEN/GCLASS [106, 10] survey measured star formation rates from SED fits to the photometry and from the [O II] emission line. Ref. [111] found SFR suppression at fixed stellar mass in the cluster galaxy star-forming main sequence compared to the field counterparts by a factor of $1.4 \pm 0.1 (\sim 3.3\sigma)$ across the stellar mass range $9.0 < \log(M_*/M_\odot) < 11.2$. They explored several scenarios to explain this suppression such as formation time differences and environmentally induced quenching. However, the spectral coverage of GOGREEN/GCLASS did not include any metallicity-sensitive features.

The present work revisits a selection of GOGREEN and GCLASS star-forming galaxies and presents new, near-IR spectroscopy that includes a more robust star formation rate indicator in Hα and a readily available metallicity indicator in the form of the [N II]/Hα line ratio. Our work shares a similar objective to ref. [89] of characterizing the environmental impact on the MZR, although I present a larger sample of cluster galaxies at a different cosmological epoch, allowing for a more statistically robust comparison between field and cluster metallicities at a slightly lower redshift. I measure the SFR-mass-metallicity relations in clusters and compare our findings against literature field samples and field galaxies within our sample; constraining models of environment-driven quenching. Using Gemini/F2 and Keck/MOSFIRE, I observe 8 overdense regions spanning a redshift range of $0.782 < z < 1.401$ and measure the Hα and [N II] fluxes in these galaxies.

1.9 Outline

The layout of this thesis is as follows. In Section 2.1 I describe the relevant details of our data such as the masks observed and the methods to reduce this data as well as the calculation of the star formations rates. Section 2.2 I go through the results, with plots that show relationships of metallicity, star formation rate, and stellar mass. In Section 2.3, I discuss the results and compare with results from the literature. Finally, I summarize the results and share my interpretation in Section 2.4. In Appendix A I show various additional plots created for verification purposes or additional information unfit for the main body. Appendix B.1 discusses the aperture corrections to the continuum, while Appendix B.2 discusses the aperture corrections to the fluxes.

For the entirety of this thesis, equivalent widths are reported in the rest frame, fluxes are in units of 10^{-17} erg/s/cm^2, and magnitudes are reported in the AB system [110]. I also assume a ΛCDM cosmology with $\Omega_m = 0.307$, $\Omega_\Lambda = 0.693$ and $H_0 = 67.7$ km s^{-1} Mpc^{-1} [120].

Chapter 2

Observations

2.1 Data and Reduction

2.1.1 Target Justification

We prioritize the selection of star-forming (SF) galaxies for most of the Keck NIR spectroscopy as follows. Top priority is given to galaxies with stellar mass $M > 10^{9.5} M_{\odot}$ and a spectroscopic redshift[1] within $\Delta z = 0.1$ of the cluster redshift. In addition, top priority targets have a detection of either [O II] with a rest-frame equivalent width of at least 3Å, or Hα+[N II] from ref. [94]. The second level of prioritization is the same, except that we include all galaxies that are either classified photometrically as star-forming, or as candidate transition galaxies. Star-forming galaxies are selected as those with either $(NUV - V) < 2 * (V - J) + 1.1$ or $(V - J) + 0.45 > (U - V)$. Transition galaxies are galaxies that fall into either the green valley (GV), blue quiescent (BQG) or post-starburst (PSB) classifications of ref. [97]. The third and final priority class is for $M > 10^{9.5} M_{\odot}$ galaxies that are either emission line, SF or transition galaxies and have only a photometric redshift that is within $\Delta z = 0.16$ of the cluster redshift.

For the Gemini target selection, and some of the earlier Keck observations, the selection was similar but more restrictive. Top priority targets required that both Hα and [N II] are clear of bright sky lines; while second-tier targets only require that of the Hα line. In addition the spectroscopic cluster membership requirement was more strict, with $\Delta z < 0.01$.

[1] The confirmed spectroscopic redshift is either from GOGREEN with a quality flag of 3 (likely redshift) or 4 (certain), or from the grism observations of ref. [94].

Cluster	Cluster z	Band	Masks	Spectra	Hα Detections
Keck MOSFIRE					
SpARCS0215	1.004	J	4	93	26
SpARCS1047	0.956	J	3	84	38
SpARCS1051	1.035	J	1	20	8
SpARCS1613	0.871	J	3	93	28
Gemini Flamingos 2					
SpARCS0034	0.867	J	2	42	5
SpARCS0035	1.336	H	2	49	11
SpARCS0036	0.869	J	1	19	2
SPT-CL J0205	1.323	H	1	14	3
Totals	/	/	**17**	**414**	**121**

Table 2.1: Summary of observations for Keck MOSFIRE and Gemini Flamingos 2. Higher cluster redshifts were observed in a longer wavelength filter, such that any $H\alpha$ detections will fall on the detector.

2.1.2 Data Acquisition

The data used in this study are observations obtained using Gemini FLAMINGOS2 and Keck MOSFIRE in semesters 2024B and 2025A. These observations are NIR spectroscopy targeting the Hα line at $0.8 \lesssim z \lesssim 1.4$, which falls within the J-band and H-band filters. The data were acquired using an ABBA dither pattern with 180/120 second exposures for J-band observations with Gemini/Keck and 120 seconds for H-band. For the Keck MOSFIRE observations, we observed 11 masks from 4 different clusters and collect a total of 290 spectra; 224 of which were unique observations (only observed on one mask). For Gemini FLAMINGOS2 observations, we observed 6 masks from 4 different clusters and collected a total of 124 spectra; 94 of which are unique. Combined, there is 34.1 hours of total exposure time, with 414 spectra collected and 121 detected Hα emissions. The sample is summarized in Table 2.1.

2.1.3 Reduction Process

To reduce the raw spectra, we use the semi-automated reduction pipeline called *Pypeit* [123, 122]. *Pypeit* runs an object finding algorithm, which detects high SNR objects within

each slit. The sky subtraction was done by subtracting pairs of observations in the ABBA dither sequence, resulting in a 2D spectrum of the galaxy.

As shown in Table 2.1, most clusters were observed with multiple masks, and some galaxies were observed on multiple masks. To maximize signal to noise, we combined the separate spectra of the same object by summing the flux, weighted by the inverse variance.

We included a telluric star on each mask to use in the sensitivity function calculation. This ensures that the telluric star is observed through the same atmospheric conditions and instrumental setup as the science data. The telluric stars were selected from the Gaia DR3 catalogue to be bright ($M_g \lesssim 5$) and blue ($B - R) \lesssim 1$). These stars are generally not standard stars available in the *Pypeit* database, so we use models based on the stellar type and magnitude from Gaia. Ultimately, we calibrate our fluxes by comparison with broadband photometry, as described in Appendix B.

In Figure 2.1 we show the reduced 1-D and 2-D spectrum data for one of our targets, as well as the K-band image of the galaxy.

2.1.4 Analysis Methods

We fit the $H\alpha$ and $[N\,\textsc{ii}]\lambda\lambda 6585, 6550$ emission lines with the *emcee* package [50]. The function fit to the data was three Gaussian components superimposed on a linear continuum. For each detection, we fit six parameters: **1)** Redshift **2)** Amplitude of the $H\alpha$ line **3)** Amplitude of the [N II] λ6585 line **4)** line width σ **5), 6)** Slope and intercept of the continuum. Since Hα and [N II] are expected to trace the same gas dynamics, we assume the same width for all three lines. We fix the amplitude ratio of $[N\,\textsc{ii}]\lambda 6585/[N\,\textsc{ii}]\lambda 6550 = 3$ as expected [98]).This fit is done on every galaxy with detected Hα, and the two [N II] lines are simultaneously fit independently of whether or not they are evident. Parameters of the fit are shown in Table 2.2.

About half our sample have spectroscopic redshifts from GOGREEN, while the rest either had a photometric redshift or a redshift from ref. [94]. We show a plot of our measured Hα redshift as a function of catalogue redshift in Figure A.1.

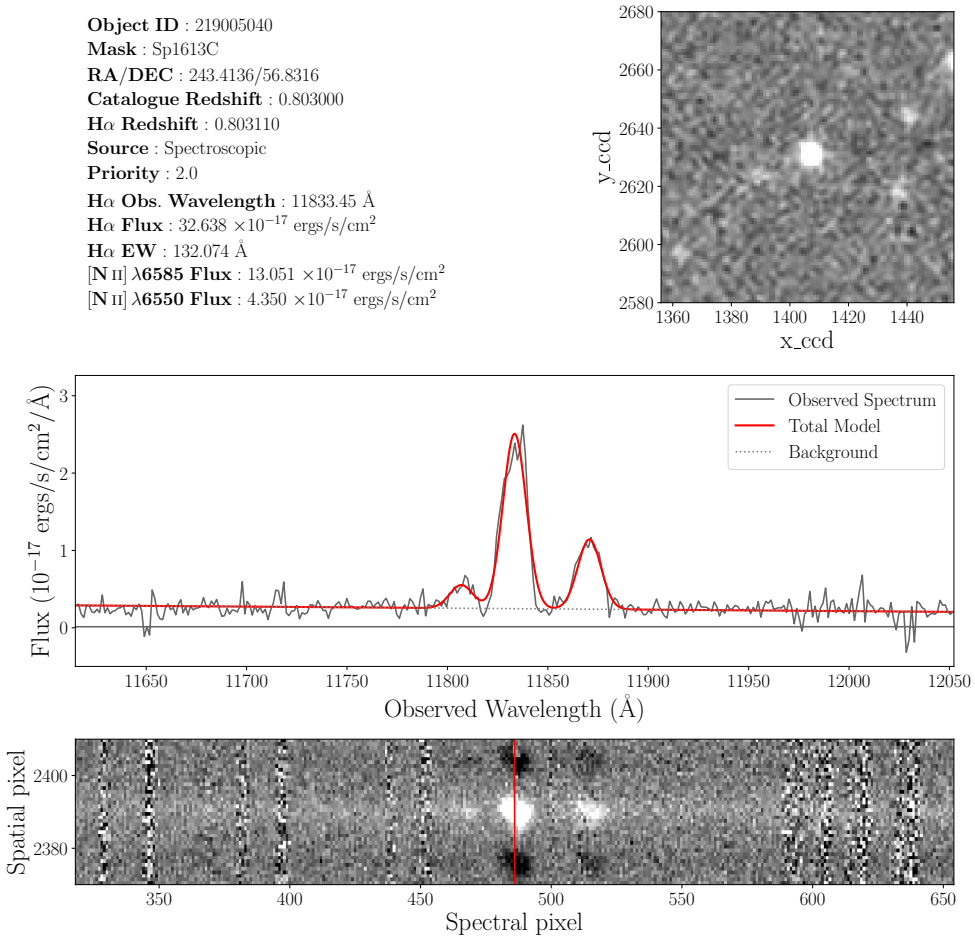


Figure 2.1: Information card generated for each galaxy with an $H\alpha$ detection. Top Left: Information about the galaxy, including measured flux information. Top Right: Image of the galaxy (K-band) with the axes being the position on the CCD. Middle: 1-dimensional spectrum which shows flux as a function of wavelength. The Hα and [N II] detections are clear in the spectra, and lie centred in the plot. Bottom: 2-dimensional spectrum from *Pypeit* with the Hα shown at the red vertical line with [N II] on either side of it. This image is in units of pixels, where the y-axis is the spatial pixel and the x-axis is the spectral pixel. The dark features on above and below the emission arise from the ABBA dither pattern used for sky subtraction. With this pattern, the "A" and "B" nod positions are differenced such that the source signal adds constructively at the central trace, while each position contributes a negative residual above and below.

Parameter	**Priors**	**Comments**
z	$\frac{(\mu_{H\alpha}-20)}{6562.8} < z+1 < \frac{(\mu_{H\alpha}+20)}{6562.8}$	$\mu_{H\alpha}$ = visually confirmed Hα detection wavelength
$A_{H\alpha}$	$0 < A_{H\alpha} < 5$	
$A_{[N\,\mathrm{II}]}$	$0 < A_{[N\,\mathrm{II}]} < 4$	Amplitude of the weaker line defined as $\frac{1}{3}A_{[N\,\mathrm{II}]}$ and fit simultaneously
σ	$2 < \sigma < 20$	σ fit simultaneously for every line
m	$-1 < m < 1$	Slope of the continuum measurement measured from a pivot wavelength of $\mu_{H\alpha} - 100$
b	$-10 < b < 10$	Intercept of the continuum at pivot wavelength defined above

Table 2.2: We show a summary of the parameters fit with *emcee* with the priors used and any additional comments about the fitting process.

We measured line fluxes and equivalent widths from the best fit parameters of our model. For each line, the flux is the area under the Gaussian,

$$F_{H\alpha} = \sqrt{2\pi}\sigma A_{H\alpha} \tag{2.1}$$

$$F_{\lambda 6585} = \sqrt{2\pi}\sigma A_{[NII]} \tag{2.2}$$

$$F_{\lambda 6550} = \sqrt{2\pi}\sigma \frac{A_{[NII]}}{3} \tag{2.3}$$

The equivalent width is the integrated ratio of the strength of the emission line to the continuum. For example, the rest-frame equivalent width of the Hα line is

$$EW(H\alpha) = \frac{1}{1+z}\sum_i \frac{A_{H\alpha} e^{\frac{-(\lambda_i-\mu)^2}{2\sigma^2}}}{m(\lambda_i - \lambda_{pivot}) + b} \tag{2.4}$$

where

$$\mu = \lambda_{rest,H\alpha}(1+z) = 6562.8(1+z)\text{Å} \tag{2.5}$$

An example fit is shown as the red line in the middle plot of Figure 2.1.

Hα SFR Calculations

We convert the Hα fluxes to SFR through the following relations. We calculate the Hα luminosity as

$$L_{H\alpha} = 4\pi F_{H\alpha} D_L^2,$$

where D_L is the luminosity distance. These luminosities are not dust corrected, as the dust correction is only applied to the star formation rates. However, we do apply an aperture correction to both our continuum and the fluxes, as described in Appendix B.

To convert our measured fluxes to star formation rates, we use the standard relation [66] adapted from a Salpeter initial mass function (IMF) to a Chabrier [27] IMF following the method of ref. [105]. We also apply an average dust correction, $\beta(M,z)$, to our Hα SFR such that

$$\frac{SFR(H\alpha)}{M_\odot\, yr^{-1}} \beta(M,z) \frac{1.7\times 10^{-8}\, L_{H\alpha}}{L_\odot} \quad . \tag{2.6}$$

The factor $\beta(M,z)$ is calculated using the analysis of 3D-HST data by ref. [154]. They measure star formation rates as a function of stellar mass for two redshift ranges: $0.5 <$

$z < 1.0$ and $1.0 < z < 1.5$. We calculate a dust correction factor to scale their $L_{H\alpha}$ curves to match their $L_{UV} + L_{IR}$ curves as a function of stellar mass for both redshift ranges. $\beta(M, z)$ is then computed by linearly interpolating between the two curves.

We also convert our measured $\log([N\,\textsc{ii}]/H\alpha)$ ratio to $\log(O/H)$ using the standard N2 method in [118]. We calculate the oxygen abundance as

$$12 + \log(O/H) = 8.90 + 0.57 \times \log([N\,\textsc{ii}]/H\alpha) \quad . \tag{2.7}$$

While we do not explicitly discuss the oxygen abundance, we show the oxygen abundance as a secondary axis on Figure 2.6.

2.1.5 Cluster Membership and Selection

While our target selection prioritizes galaxies with redshift close to that of the associated cluster, we now apply a more precise definition of cluster membership. We use a simple selection based on rest-frame velocity difference, using the redshift we measure for the detected emission lines, and distance from the cluster centre, as shown in Figure 2.2. We define cluster galaxies to have $|\Delta V| < 3000\,\mathrm{km/s}$ and $D < 1Mpc$, shown as the red box. We perform similar cuts to the data from ref. [94].

We also sorted through the total sample of 121 galaxies and flagged individual spectra for either non-detections where the S/N was small or AGN. We discarded the non-detections based on the 1-D spectra, and flagged AGN to be excluded from the analysis. In total, we have 23 cluster members and 79 field members based on the above selection criteria.

2.1.6 Field Comparison Samples

Throughout the analysis, we compare our results with several field samples selected from the literature that span a similar mass and redshift range. The low resolution 3D-HST [148] provides equivalent width ($H\alpha + [N\,\textsc{ii}]$) measurements up to about $z \approx 2$; we limit this to the range $0.8 < z < 1.4$ relevant to our study. We also compare to the MOSDEF [79, 124] and KMOS-3D [156, 158] field samples, which have higher spectral resolution and hence resolve [N II] from Hα. Again we limit both surveys to the redshift range of interest. For all datasets, we apply any flags set by the authors, such as untrustworthy fluxes, redshifts, and spectra. To visualize the redshift distributions, we show the redshift range for each dataset, and hashes on that line to show the distribution in Figure 2.3.

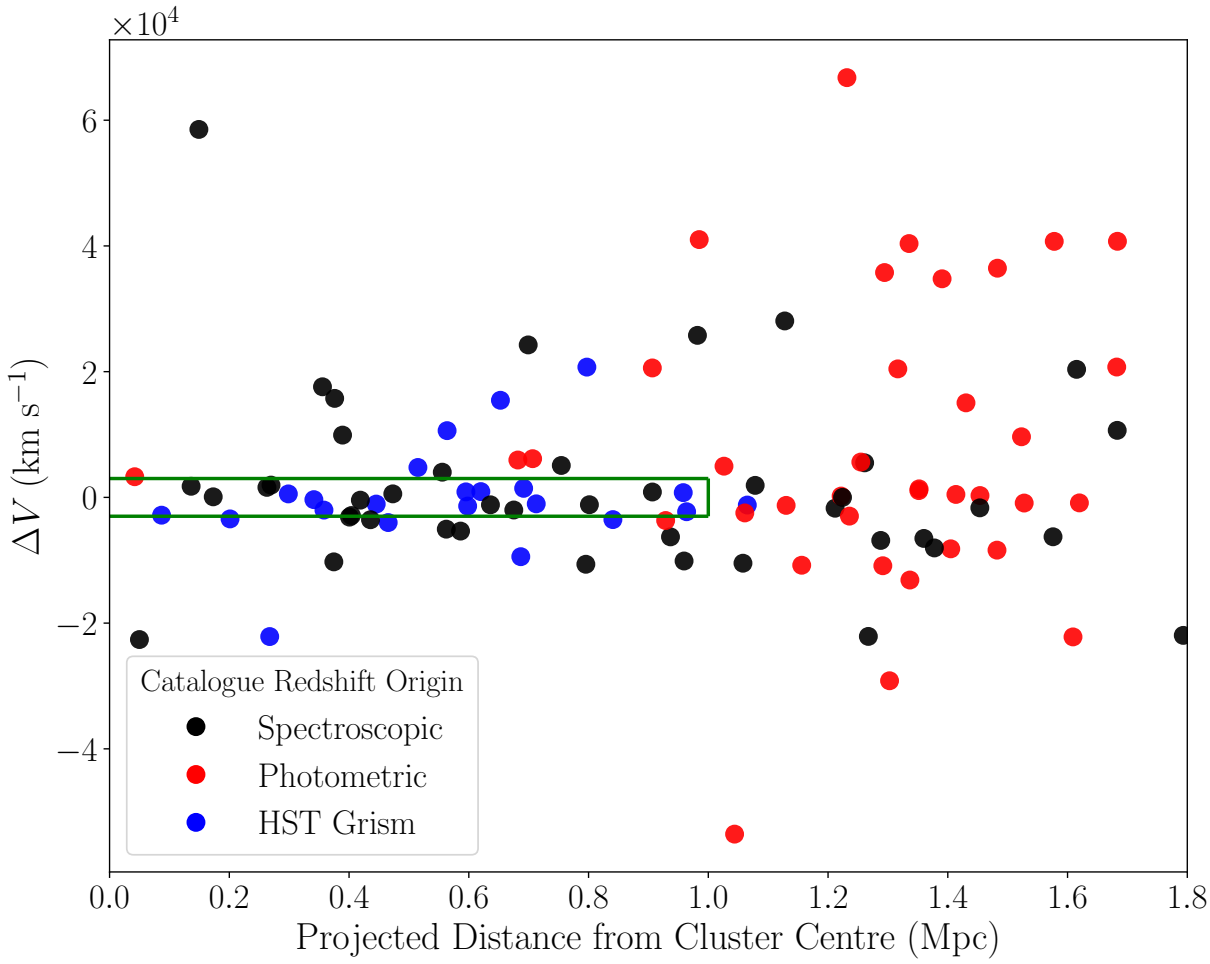


Figure 2.2: We show the rest-frame velocity difference relative to the cluster, as a function of distance from the cluster centre for our work. Velocities are measured from the emission line redshifts obtained from our spectroscopy. The galaxies within the red box with dimensions ΔV = 3000km/s and $D = 1Mpc$ we define to be cluster members, while galaxies outside this box we define as field galaxies.

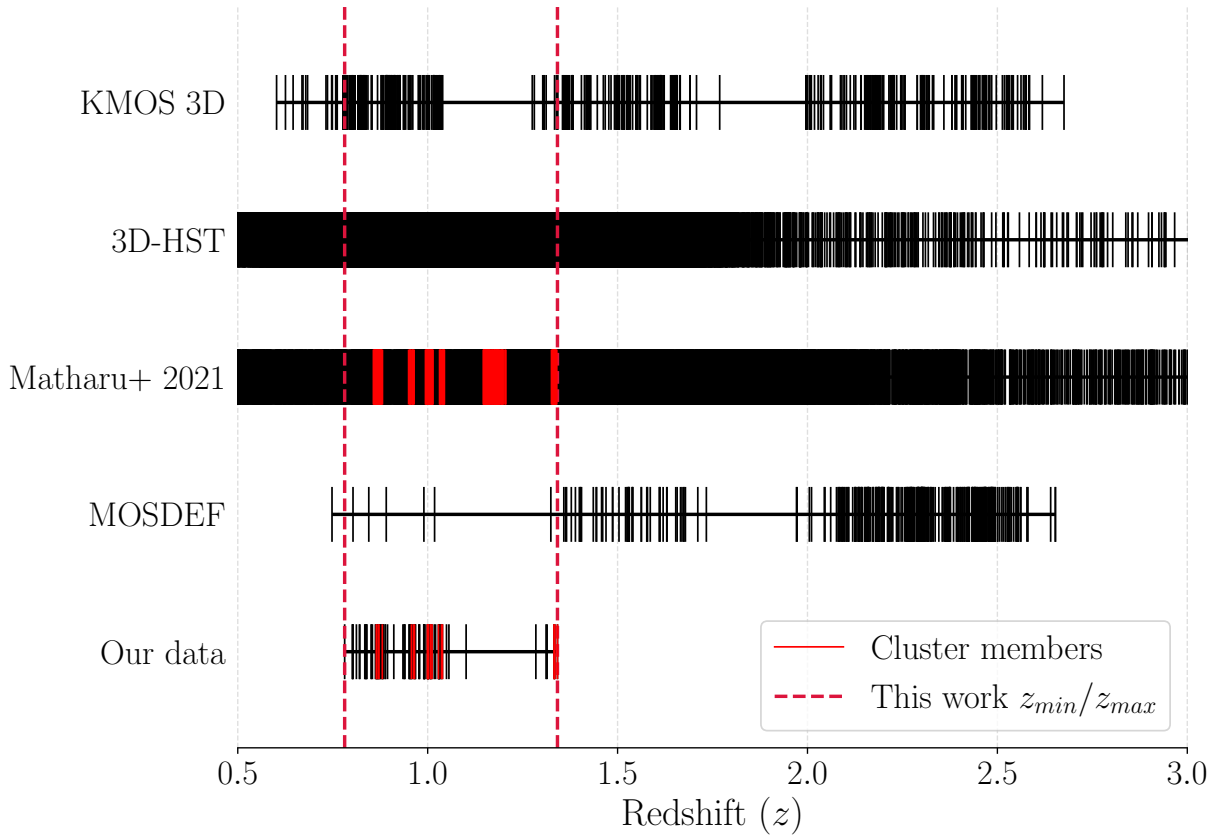


Figure 2.3: We show the redshift distribution for each dataset to which we compare our sample. Each data set covers a broad redshift range, which we limit for our comparison. 3D-HST has a maximum redshift of $z \sim 6$, so for readability we limit the axis ranges even though 3D-HST continues to $z = 0$ and higher than $z = 3$. Similarly, the data from ref. [94] spans a redshift range of $0 < z < 3.4$. The red, vertical dashed lines show the minimum and maximum redshift of our sample, so for most of the samples we limit to the hashes between these lines. Note that for ref. [94] and our data, we mark in red the cluster members determined by the velocity dispersion and distance from the cluster centre. MOSDEF has very few low redshift objects, and the field is dominated by $z > 2.0$ galaxies. On other plots in this paper, we limit the MOSDEF data to $z < 1.4$.

We use the SDSS DR8 as a $z = 0$ reference for some of the analysis. We exclude measurements with errors $> 10\%$ of the measurements as these are likely non-detections, and limit the sample to the same range of masses and Hα/[N II] ratios as our sample. We use the environment classifications from ref. [142].

2.2 Results

2.2.1 Consistent Equivalent Widths

In Figure 2.4, we show Hα equivalent width as a function of stellar mass. We compare with data from two literature samples; MOSDEF limited to $z < 1.4$ and KMOS-3D limited to the same redshift and we compute our statistics to the combined sample. Our cluster sample is shown as the red stars, while our field sample is the small purple stars. We show a rolling mean in bins of stellar mass to easily compare equivalent widths. The error bars represent the bootstrap 1σ error on the mean which is also shown by the shaded regions.

We find that across this range of stellar masses, there is no significant offset in Hα equivalent width between the field and cluster. Equivalent width is invariant to dust and flux calibrations, so we show this plot as a check to verify the following star formation rate.

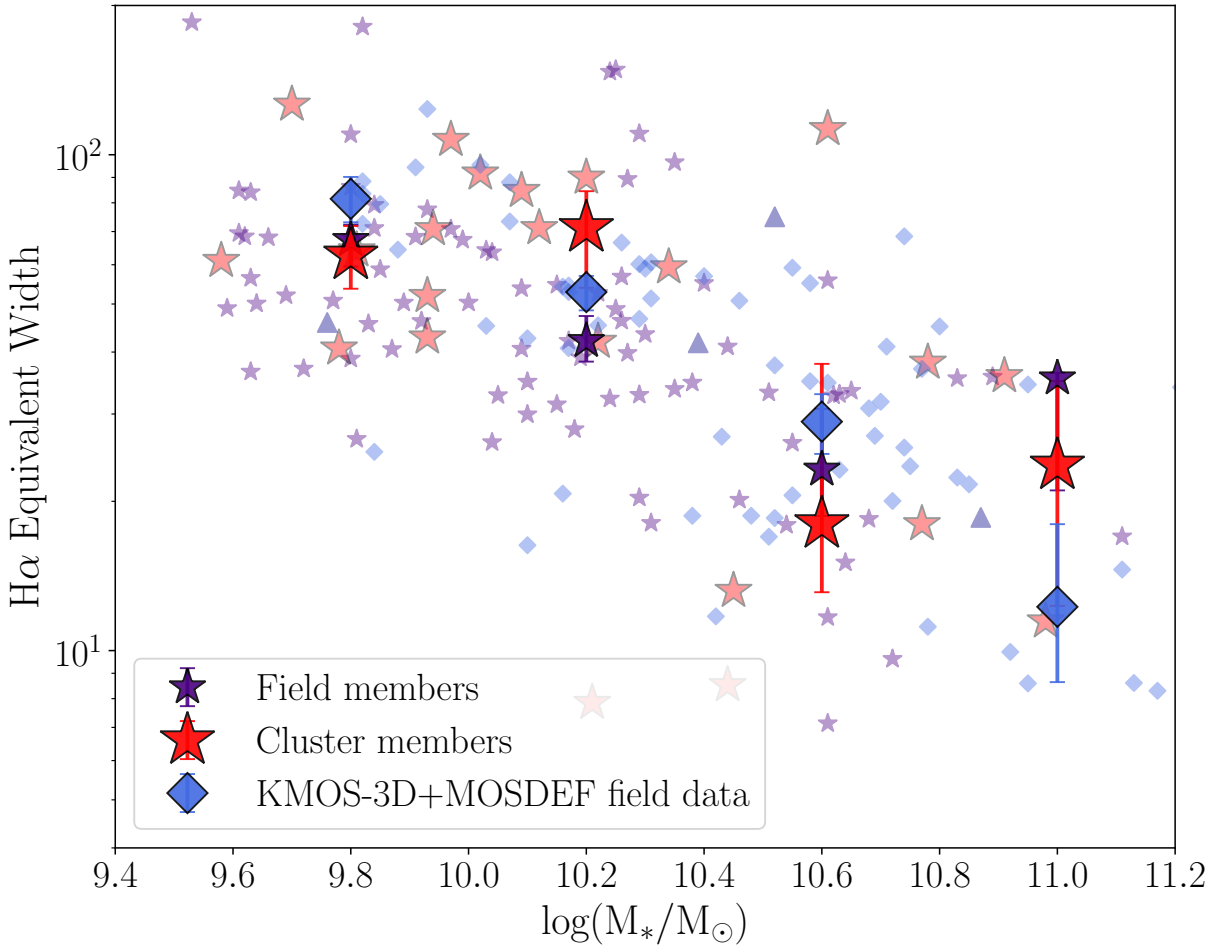


Figure 2.4: We show rest-frame Hα equivalent width as a function of stellar mass and compare our data to that of MOSDEF and KMOS-3D. We show the data points in the background, where the large red stars are our selected cluster sample, the small purple stars are our field sample, the blue diamonds are the KMOS-3D sample, and the blue triangles are the MOSDEF sample where KMOS-3D and MOSDEF are redshift limited ($z < 1.4$). The large foreground points represent the rolling means of each dataset, with KMOS-3D and MOSDEF combined into the large, blue diamonds. The error bars and shaded regions represent the 1σ errors on the means of the 4 mass bins. At all masses, there is no significant offset between our cluster and any field sample.

2.2.2 Consistent Star Formation Rates

In Figure 2.5 we show dust-corrected star formation rates as a function of stellar mass. We represent our cluster sample as stars with black outline and a colour bar representing redshift. Our field members are represented by the grey stars, the redshift-limited MOSDEF at $z < 1.4$ as the blue triangles, and the KMOS-3D ($z < 1.4$) data as the blue diamonds. We also show two lines from ref. [154] which are $L_{UV} + L_{IR}$ star formation rate measurements at two redshift ranges. We correspond the median of these redshift ranges to the colour bar, showing in purple the $0.5 < z < 1.0$ line and the $1.0 < z < 1.5$ line in green.

Our sample shows increasing star formation rate with increasing redshift and increasing stellar mass. We measure no offset compared to any literature sample, and measure a total scatter about the star forming main sequence (SFMS) of both our field and cluster samples to be ~ 0.3 dex. This is consistent with literature values [153, 140, 58].

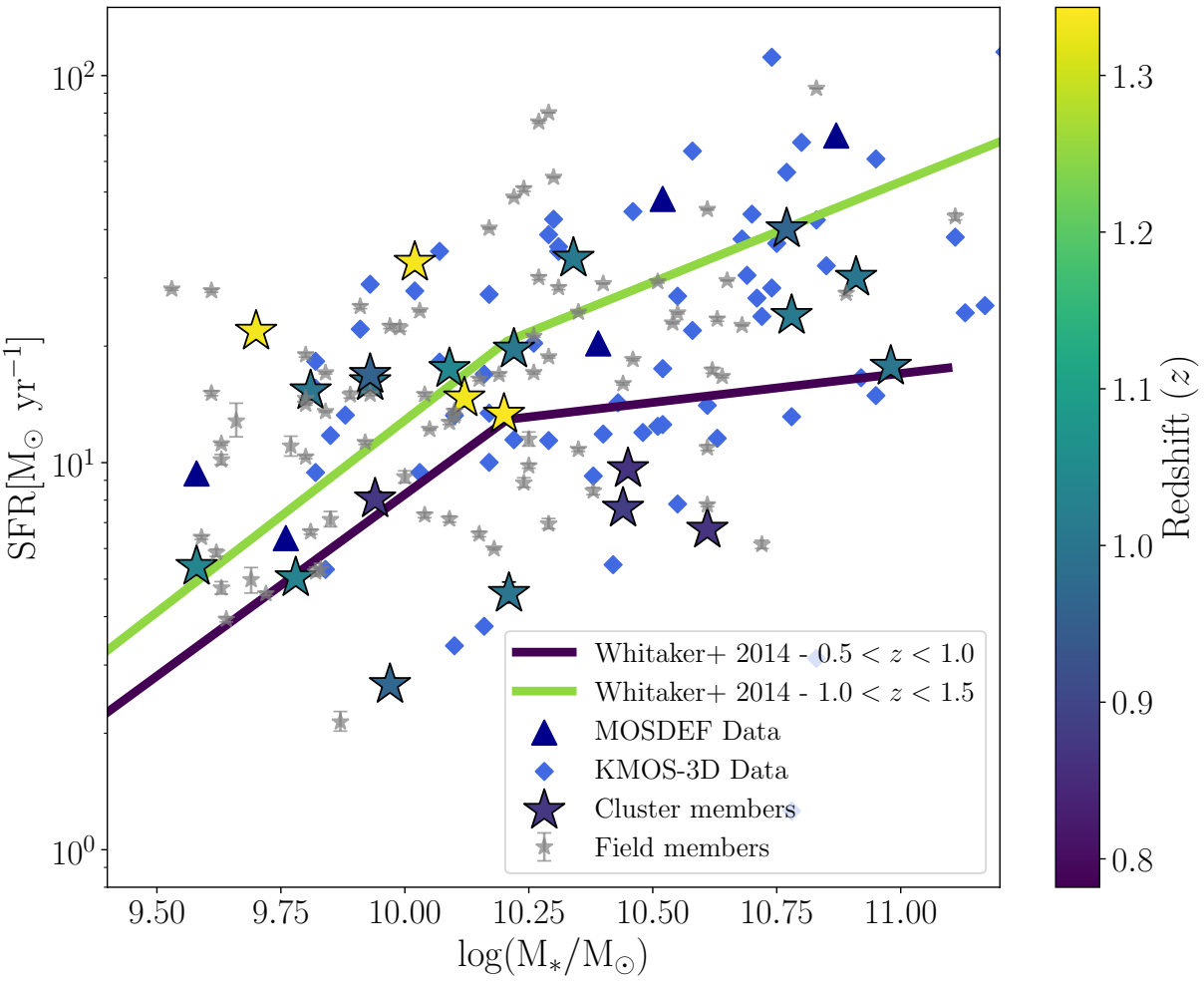


Figure 2.5: We show star formation rates as a function of stellar mass. Our cluster population is represented by the stars with black outline and a colourbar showing the galaxy redshift. Our field galaxies are represented by the gray stars, the MOSDEF sample at $z < 1.4$ as the blue triangles, and KMOS-3D ($z < 1.4$) as the blue diamonds. The green and purple lines are lines of best fit from ref. [154] which are field star formation rates calculated using $L_{UV} + L_{IR}$ observations. The darker purple line represents the redshift range $0.5 < z < 1.0$ while the green is $1.0 < z < 1.5$. As our Hα fluxes were corrected for dust, we applied a similar dust correction to MOSDEF and KMOS-3D with the same method. Our sample shows increasing star formation rates with increasing redshift and increasing stellar mass, and are fully consistent with both field comparison samples. We calculate the scatter of both our field and cluster samples to be ~ 0.3 dex, consistent with literature values.

2.2.3 Enhanced Cluster Metallicities

In this section, we use our measurements of [N II] and Hα to infer metallicities of our cluster sample. In Figure 2.6, we show log([N II]/Hα) as a function of stellar mass. We represent our cluster sample with the large, red stars and field sample with the smaller purple stars. The blue triangles represent the MOSDEF field sample and KMOS-3D shown in blue diamonds. We show the lines of best fit for each sample, as well as the 1σ confidence interval of each best fit. We combine MOSDEF with KMOS-3D when calculating the best fit for the field. We also show on the right-hand side the oxygen abundance calculated through the N2 method described in Equation 2.7.

The slopes of the cluster and field relations are different such that the offset converges at high stellar mass. At an intermediate stellar mass of $10^{10.2}$M$_\odot$, we measure an offset in the log([N II]/Hα) ratio of 0.155 ± 0.043 dex between our cluster and the MOSDEF+KMOS-3D field sample and an offset of 0.083 ± 0.035 dex relative to our own field sample.

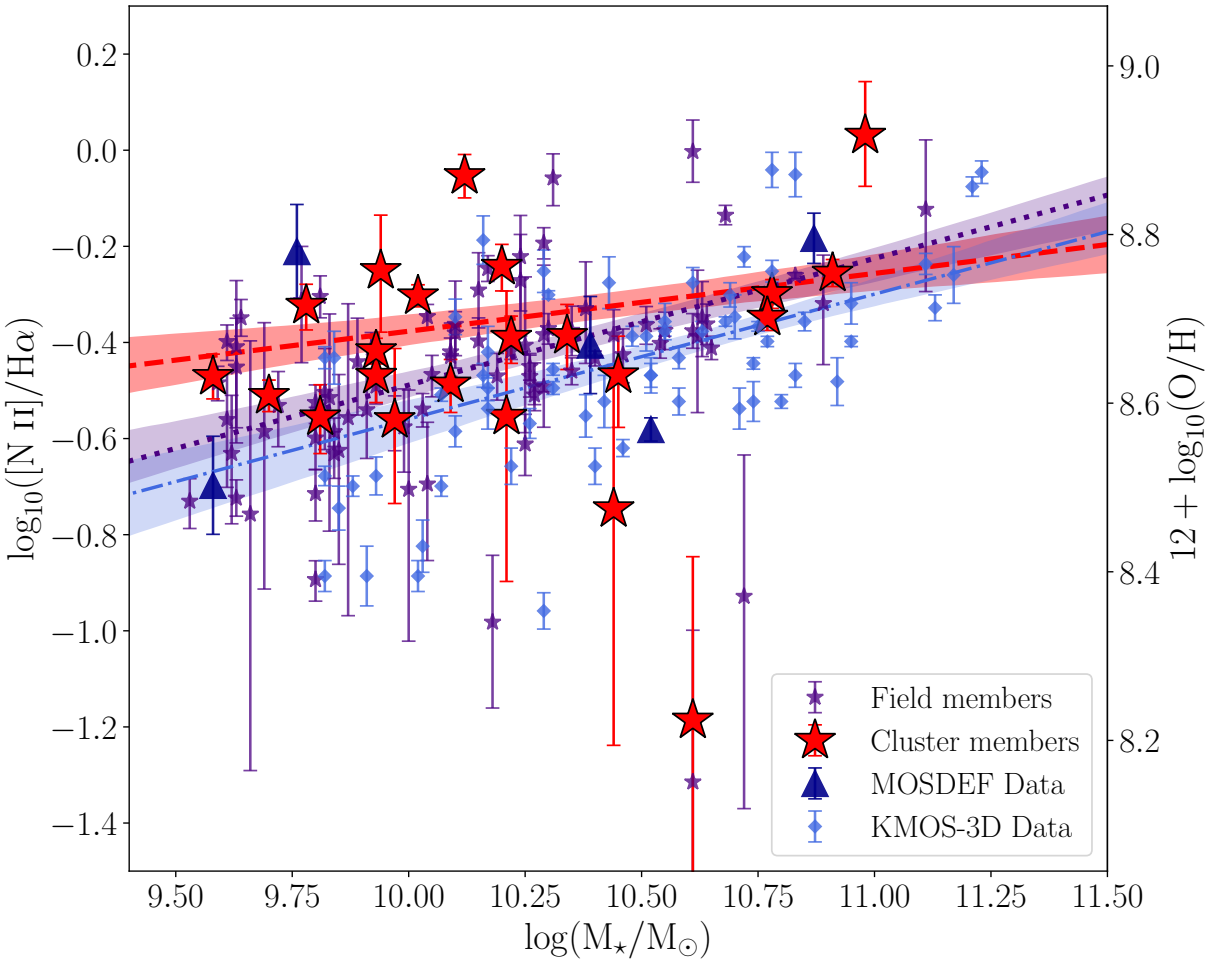


Figure 2.6: We show our [N II] /Hα ratio as a function of stellar mass. Our cluster is represented by the red stars while our field sample are the smaller purple stars. We again show MOSDEF and KMOS-3D as the blue triangles and diamonds respectively, and combine the best fits together as the blue line. We show the lines of best fit and the associated 1σ errors. At low masses, our cluster data exhibits higher line ratios (metallicity) than our field sample, as well as the MOSDEF+KMOS-3D field sample. The significance of the offset with MOSDEF+KMOS-3D is $\sim 3.5\sigma$ and 2σ compared to our field sample at a fixed stellar mass of $10^{10.2}M_{\odot}$.

The dominant scaling of metallicity is determined by the stellar mass and the FMR is characterized by how the scatter depends on SFR [145, 71]. In Figure 2.7, we show the offset between the data and the KMOS-3D field model, or residuals, as a function of star formation rate for each dataset. We use the same colouration as previous plots, with MOSDEF and KMOS-3D again combined into the same fit.

We find enhanced cluster line ratio residuals of 0.09 ± 0.05 with respect to our field sample at a fixed star formation rate of $10 M_{\odot} yr^{-1}$. For the KMOS-3D field, we measure a larger and more significant enhancement of cluster residuals of 0.15 ± 0.04 at the same SFR of $10 M_{\odot} yr^{-1}$. At SFRs $> 50 M_{\odot} yr^{-1}$, there is no significant offset, similar to the relationship with higher stellar mass. We also measure a small offset of 0.06 ± 0.03 between KMOS-3D and our field sample.

As an alternative way to consider the three-way relation of metallicity, star formation rate, and stellar mass, we show Figure 2.8 where we present [N II]/Hα as a function of stellar mass in four bins of Hα equivalent width: H$\alpha \leq 20$, $20 \leq$ H$\alpha \leq 40$, $40 \leq$ H$\alpha \leq 70$ and H$\alpha > 70$. We show MOSDEF as the blue triangles, KMOS-3D as the blue diamonds, our field sample as the purple stars, and our cluster sample as the red stars. We also show a $z \sim 0$ SDSS sample as the green contours.

Qualitatively, on average our cluster sample possesses enhanced metallicity compared to all field samples in every bin of equivalent width. The largest equivalent width objects have the largest offset in metallicity, contrary to previous the previous plots which showed no offset in metallicity at both high stellar mass and high star formation rate.

2.3 Discussion

2.3.1 No Environmental Dependence with Hα EW and SFR

In Section 2.2.1, we measured consistent equivalent widths relative to a variety of field samples, with Figure 2.4 showing the distribution of equivalent widths against MOSDEF and our field sample. We found no significant evidence for any offset relative to the field in equivalent width. In Section 2.2.2, we explored our measured SFR with field data from KMOS-3D [154], MOSDEF [79, 124], and our own field sample. Again, we found no significant offset relative to the field. We also split our sample at $z = 1$ in Figure A.10 and looked at the different distributions of equivalent widths between the field and cluster and again found no evidence for any offset.

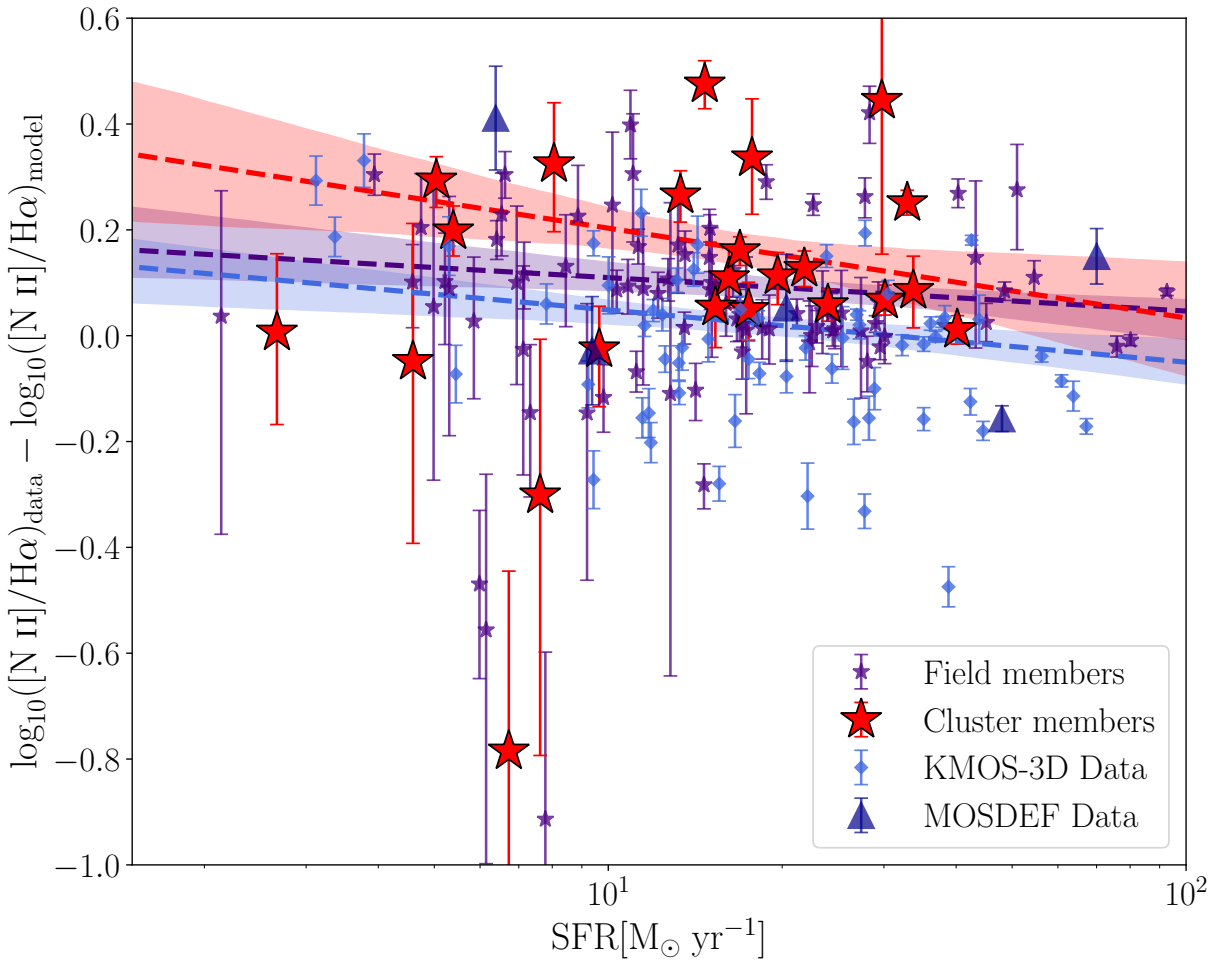


Figure 2.7: We show the difference between the KMOS-3D field model and our cluster and field samples as a function of star formation rate. In red, we show our cluster sample and in purple we show our field sample. The lines represent the lines of best fit and the 1σ confidence interval as the shaded region. We find significant (3.5σ) evidence for enhanced metallicities relative to the field MZR at a SFR of 10 $\mathrm{M}_\odot\,\mathrm{yr}^{-1}$. Note that H$\alpha$ is present on both axis and therefore produced correlated uncertainties. However, uncertainties on the measured SFR are small.

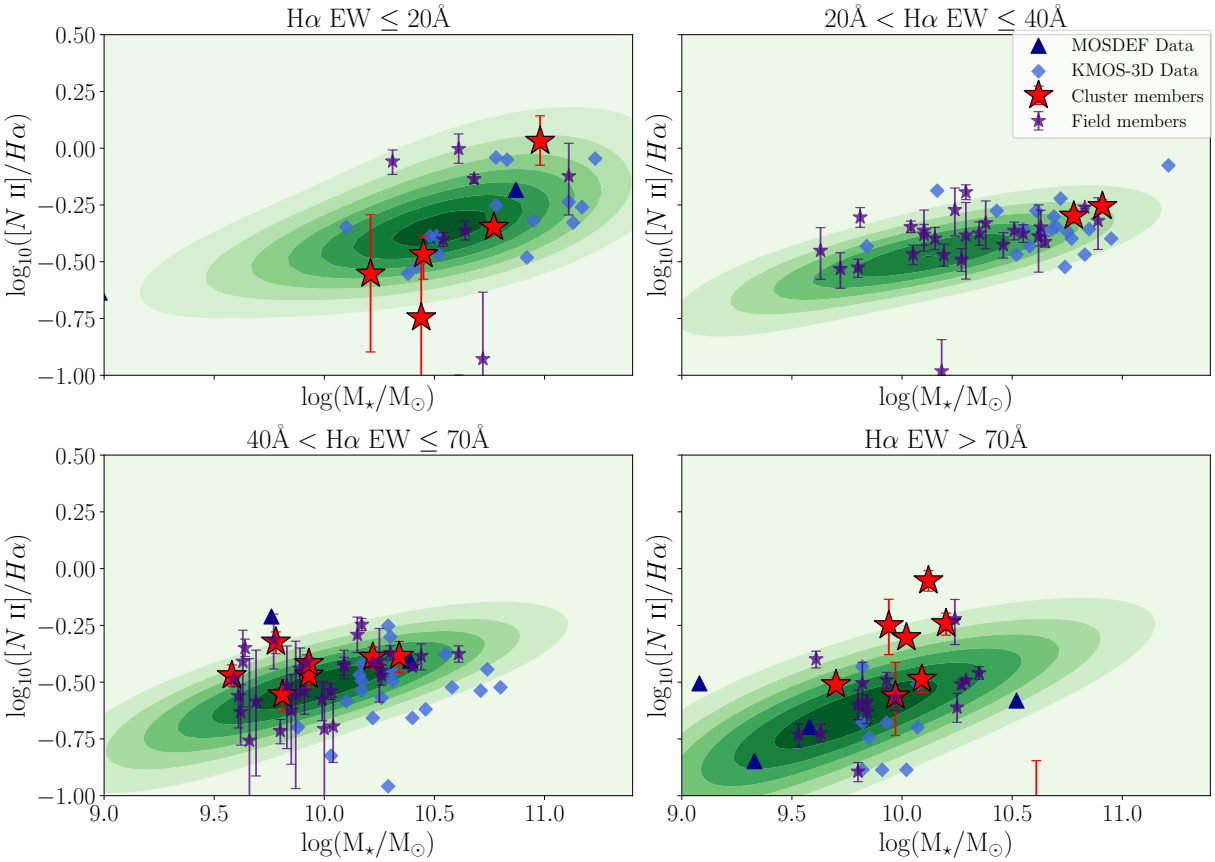


Figure 2.8: We show $[N\,\textsc{ii}]/H\alpha$ as a function of stellar mass, but we instead split the samples into different bins of Hα equivalent width. The colouration is the same as the previous plots, but we also introduce a $z \sim 0$ sample (SDSS) to increase the overall redshift range to observe any significant redshift dependence as redshift decreases. Hα equivalent width ranges of each bin are listed on the top of each plot. By splitting the data into equivalent width bins, we effectively eliminate the dependence of metallicity on equivalent width. MOSDEF is dominated by high equivalent width objects, and in the largest equivalent width bin we do see an offset. We find evidence of an offset in $[N\,\textsc{ii}]/H\alpha$ in each bin, with the significance increasing with increasing equivalent width.

While clusters generally have a lower fraction of star-forming galaxies, whether the SFMS depends on environment is still debated. While some studies find no significant dependence on environment [108, 106, 77, 49, 78, 137, 39, 33], some studies have found suppressed star formation rate in the clusters relative to their field counterparts [111, 151, 55, 115, 159]. While these different findings may be caused by systematics such as differing environment definitions, SFR tracers, or sample selection, they highlight this ongoing issue within galaxy evolution where there is no clear answer. Previous GOGREEN results utilizing the entire dataset have found suppressed star formation rate in the cluster relative to their field counterparts at lower stellar mass than we observed in this study [111]. However, we find no significant offset at any mass or redshift for our subset. Furthermore, because we are underrepresented at low SFR, we cannot dismiss the suppression of SFR in our sample, especially considering previous GOGREEN work has found cluster SFR suppression.

2.3.2 Evolution in the Cluster Metallicity offset relative to Field

We measure a significant offset in $\log([N\,\textsc{ii}]/H\alpha)$ within our own sample. We choose to measure the offset of our cluster sample relative to the combined fit of KMOS-3D, MOSDEF, and our own field sample. At a fixed stellar mass of $10^{10.2}$, we measure an offset in the $\log([\mathrm{N\,II}]/\mathrm{H}\alpha)$ line ratios relative to the combined fields of $0.126^{+0.037}_{-0.029}$.

We compare our work to samples from the literature over a wide redshift range. We compare to SDSS at $z \sim 0$ from [142] where the clusters are slightly enhanced compared to the field galaxies but highly significant. We also compare to [138] at $z \sim 0.4$ that have a negative offset but large errors that preclude strong conclusions. We compare with the work from [89] who found significant $\log([N\,\textsc{ii}]/H\alpha)$ ratio enhancement of 0.180 ± 0.047 dex within the galaxy cluster XMMXCS J2215.9-1738 at $z \sim 1.5$ compared to the field. We also compare with MOSDEF results from [29] at $z \sim 1.5$ and $z \sim 2.3$, where they found an enhancement of cluster metallicities at $z \sim 1.5$ relative to the field but an enhancement in field metallicities relative to the cluster at $z \sim 2.3$. Finally, we compare with ZFIRE from [107] at $z \sim 2.5$ where the field galaxies are again enhanced relative to their cluster counterparts.

In Figure 2.9, we show the offset between the cluster galaxies and field galaxies as a function of redshift, showing each sample along with our own. We measure the offset of each sample at $\log(M_*/\mathrm{M}_\odot) = 10.2$. We highlight our sample as the red star, where we find enhanced metallicities, consistent with [89] and [29] but at a slightly lower redshift. This offset has a turnover point somewhere around $z \sim 2$ after which the cluster population has reduced metallicities relative to the field.

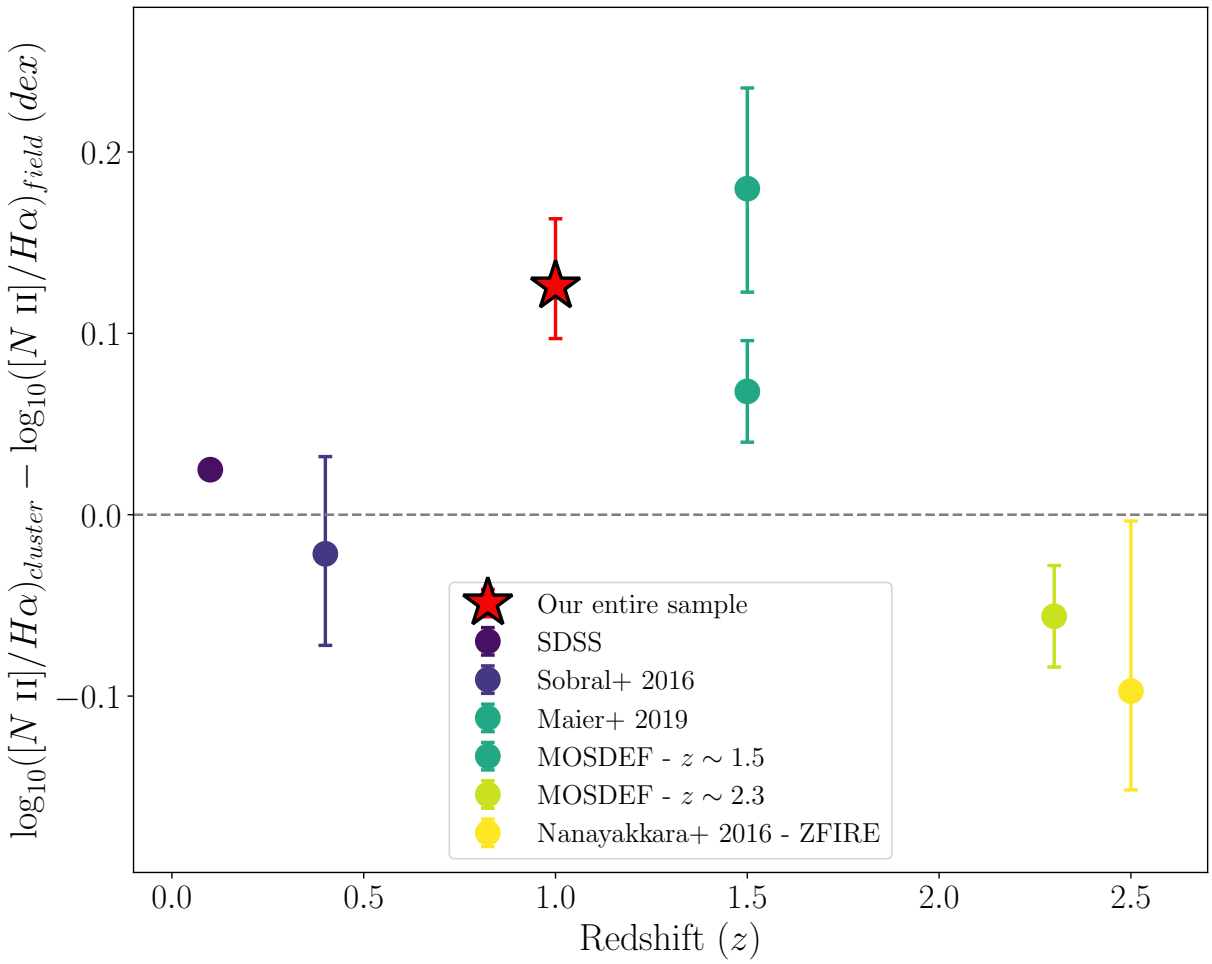


Figure 2.9: We show the offset between $[N\,\mathrm{II}]/H\alpha$ in the field and cluster as a function of redshift for different samples over a wide redshift range of $0 < z < 2.5$. For each dataset, the offset was measured at a fixed mass of $M = 10^{10.2} M_{\odot}$.

2.3.3 Interpretation

For simplicity, I am going to consider two simple models of environmental quenching. Ram pressure stripping predicts the removal of cold gas in the disk and the hot, infalling gas [56]. The removal of cold gas preferentially acts from the outside-in on timescales of $<$ 1Gyr [17]. Assuming that SFR scales with the amount of available gas, the SFR will decrease on a similar timescale. Any change in metallicity depends only on the strength of the existing metallicity gradient, assuming negligible contribution from the continued star formation. Thus, cluster galaxies should have lower SFR but similar metallicities to unperturbed field galaxies [51]. On the contrary, strangulation predicts that only the hot, infalling gas is removed; leaving the cold gas in the disk fully intact [80, 9]. Star formation continues normally for several Gyr, assuming the molecular gas is sufficiently replenished by H I. This is accompanied by an increase in metallicity as star formation continues in the absence of dilution from infalling gas [90]. Thus, cluster galaxies should have similar SFR but higher metallicities to unperturbed field galaxies. These simple, extreme models neglect many important effects. For example, ram pressure stripping may not only strip gas, but also compress it, leading to a short period of enhanced star formation [127, 126]. While inflows are stripped in both models, outflows are assumed to continue as normal which may not be the case [2, 5]. The rate of SFR decline in both models depends on how molecular gas supply is maintained as the H I gas is depleted. Therefore, quantitative distinction between the two models must go beyond these toy models.

My observations are consistent with slow quenching through reduced gas accretion, such as strangulation. If strangulation is indeed what we observe, we might expect the observed offset to be strongest at low SFR as a galaxy at low SFR will be further through the quenching process and possess enhanced metallicity [116, 146, 85]. We do not see such an offset in Figure 2.7. However, large uncertainties at SFR $<$ 10 $M_\odot$ yr^{-1} do not mean that the expected offset is absent. Furthermore, we targeted SF galaxies in this work and because the Hα detections were identified visually, the low SFR galaxies will be underrepresented. A larger sample that probes lower SFR will be required to further explore the dependence on SFR. Although with an automated line detection algorithm, I could try to put robust limits on Hα fluxes for non-detections. However, this would only be possible for galaxies with accurate spectroscopic redshifts.

Comparing to other literature samples, we see this enhancement in metallicities as a function of redshift in Figure 2.9. However, we must be cautious because although each sample was selected because they use [N II]/Hα as an indicator, they all have different selection functions and definitions of environment. Furthermore, statistical uncertainties for each sample are large. However, evidence is mounting that strangulation is in effect at $1 \leq z \leq 2$, and becomes less effective past $z \sim 2$. This is an interesting conclusion as this is the epoch of massive cluster assembly and before this time, the star formation rate of the Universe was at it's peak and the decrease to present day values is during this time.

For the surveys that are at local redshifts ($z \leq 0.5$), other environmental effects may be more favourable as the densities within the ICM are larger. While the large error bars of ref. [138] preclude any strong conclusions, SDSS shows a slight enhancement in cluster metallicities compared to the field. Ram pressure stripping can raise the average metallicity to a lesser extent than strangulation, which is consistent with this signature.

At $z \geq 2$, the offset between field and cluster metallicities potentially flips, such that the field possesses enhanced metallicities to the cluster. This could be attributed to higher accretion rates of galaxies in this epoch and efficient gas cooling in the early stages of cluster formation. Galaxies residing in groups or clusters possess higher fractions of pristine, low metallicity gas due to the higher accretion rates, which will in turn lower their gas-phase metallicity compared to their field counterparts. At lower redshifts ($z \lesssim 2$), the gas becomes metal-rich rapidly due to the suppression of pristine gas inflow by strangulation. This may explain the turnover point around $z \approx 2$. These results are consistent with the findings of ref. [29], and in simulation work [147, 57] where the lack of pristine gas accretion in cluster members has been observed.

2.4 Conclusion

I have presented a follow-up spectroscopic analysis of 8 clusters spanning $0.8 < z < 1.4$ selected from the GCLASS [106] and GOGREEN [10] surveys. I compare our measurements of SFR and metallicity with the field at the same redshift and using the same indicators of [N II] and Hα. My main conclusions are summarized as follows.

1. The Hα equivalent widths and star formation rates for our cluster population show no significant evidence of any environmental dependence relative to our own field sample and field samples from the literature at any stellar mass or redshift.

2. Our cluster sample possesses enhanced $\log([\text{N II}]/\text{H}\alpha)$ ratios relative to the combined fit of the literature field samples and our field sample of 0.126 ± 0.033.

3. The observed metallicity offset as a function of stellar mass is slightly dependent on the SFR. However, large error bars and the lack of low star formation rate galaxies preclude any strong conclusions.

Thus, these findings are consistent with a slow quenching model in which the accretion of metal-poor gas is reduced, such as in strangulation [96, 8]. Furthermore, this is mounting evidence for strangulation being the dominant quenching mechanisms at $1 < z < 2$ [e.g. 48, 65, 12, 13]. At $z < 1$, while the conditions for strangulation become even more favourable in massive clusters, the conditions for ram-pressure stripping may start to play a relatively larger role.

Although I interpret this signature as evidence for strangulation, I would like to note that the re-accretion of metal-rich outflows could also account for the enhancement in cluster metallicities. These two processes could be distinguished with stellar metallicities [116] and likely work in tandem to enhance the gas-phase metallicity [146].

Possible Improvements

This interpretation could be more robust with a larger sample size. Of our 326 unique galaxies observed, 121 had detectable $H\alpha$ emissions and following our cluster selection, 23 galaxies were a part of the cluster. As the emitters we determined visually from the 2D-spectra, galaxies with very small Hα emission were not included.

For future work, it may also prove useful to measure the metallicity with another method with smaller systematic uncertainties compared to N2. Ideally, this would be done with space based instruments, as the needed $[O\,\textsc{iii}]$ lines would be shifted to $\sim 10\,000$ Å at $z \sim 1$; putting much of our sample between photometric filters. While this work provides significant evidence for an offset in $[N\,\textsc{ii}]/H\alpha$, Figure 2.9 could be remade with other metallicity tracers which would fill in the redshift gap between $1.5 < z < 2$ to provide a clearer picture of the turnover point at $z \approx 2$.

References

[1] Kevork N. Abazajian, Jennifer K. Adelman-McCarthy, Marcel A. Agüeros, Sahar S. Allam, Carlos Allende Prieto, Deokkeun An, Kurt S. J. Anderson, Scott F. Anderson, James Annis, Neta A. Bahcall, C. A. L. Bailer-Jones, J. C. Barentine, Bruce A. Bassett, Andrew C. Becker, Timothy C. Beers, Eric F. Bell, Vasily Belokurov, Andreas A. Berlind, Eileen F. Berman, Mariangela Bernardi, Steven J. Bickerton, Dmitry Bizyaev, John P. Blakeslee, Michael R. Blanton, John J. Bochanski, William N. Boroski, Howard J. Brewington, Jarle Brinchmann, J. Brinkmann, Robert J. Brunner, Tamás Budavári, Larry N. Carey, Samuel Carliles, Michael A. Carr, Francisco J. Castander, David Cinabro, A. J. Connolly, István Csabai, Carlos E. Cunha, Paul C. Czarapata, James R. A. Davenport, Ernst de Haas, Ben Dilday, Mamoru Doi, Daniel J. Eisenstein, Michael L. Evans, N. W. Evans, Xiaohui Fan, Scott D. Friedman, Joshua A. Frieman, Masataka Fukugita, Boris T. Gänsicke, Evalyn Gates, Bruce Gillespie, G. Gilmore, Belinda Gonzalez, Carlos F. Gonzalez, Eva K. Grebel, James E. Gunn, Zsuzsanna Györy, Patrick B. Hall, Paul Harding, Frederick H. Harris, Michael Harvanek, Suzanne L. Hawley, Jeffrey J. E. Hayes, Timothy M. Heckman, John S. Hendry, Gregory S. Hennessy, Robert B. Hindsley, J. Hoblitt, Craig J. Hogan, David W. Hogg, Jon A. Holtzman, Joseph B. Hyde, Shinichi Ichikawa, Takashi Ichikawa, Myungshin Im, Željko Ivezić, Sebastian Jester, Linhua Jiang, Jennifer A. Johnson, Anders M. Jorgensen, Mario Jurić, Stephen M. Kent, R. Kessler, S. J. Kleinman, G. R. Knapp, Kohki Konishi, Richard G. Kron, Jurek Krzesinski, Nikolay Kuropatkin, Hubert Lampeitl, Svetlana Lebedeva, Myung Gyoon Lee, Young Sun Lee, R. French Leger, Sébastien Lépine, Nolan Li, Marcos Lima, Huan Lin, Daniel C. Long, Craig P. Loomis, Jon Loveday, Robert H. Lupton, Eugene Magnier, Olena Malanushenko, Viktor Malanushenko, Rachel Mandelbaum, Bruce Margon, John P. Marriner, David Martínez-Delgado, Takahiko Matsubara, Peregrine M. McGehee, Timothy A. McKay, Avery Meiksin, Heather L. Morrison, Fergal Mullally, Jeffrey A. Munn, Tara Murphy, Thomas Nash, Ada Nebot, Eric H. Neilsen, Jr., Heidi Jo Newberg, Peter R. Newman, Robert C. Nichol, Tom Nicin-

ski, Maria Nieto-Santisteban, Atsuko Nitta, Sadanori Okamura, Daniel J. Oravetz, Jeremiah P. Ostriker, Russell Owen, Nikhil Padmanabhan, Kaike Pan, Changbom Park, George Pauls, John Peoples, Jr., Will J. Percival, Jeffrey R. Pier, Adrian C. Pope, Dimitri Pourbaix, Paul A. Price, Norbert Purger, Thomas Quinn, M. Jordan Raddick, Paola Re Fiorentin, Gordon T. Richards, Michael W. Richmond, Adam G. Riess, Hans-Walter Rix, Constance M. Rockosi, Masao Sako, David J. Schlegel, Donald P. Schneider, Ralf-Dieter Scholz, Matthias R. Schreiber, Axel D. Schwope, Uroš Seljak, Branimir Sesar, Erin Sheldon, Kazu Shimasaku, Valena C. Sibley, A. E. Simmons, Thirupathi Sivarani, J. Allyn Smith, Martin C. Smith, Vernesa Smolčić, Stephanie A. Snedden, Albert Stebbins, Matthias Steinmetz, Chris Stoughton, Michael A. Strauss, Mark SubbaRao, Yasushi Suto, Alexander S. Szalay, István Szapudi, Paula Szkody, Masayuki Tanaka, Max Tegmark, Luis F. A. Teodoro, Aniruddha R. Thakar, Christy A. Tremonti, Douglas L. Tucker, Alan Uomoto, Daniel E. Vanden Berk, Jan Vandenberg, S. Vidrih, Michael S. Vogeley, Wolfgang Voges, Nicole P. Vogt, Yogesh Wadadekar, Shannon Watters, David H. Weinberg, Andrew A. West, Simon D. M. White, Brian C. Wilhite, Alainna C. Wonders, Brian Yanny, and D. R. Yocum. The Seventh Data Release of the Sloan Digital Sky Survey. *apjs*, 182(2):543–558, June 2009. _eprint: 0812.0649.

[2] Kota Adachi, Tadayuki Kodama, Jose Manuel Pérez-Martínez, Tomoko L. Suzuki, and Masato Onodera. Enhanced gas-phase metallicities and suppressed outflows for galaxies in a rich cluster core at cosmic noon, June 2025. arXiv:2506.01088 [astro-ph.GA] version: 1.

[3] D. Alloin, S. Collin-Souffrin, M. Joly, and L. Vigroux. Nitrogen and oxygen abundances in galaxies. *Astronomy and Astrophysics*, 78:200–216, September 1979. ADS Bibcode: 1979A&A....78..200A.

[4] Brett H. Andrews and Paul Martini. The Mass-Metallicity Relation with the Direct Method on Stacked Spectra of SDSS Galaxies. *The Astrophysical Journal*, 765:140, March 2013. ADS Bibcode: 2013ApJ...765..140A.

[5] Amy Attwater, Barbara Catinella, Luca Cortese, Timothy Davis, Toby Brown, A. Fraser-McKelvie, Andrew Battisti, Alessandro Boselli, Pavel Jáchym, Andrei Ristea, Kristine Spekkens, Sabine Thater, and Christine Wilson. MAUVE-MUSE: A Star Formation-driven Outflow Caught in the Act of Quenching the Stripped Virgo Galaxy NGC 4064, December 2025. arXiv:2512.10574 [astro-ph.GA].

[6] J. A. Baldwin, M. M. Phillips, and R. Terlevich. Classification parameters for the

emission-line spectra of extragalactic objects. *Publications of the Astronomical Society of the Pacific*, 93:5–19, February 1981. ADS Bibcode: 1981PASP...93....5B.

[7] Michael Balogh, Vince Eke, Chris Miller, Ian Lewis, Richard Bower, Warrick Couch, Robert Nichol, Joss Bland-Hawthorn, Ivan K. Baldry, Carlton Baugh, Terry Bridges, Russell Cannon, Shaun Cole, Matthew Colless, Chris Collins, Nicholas Cross, Gavin Dalton, Roberto de Propris, Simon P. Driver, George Efstathiou, Richard S. Ellis, Carlos S. Frenk, Karl Glazebrook, Percy Gomez, Alex Gray, Edward Hawkins, Carole Jackson, Ofer Lahav, Stuart Lumsden, Steve Maddox, Darren Madgwick, Peder Norberg, John A. Peacock, Will Percival, Bruce A. Peterson, Will Sutherland, and Keith Taylor. Galaxy ecology: groups and low-density environments in the SDSS and 2dFGRS. *mnras*, 348(4):1355–1372, March 2004. _eprint: astro-ph/0311379.

[8] Michael L. Balogh, Sean L. McGee, Angus Mok, Adam Muzzin, Remco F. J. van der Burg, Richard G. Bower, Alexis Finoguenov, Henk Hoekstra, Chris Lidman, John S. Mulchaey, Allison Noble, Laura C. Parker, Masayuki Tanaka, David J. Wilman, Tracy Webb, Gillian Wilson, and Howard K. C. Yee. Evidence for a change in the dominant satellite galaxy quenching mechanism at z = 1. *Monthly Notices of the Royal Astronomical Society*, 456:4364–4376, March 2016. ADS Bibcode: 2016MNRAS.456.4364B.

[9] Michael L. Balogh, Julio F. Navarro, and Simon L. Morris. The Origin of Star Formation Gradients in Rich Galaxy Clusters. *apj*, 540(1):113–121, September 2000. _eprint: astro-ph/0004078.

[10] Michael L. Balogh, Remco F. J. van der Burg, Adam Muzzin, Gregory Rudnick, Gillian Wilson, Kristi Webb, Andrea Biviano, Kevin Boak, Pierluigi Cerulo, Jeffrey Chan, M. C. Cooper, David G. Gilbank, Stephen Gwyn, Chris Lidman, Jasleen Matharu, Sean L. McGee, Lyndsay Old, Irene Pintos-Castro, Andrew M. M. Reeves, Heath Shipley, Benedetta Vulcani, Howard K. C. Yee, M. Victoria Alonso, Callum Bellhouse, Kevin C. Cooke, Anna Davidson, Gabriella De Lucia, Ricardo Demarco, Nicole Drakos, Sean P. Fillingham, Alexis Finoguenov, Ben Forrest, Caelan Golledge, Pascale Jablonka, Diego Lambas Garcia, Karen McNab, Hernan Muriel, Julie B. Nantais, Allison Noble, Laura C. Parker, Grayson Petter, Bianca M. Poggianti, Melinda Townsend, Carlos Valotto, Tracy Webb, and Dennis Zaritsky. The GOGREEN and GCLASS surveys: first data release. *mnras*, 500(1):358–387, January 2021. _eprint: 2009.13345.

[11] Filippo Barbani, Raffaele Pascale, Federico Marinacci, Paul Torrey, Laura V. Sales, Hui Li, and Mark Vogelsberger. Understanding the baryon cycle: Fueling star for-

mation via inflows in Milky Way-like galaxies. *Astronomy & Astrophysics*, 697:A121, May 2025.

[12] Devontae Baxter, Michael Cooper, Michael Balogh, Tim Carleton, Pierluigi Cerulo, Gabriella De Lucia, Ricardo Demarco, Sean McGee, Adam Muzzin, Julie Nantais, Irene Pintos Castro, Andrew Reeves, Gregory Rudnick, Florian Sarron, Remco van der Burg, Benedetta Vulcani, Gillian Wilson, and Dennis Zaritsky. The GOGREEN Survey: Constraining the Satellite Quenching Timescale in Massive Clusters at $\boldsymbol{z} \gtrsim 1$. *Monthly Notices of the Royal Astronomical Society*, 515(4):5479–5494, August 2022. arXiv:2207.14302 [astro-ph.GA].

[13] Devontae C. Baxter, Michael C. Cooper, Michael L. Balogh, Gregory H. Rudnick, Gabriella De Lucia, Ricardo Demarco, Alexis Finoguenov, Ben Forrest, Adam Muzzin, Andrew Reeves, Florian Sarron, Benedetta Vulcani, Gillian Wilson, and Dennis Zaritsky. When the Well Runs Dry: Modeling Environmental Quenching of High-mass Satellites in Massive Clusters at \boldmath$z \gtrsim 1$. *Monthly Notices of the Royal Astronomical Society*, 526(3):3716–3729, October 2023. arXiv:2306.09404 [astro-ph.GA].

[14] Yuval Birnboim, Avishai Dekel, and Eyal Neistein. Bursting and quenching in massive galaxies without major mergers or AGNs. *Monthly Notices of the Royal Astronomical Society*, 380(1):339–352, August 2007. _eprint: https://academic.oup.com/mnras/article-pdf/380/1/339/4151465/mnras0380-0339.pdf.

[15] Asa F. L. Bluck, Joanna M. Piotrowska, and Roberto Maiolino. The Fundamental Signature of Star Formation Quenching from AGN Feedback: A Critical Dependence of Quiescence on Supermassive Black Hole Mass, Not Accretion Rate. *The Astrophysical Journal*, 944(1):108, February 2023.

[16] Alberto D. Bolatto, Mark Wolfire, and Adam K. Leroy. The CO-to-H2 Conversion Factor. *Annual Review of Astronomy and Astrophysics*, 51(Volume 51, 2013):207–268, August 2013.

[17] Alessandro Boselli, Matteo Fossati, and Ming Sun. Ram pressure stripping in high-density environments. *The Astronomy and Astrophysics Review*, 30(1), May 2022.

[18] N. Bouché, A. Dekel, R. Genzel, S. Genel, G. Cresci, N. M. Förster Schreiber, K. L. Shapiro, R. I. Davies, and L. Tacconi. The Impact of Cold Gas Accretion Above

a Mass Floor on Galaxy Scaling Relations. *apj*, 718(2):1001–1018, August 2010. _eprint: 0912.1858.

[19] J. Bovy. *Dynamics and Astrophysics of Galaxies*. Princeton University Press, Princeton, NJ, 2026.

[20] J. Brinchmann, S. Charlot, S. D. M. White, C. Tremonti, G. Kauffmann, T. Heckman, and J. Brinkmann. The physical properties of star-forming galaxies in the low-redshift Universe. *Monthly Notices of the Royal Astronomical Society*, 351(4):1151–1179, July 2004.

[21] G. Buldgen, A. Noels, V. A. Baturin, A. V. Oreshina, S. V. Ayukov, R. Scuflaire, A. M. Amarsi, and N. Grevesse. Helioseismic determination of the solar metal mass fraction. *Astronomy & Astrophysics*, 681:A57, January 2024.

[22] G. Buldgen, A. Noels, R. Scuflaire, A. M. Amarsi, N. Grevesse, P. Eggenberger, J. Colgan, C. J. Fontes, V. A. Baturin, A. V. Oreshina, S. V. Ayukov, P. Hakel, and D. P. Kilcrease. In-depth analysis of solar models with high-metallicity abundances and updated opacity tables. *Astronomy & Astrophysics*, 686:A108, June 2024.

[23] Daniela Calzetti, Lee Armus, Ralph C. Bohlin, Anne L. Kinney, Jan Koornneef, and Thaisa Storchi-Bergmann. The Dust Content and Opacity of ActivelyStar-forming Galaxies*. *The Astrophysical Journal*, 533(2):682, April 2000.

[24] Daniela Calzetti, Anne L. Kinney, and Thaisa Storchi-Bergmann. Dust Extinction of the Stellar Continua in Starburst Galaxies: The Ultraviolet and Optical Extinction Law. *The Astrophysical Journal*, 429:582, July 1994. ADS Bibcode: 1994ApJ...429..582C.

[25] A C Carnall, D J McLeod, R J McLure, J S Dunlop, R Begley, F Cullen, C T Donnan, M L Hamadouche, S M Jewell, E W Jones, C L Pollock, and V Wild. A surprising abundance of massive quiescent galaxies at 3 <z< 5 in the first data from*JWST*CEERS. *Monthly Notices of the Royal Astronomical Society*, 520(3):3974–3985, February 2023.

[26] M. Cerviño and D. Valls-Gabaud. On biases in the predictions of stellar population synthesis models. *Monthly Notices of the Royal Astronomical Society*, 338(2):481–496, January 2003.

[27] Gilles Chabrier. Galactic Stellar and Substellar Initial Mass Function. *Publications of the Astronomical Society of the Pacific*, 115(809):763–795, July 2003.

[28] Stéphane Charlot and S. Michael Fall. A Simple Model for the Absorption of Starlight by Dust inGalaxies. *The Astrophysical Journal*, 539(2):718, August 2000.

[29] Nima Chartab, Bahram Mobasher, Alice E. Shapley, Irene Shivaei, Ryan L. Sanders, Alison L. Coil, Mariska Kriek, Naveen A. Reddy, Brian Siana, William R. Freeman, Mojegan Azadi, Guillermo Barro, Tara Fetherolf, Gene Leung, Sedona H. Price, and Tom Zick. The MOSDEF Survey: Environmental Dependence of the Gas-phase Metallicity of Galaxies at 1.4 z 2.6*. *The Astrophysical Journal*, 908(2):120, February 2021.

[30] Yaoxin Chen, Xi Kang, Hong Guo, Hou-Zun Chen, and Jiafeng Lu. Unveiling the galactic baryon cycle process by an empirical model, July 2025.

[31] G. W. Collins, II. *The virial theorem in stellar astrophysics*. January 1978. Publication Title: Astronomy and Astrophysics Series ADS Bibcode: 1978vtsa.book.....C.

[32] Charlie Conroy. Modeling the Panchromatic Spectral Energy Distributions of Galaxies. *Annual Review of Astronomy and Astrophysics*, 51(1):393–455, August 2013. arXiv:1301.7095 [astro-ph.CO].

[33] Jennifer R Cooper, Gregory H Rudnick, Gabriel G Brammer, Tyler Desjardins, Justin L Mann, Benjamin J Weiner, Alfonso Aragón-Salamanca, Gabriella De Lucia, Vandana Desai, Rose A Finn, Pascale Jablonka, Yara L Jaffé, John Moustakas, Damien Spérone-Longin, Harry I Teplitz, Benedetta Vulcani, and Dennis Zaritsky. H -based star formation rates in and around z 0.5 EDisCS clusters. *Monthly Notices of the Royal Astronomical Society*, 509(4):5382–5398, November 2021.

[34] G. Cresci, F. Mannucci, and M. Curti. Fundamental metallicity relation in CALIFA, SDSS-IV MaNGA, and high-z galaxies. *Astronomy & Astrophysics*, 627:A42, June 2019.

[35] M. Curti, G. Cresci, F. Mannucci, A. Marconi, R. Maiolino, and S. Esposito. New fully empirical calibrations of strong-line metallicity indicators in star-forming galaxies. *Monthly Notices of the Royal Astronomical Society*, 465(2):1384–1400, February 2017.

[36] Mirko Curti, Francesco D'Eugenio, Stefano Carniani, Roberto Maiolino, Lester Sandles, Joris Witstok, William M Baker, Jake S Bennett, Joanna M Piotrowska, Sandro Tacchella, Stephane Charlot, Kimihiko Nakajima, Gabriel Maheson, Filippo Mannucci, Amirnezam Amiri, Santiago Arribas, Francesco Belfiore, Nina R Bonaventura,

Andrew J Bunker, Jacopo Chevallard, Giovanni Cresci, Emma Curtis-Lake, Connor Hayden-Pawson, Gareth C Jones, Nimisha Kumari, Isaac Laseter, Tobias J Looser, Alessandro Marconi, Michael V Maseda, Jan Scholtz, Renske Smit, Hannah Übler, and Imaan E B Wallace. The chemical enrichment in the early Universe as probed by JWST via direct metallicity measurements at z 8. *Monthly Notices of the Royal Astronomical Society*, 518(1):425–438, January 2023.

[37] Mirko Curti, Filippo Mannucci, Giovanni Cresci, and Roberto Maiolino. The mass–metallicity and the fundamental metallicity relation revisited on a fully T_e-based abundance scale for galaxies. *Monthly Notices of the Royal Astronomical Society*, 491(1):944–964, November 2019.

[38] Daniel A. Dale, Mederic Boquien, Jordan A. Turner, Daniela Calzetti, Robert C. Kennicutt, and Janice C. Lee. Spectral Energy Distributions for 258 Local Volume Galaxies. *The Astronomical Journal*, 165(6):260, June 2023. arXiv:2304.12491 [astro-ph.GA].

[39] B. Darvish, D. Sobral, B. Mobasher, N. Z. Scoville, P. Best, L. V. Sales, and I. Smail. COSMIC WEB AND STAR FORMATION ACTIVITY IN GALAXIES AT z 1. *The Astrophysical Journal*, 796(1):51, November 2014.

[40] Romeel Davé, Kristian Finlator, and Benjamin D. Oppenheimer. An analytic model for the evolution of the stellar, gas and metal content of galaxies: An analytic model for galaxy evolution. *Monthly Notices of the Royal Astronomical Society*, pages no–no, December 2011.

[41] Anna de Graaff, Hans-Walter Rix, Stefano Carniani, Katherine A. Suess, Stéphane Charlot, Emma Curtis-Lake, Santiago Arribas, William M. Baker, Kristan Boyett, Andrew J. Bunker, Alex J. Cameron, Jacopo Chevallard, Mirko Curti, Daniel J. Eisenstein, Marijn Franx, Kevin Hainline, Ryan Hausen, Zhiyuan Ji, Benjamin D. Johnson, Gareth C. Jones, Roberto Maiolino, Michael V. Maseda, Erica Nelson, Eleonora Parlanti, Tim Rawle, Brant Robertson, Sandro Tacchella, Hannah Übler, Christina C. Williams, Christopher N. A. Willmer, and Chris Willott. Ionised gas kinematics and dynamical masses of z 6 galaxies from JADES/NIRSpec high-resolution spectroscopy. *Astronomy and Astrophysics*, 684:A87, April 2024. ADS Bibcode: 2024A&A...684A..87D.

[42] Megan Donahue and G. Mark Voit. Baryon Cycles in the Biggest Galaxies, April 2022.

[43] Martina Donnari, Annalisa Pillepich, Gandhali D Joshi, Dylan Nelson, Shy Genel, Federico Marinacci, Vicente Rodriguez-Gomez, Rüdiger Pakmor, Paul Torrey, Mark Vogelsberger, and Lars Hernquist. Quenched fractions in the IllustrisTNG simulations: the roles of AGN feedback, environment, and pre-processing. *Monthly Notices of the Royal Astronomical Society*, 500(3):4004–4024, October 2020. _eprint: https://academic.oup.com/mnras/article-pdf/500/3/4004/34695286/staa3006.pdf.

[44] B. T. Draine. Interstellar Dust Grains. *Annual Review of Astronomy and Astrophysics*, 41(1):241–289, September 2003. arXiv:astro-ph/0304489.

[45] Bruce G. Elmegreen, Ralf S. Klessen, and Christine D. Wilson. On the Constancy of the Characteristic Mass of Young Stars. *The Astrophysical Journal*, 681(1):365–374, July 2008. arXiv:0803.4411 [astro-ph].

[46] Kristoffer A. Eriksen, Jack Hughes, Christopher J. Fontes, James P. Colgan, Aimee L. Hungerford, Christopher L. Fryer, Honglin Zhang, Carles Badenes, and Patrick Slane. Progress in Understanding Iron Peak Elements in Young Supernova Remnants. Technical Report LA-UR-13-27127, Los Alamos National Laboratory (LANL), September 2013.

[47] Gao Feng, Kong Xu, Lin Xuan-bin, Zhang Wei, and Li Jun-rong. A Study of the [OII]3727/H Flux Ratio of Emission Line Galaxies. *Chinese Astronomy and Astrophysics*, 34(3):234–244, 2010.

[48] Sean P. Fillingham, Michael C. Cooper, Coral Wheeler, Shea Garrison-Kimmel, Michael Boylan-Kolchin, and James S. Bullock. Taking care of business in a flash : constraining the time-scale for low-mass satellite quenching with ELVIS. *Monthly Notices of the Royal Astronomical Society*, 454(2):2039–2049, October 2015.

[49] Rose A. Finn, Michael L. Balogh, Dennis Zaritsky, Christopher J. Miller, and Robert C. Nichol. Mass and Redshift Dependence of Star Formation in Relaxed Galaxy Clusters. *The Astrophysical Journal*, 679(1):279–292, May 2008.

[50] Daniel Foreman-Mackey, David W. Hogg, Dustin Lang, and Jonathan Goodman. <tt>emcee</tt>: The MCMC Hammer. *Publications of the Astronomical Society of the Pacific*, 125(925):306–312, March 2013.

[51] Andrea Franchetto, Benedetta Vulcani, Bianca M. Poggianti, Marco Gullieuszik, Matilde Mingozzi, Alessia Moretti, Neven Tomičić, Jacopo Fritz, Daniela Bettoni,

and Yara L. Jaffé. GASP XXVII: Gas-phase metallicity scaling relations in disk galaxies with and without ram-pressure stripping. *The Astrophysical Journal*, 895(2):106, June 2020. arXiv:2004.11917 [astro-ph.GA].

[52] J. M. Gabor and R. Davé. Hot gas in massive haloes drives both mass quenching and environment quenching. *Monthly Notices of the Royal Astronomical Society*, 447(1):374–391, December 2014. _eprint: https://academic.oup.com/mnras/article-pdf/447/1/374/4908737/stu2399.pdf.

[53] J. S. Gallagher, H. Bushouse, and D. A. Hunter. Star Formation Rates and [O II] Emission in Blue Galaxies. *The Astronomical Journal*, 97:700, March 1989. ADS Bibcode: 1989AJ.....97..700G.

[54] David G. Gilbank, Ivan K. Baldry, Michael L. Balogh, Karl Glazebrook, and Richard G. Bower. The local star formation rate density: assessing calibrations using [OII], H and UV luminosities. *Monthly Notices of the Royal Astronomical Society*, 405:2594–2614, July 2010. ADS Bibcode: 2010MNRAS.405.2594G.

[55] Ruth Grützbauch, Amanda E. Bauer, Inger Jørgensen, and Jesus Varela. Suppression of star formation in the central 200 kpc of a z= 1.4 galaxy cluster. *Monthly Notices of the Royal Astronomical Society*, 423(4):3652–3662, July 2012. _eprint: https://academic.oup.com/mnras/article-pdf/423/4/3652/17335440/mnras0423-3652.pdf.

[56] James E. Gunn and J. Richard Gott, III. On the Infall of Matter Into Clusters of Galaxies and Some Effects on Their Evolution. *apj*, 176:1, August 1972.

[57] Anshu Gupta, Tiantian Yuan, Paul Torrey, Mark Vogelsberger, Davide Martizzi, Kim-Vy H. Tran, Lisa J. Kewley, Federico Marinacci, Dylan Nelson, Annalisa Pillepich, Lars Hernquist, Shy Genel, and Volker Springel. Chemical pre-processing of cluster galaxies over the past 10 billion years in the IllustrisTNG simulations. *Monthly Notices of the Royal Astronomical Society*, 477:L35–L39, June 2018. ADS Bibcode: 2018MNRAS.477L..35G.

[58] Christine Hall, Stéphane Courteau, Thomas Jarrett, Michelle Cluver, Gerhardt Meurer, Claude Carignan, and Fiona Audcent-Ross. Unique Tracks Drive the Scatter of the Spatially Resolved Star Formation Main Sequence. *The Astrophysical Journal*, 865(2):154, October 2018.

[59] R. B. C. Henry, M. G. Edmunds, and J. Köppen. On the Cosmic Origins of Carbon and Nitrogen. *The Astrophysical Journal*, 541(2):660, October 2000.

[60] Philip F. Hopkins, Eliot Quataert, and Norman Murray. Stellar feedback in galaxies and the origin of galaxy-scale winds. *Monthly Notices of the Royal Astronomical Society*, 421(4):3522–3537, April 2012.

[61] Y. I. Izotov, G. Stasińska, G. Meynet, N. G. Guseva, and T. X. Thuan. The chemical composition of metal-poor emission-line galaxies in the Data Release 3 of the Sloan Digital Sky Survey. *Astronomy and Astrophysics*, 448:955–970, March 2006. ADS Bibcode: 2006A&A...448..955I.

[62] T. H. Jarrett. Near-Infrared Galaxy Morphology Atlas. *Publications of the Astronomical Society of the Pacific*, 112:1008–1080, August 2000. ADS Bibcode: 2000PASP..112.1008J.

[63] Peter M. W. Kalberla and Jürgen Kerp. The Hi Distribution of the Milky Way. *Annual Review of Astronomy and Astrophysics*, 47(Volume 47, 2009):27–61, September 2009.

[64] H. Karttunen, P. Kröger, H. Oja, M. Poutanen, and K.J. Donner. *Fundamental Astronomy*. Physics and Astronomy Online Library. Springer Berlin Heidelberg, 2003.

[65] Lalitwadee Kawinwanichakij, Casey Papovich, Ryan F. Quadri, Karl Glazebrook, Glenn G. Kacprzak, Rebecca J. Allen, Eric F. Bell, Darren J. Croton, Avishai Dekel, Henry C. Ferguson, Ben Forrest, Norman A. Grogin, Yicheng Guo, Dale D. Kocevski, Anton M. Koekemoer, Ivo Labbé, Ray A. Lucas, Themiya Nanayakkara, Lee R. Spitler, Caroline M. S. Straatman, Kim-Vy H. Tran, Adam Tomczak, and Pieter van Dokkum. Effect of local environment and stellar mass on galaxy quenching and morphology at \$0.5<z<2.0\$. *The Astrophysical Journal*, 847(2):134, October 2017. arXiv:1706.03780 [astro-ph.GA].

[66] Robert C. Kennicutt. STAR FORMATION IN GALAXIES ALONG THE HUBBLE SEQUENCE. *Annual Review of Astronomy and Astrophysics*, 36(1):189–231, September 1998.

[67] Robert C. Kennicutt and Neal J. Evans. Star Formation in the Milky Way and Nearby Galaxies. *Annual Review of Astronomy and Astrophysics*, 50:531–608, September 2012. ADS Bibcode: 2012ARA&A..50..531K.

[68] Robert C. Kennicutt, Jr. The Integrated Spectra of Nearby Galaxies: General Properties and Emission-Line Spectra. *The Astrophysical Journal*, 388:310, April 1992. ADS Bibcode: 1992ApJ...388..310K.

[69] Robert C. Kennicutt, Jr., Peter Tamblyn, and Charles E. Congdon. Past and Future Star Formation in Disk Galaxies. *The Astrophysical Journal*, 435:22, November 1994. ADS Bibcode: 1994ApJ...435...22K.

[70] L. J. Kewley and M. A. Dopita. Using Strong Lines to Estimate Abundances in Extragalactic H II Regions and Starburst Galaxies. *The Astrophysical Journal Supplement Series*, 142:35–52, September 2002. ADS Bibcode: 2002ApJS..142...35K.

[71] Lisa J. Kewley and Sara L. Ellison. Metallicity Calibrations and the Mass-Metallicity Relation for Star-forming Galaxies. *The Astrophysical Journal*, 681(2):1183, July 2008.

[72] Lisa J. Kewley, Margaret J. Geller, and Rolf A. Jansen. [O II] as a Star Formation Rate Indicator. *The Astronomical Journal*, 127(4):2002, April 2004.

[73] Lisa J. Kewley, Rolf A. Jansen, and Margaret J. Geller. Aperture Effects on Star Formation Rate, Metallicity, and Reddening. *Publications of the Astronomical Society of the Pacific*, 117(829):227, March 2005.

[74] Lisa J. Kewley, David C. Nicholls, and Ralph S. Sutherland. Understanding Galaxy Evolution Through Emission Lines. *Annual Review of Astronomy and Astrophysics*, 57:511–570, August 2019. ADS Bibcode: 2019ARA&A..57..511K.

[75] Jeong-Gyu Kim, Eve C. Ostriker, and Nina Filippova. Star Formation Efficiency and Dispersal of Giant Molecular Clouds with UV Radiation Feedback: Dependence on Gravitational Boundedness and Magnetic Fields. *The Astrophysical Journal*, 911(2):128, April 2021.

[76] Henry A. Kobulnicky, Jr Robert C. Kennicutt, and James L. Pizagno. On Measuring Nebular Chemical Abundances in Distant Galaxies Using Global Emission-Line Spectra. *The Astrophysical Journal*, 514(2):544, April 1999.

[77] T. Kodama, M. L. Balogh, I. Smail, R. G. Bower, and F. Nakata. A panoramic H imaging survey of the z= 0.4 cluster Cl 0024.0+1652 with Subaru. *Monthly Notices of the Royal Astronomical Society*, 354(4):1103–1119, November 2004.

[78] Yusei Koyama, Ian Smail, Jaron Kurk, James E. Geach, David Sobral, Tadayuki Kodama, Fumiaki Nakata, A. M. Swinbank, Philip N. Best, Masao Hayashi, and Kenichi Tadaki. On the evolution and environmental dependence of the star formation rate versus stellar mass relation since z 2. *Monthly Notices of the Royal Astronomical Society*, 434(1):423–436, July 2013.

[79] Mariska Kriek, Alice E. Shapley, Naveen A. Reddy, Brian Siana, Alison L. Coil, Bahram Mobasher, William R. Freeman, Laura de Groot, Sedona H. Price, Ryan Sanders, Irene Shivaei, Gabriel B. Brammer, Ivelina G. Momcheva, Rosalind E. Skelton, Pieter G. van Dokkum, Katherine E. Whitaker, James Aird, Mojegan Azadi, Marc Kassis, James S. Bullock, Charlie Conroy, Romeel Davé, Dušan Kereš, and Mark Krumholz. The MOSFIRE Deep Evolution Field (MOSDEF) Survey: Rest-frame Optical Spectroscopy for \raisebox-0.5ex\textasciitilde1500 H-selected Galaxies at $1.37 < z < 3.8$. *apjs*, 218(2):15, June 2015. _eprint: 1412.1835.

[80] R. B. Larson, B. M. Tinsley, and C. N. Caldwell. The evolution of disk galaxies and the origin of S0 galaxies. *The Astrophysical Journal*, 237:692–707, May 1980. ADS Bibcode: 1980ApJ...237..692L.

[81] Janice C. Lee, Armando Gil de Paz, Christy Tremonti, Robert C. Kennicutt, Jr., Samir Salim, Matthew Bothwell, Daniela Calzetti, Julianne Dalcanton, Daniel Dale, Chad Engelbracht, S. J. José G. Funes, Benjamin Johnson, Shoko Sakai, Evan Skillman, Liese van Zee, Fabian Walter, and Daniel Weisz. Comparison of H and UV Star Formation Rates in the Local Volume: Systematic Discrepancies for Dwarf Galaxies. *The Astrophysical Journal*, 706:599–613, November 2009. ADS Bibcode: 2009ApJ...706..599L.

[82] Simon J. Lilly, C. Marcella Carollo, Antonio Pipino, Alvio Renzini, and Yingjie Peng. Gas Regulation of Galaxies: The Evolution of the Cosmic Specific Star Formation Rate, the Metallicity-Mass-Star-formation Rate Relation, and the Stellar Content of Halos. *apj*, 772(2):119, August 2013. _eprint: 1303.5059.

[83] Oliver J. Lodge. Gravitation and Light. *Nature*, 104:354, December 1919. ADS Bibcode: 1919Natur.104..354L.

[84] E. K. Lofthouse, R. C. W. Houghton, and S. Kaviraj. Local analogues of high-redshift star-forming galaxies: integral field spectroscopy of green peas. *Monthly Notices of the Royal Astronomical Society*, 471:2311–2320, October 2017. ADS Bibcode: 2017MNRAS.471.2311L.

[85] Tobias J. Looser, Francesco D'Eugenio, Joanna M. Piotrowska, Francesco Belfiore, Roberto Maiolino, Michele Cappellari, William M. Baker, and Sandro Tacchella. The stellar fundamental metallicity relation: the correlation between stellar mass, star formation rate, and stellar metallicity. *Monthly Notices of the Royal Astronomical Society*, 532:2832–2841, August 2024. ADS Bibcode: 2024MNRAS.532.2832L.

[86] Marcel Lotz, Rhea-Silvia Remus, Klaus Dolag, Andrea Biviano, and Andreas Burkert. Gone after one orbit: How cluster environments quench galaxies. *Monthly Notices of the Royal Astronomical Society*, 488(4):5370–5389, October 2019.

[87] Piero Madau and Mark Dickinson. Cosmic Star Formation History. *Annual Review of Astronomy and Astrophysics*, 52(1):415–486, August 2014. arXiv:1403.0007 [astro-ph.CO].

[88] Piero Madau, Lucia Pozzetti, and Mark Dickinson. The Star Formation History of Field Galaxies. *The Astrophysical Journal*, 498:106–116, May 1998. ADS Bibcode: 1998ApJ...498..106M.

[89] C. Maier, M. Hayashi, B. L. Ziegler, and T. Kodama. Cluster induced quenching of galaxies in the massive cluster XMMXCS J2215.9-1738 at z \ensuremath\sim 1.5 traced by enhanced metallicities inside half R_{200}. *åp*, 626:A14, June 2019. _eprint: 1903.09591.

[90] C. Maier, U. Kuchner, B. L. Ziegler, M. Verdugo, I. Balestra, M. Girardi, A. Mercurio, P. Rosati, A. Fritz, C. Grillo, M. Nonino, and B. Sartoris. CLASH-VLT: Strangulation of cluster galaxies in MACS J0416.1-2403 as seen from their chemical enrichment. *Astronomy & Astrophysics*, 590:A108, June 2016.

[91] R. Maiolino and F. Mannucci. De re metallica: the cosmic chemical evolution of galaxies. *Astronomy and Astrophysics Review*, 27:3, February 2019. ADS Bibcode: 2019A&ARv..27....3M.

[92] F. Mannucci, G. Cresci, R. Maiolino, A. Marconi, and A. Gnerucci. A fundamental relation between mass, star formation rate and metallicity in local and high-redshift galaxies: The fundamental metallicity relation. *Monthly Notices of the Royal Astronomical Society*, 408(4):2115–2127, September 2010.

[93] A. Marcolini, F. Brighenti, and A. D'Ercole. Three-dimensional simulations of the interstellar medium in dwarf galaxies – I. Ram pressure stripping. *Monthly Notices of the Royal Astronomical Society*, 345(4):1329–1339, November 2003.

[94] Jasleen Matharu, Adam Muzzin, Gabriel B. Brammer, Erica J. Nelson, Matthew W. Auger, Paul C. Hewett, Remco van der Burg, Michael Balogh, Ricardo Demarco, Danilo Marchesini, Allison G. Noble, Gregory Rudnick, Arjen van der Wel, Gillian Wilson, and Howard K. C. Yee. HST/WFC3 Grism Observations of z 1 Clusters: Evidence for Rapid Outside-in Environmental Quenching from Spatially Resolved H\ensuremath\alpha Maps. *apj*, 923(2):222, December 2021. _eprint: 2109.06186.

[95] Stacy S. McGaugh. H II Region Abundances: Model Oxygen Line Ratios. *The Astrophysical Journal*, 380:140, October 1991. ADS Bibcode: 1991ApJ...380..140M.

[96] Sean McGee, Richard Bower, and Michael Balogh. Overconsumption, outflows and the quenching of satellite galaxies. *Monthly Notices of the Royal Astronomical Society: Letters*, 442, April 2014.

[97] Karen McNab, Michael L. Balogh, Remco F. J. van der Burg, Anya Forestell, Kristi Webb, Benedetta Vulcani, Gregory Rudnick, Adam Muzzin, M. C. Cooper, Sean McGee, Andrea Biviano, Pierluigi Cerulo, Jeffrey C. C. Chan, Gabriella De Lucia, Ricardo Demarco, Alexis Finoguenov, Ben Forrest, Caelan Golledge, Pascale Jablonka, Chris Lidman, Julie Nantais, Lyndsay Old, Irene Pintos-Castro, Bianca Poggianti, Andrew M. M. Reeves, Gillian Wilson, Howard K. C. Yee, and Dennis Zaritsky. The GOGREEN survey: transition galaxies and the evolution of environmental quenching. *mnras*, 508(1):157–174, November 2021. _eprint: 2109.03105.

[98] M. Mignoli, A. Cimatti, G. Zamorani, L. Pozzetti, E. Daddi, A. Renzini, T. Broadhurst, S. Cristiani, S. D'Odorico, A. Fontana, E. Giallongo, R. Gilmozzi, N. Menci, and P. Saracco. The K20 survey. VII. The spectroscopic catalogue: spectral properties and evolution of the galaxy population. *Astronomy & Astrophysics*, 437(3):883–897, July 2005. arXiv:astro-ph/0504248.

[99] Š Mikolaitis, P. de Laverny, A. Recio-Blanco, V. Hill, C. C. Worley, and M. de Pascale. The AMBRE project: Iron-peak elements in the solar neighbourhood, December 2016.

[100] Houjun Mo, Frank van den Bosch, and Simon White. *Galaxy Formation and Evolution*. Cambridge University Press, 2010.

[101] Masao Mori and Andreas Burkert. Gas Stripping of Dwarf Galaxies in Clusters ofGalaxies. *The Astrophysical Journal*, 538(2):559, August 2000.

[102] John Moustakas, Jr Robert C. Kennicutt, and Christy A. Tremonti. Optical Star Formation Rate Indicators. *The Astrophysical Journal*, 642(2):775, May 2006.

[103] John S. Mulchaey. X-Ray Properties of Groups of Galaxies. *Annual Review of Astronomy and Astrophysics*, 38(Volume 38, 2000):289–335, September 2000.

[104] Adam Muzzin, Danilo Marchesini, Mauro Stefanon, Marijn Franx, Henry J. McCracken, Bo Milvang-Jensen, James S. Dunlop, J. P. U. Fynbo, Gabriel Brammer, Ivo Labbé, and Pieter G. van Dokkum. THE EVOLUTION OF THE

SLAR MASS FUNCTIONS OF STAR-FORMING AND QUIESCENT GALAXIES TOz= 4 FROM THE COSMOS/UltraVISTA SURVEY. *The Astrophysical Journal*, 777(1):18, October 2013.

[105] Adam Muzzin, Pieter van Dokkum, Mariska Kriek, Ivo Labbé, Iara Cury, Danilo Marchesini, and Marijn Franx. WELL-SAMPLED FAR-INFRARED SPECTRAL ENERGY DISTRIBUTIONS OF z 2 GALAXIES: EVIDENCE FOR SCALED UP COOL GALAXIES. *The Astrophysical Journal*, 725(1):742, November 2010.

[106] Adam Muzzin, Gillian Wilson, H. K. C. Yee, David Gilbank, Henk Hoekstra, Ricardo Demarco, Michael Balogh, Pieter van Dokkum, Marijn Franx, Erica Ellingson, Amalia Hicks, Julie Nantais, Allison Noble, Mark Lacy, Chris Lidman, Alessandro Rettura, Jason Surace, and Tracy Webb. THE GEMINI CLUSTER ASTROPHYSICS SPECTROSCOPIC SURVEY (GCLASS): THE ROLE OF ENVIRONMENT AND SELF-REGULATION IN GALAXY EVOLUTION AT z 1*. *The Astrophysical Journal*, 746(2):188, February 2012.

[107] Themiya Nanayakkara, Karl Glazebrook, Glenn G. Kacprzak, Tiantian Yuan, Kim-Vy Tran, Lee Spitler, Lisa Kewley, Caroline Straatman, Michael Cowley, David Fisher, Ivo Labbe, Adam Tomczak, Rebecca Allen, and Leo Alcorn. ZFIRE: A KECK/MOSFIRE Spectroscopic Survey of Galaxies in Rich Environments at z \ensuremath\sim 2. *apj*, 828(1):21, September 2016. _eprint: 1607.00013.

[108] Julie Nantais, Gillian Wilson, Adam Muzzin, Lyndsay J Old, Ricardo Demarco, Pierluigi Cerulo, Michael Balogh, Gregory Rudnick, Jeffrey Chan, M C Cooper, Ben Forrest, Brian Hayden, Chris Lidman, Allison Noble, Saul Perlmutter, Carter Rhea, Jason Surace, Remco van der Burg, and Eelco van Kampen. The H star formation main sequence in cluster and field galaxies at z 1.6. *Monthly Notices of the Royal Astronomical Society*, 499(3):3061–3070, September 2020.

[109] K. G. Noeske, B. J. Weiner, S. M. Faber, C. Papovich, D. C. Koo, R. S. Somerville, K. Bundy, C. J. Conselice, J. A. Newman, D. Schiminovich, E. Le Floc'h, A. L. Coil, G. H. Rieke, J. M. Lotz, J. R. Primack, P. Barmby, M. C. Cooper, M. Davis, R. S. Ellis, G. G. Fazio, P. Guhathakurta, J. Huang, S. A. Kassin, D. C. Martin, A. C. Phillips, R. M. Rich, T. A. Small, C. N. A. Willmer, and G. Wilson. Star Formation in AEGIS Field Galaxies since $z = 1.1$: The Dominance of Gradually Declining Star Formation, and the Main Sequence of Star-forming Galaxies. *The Astrophysical Journal*, 660(1):L43–L46, April 2007.

[110] J. B. Oke and J. E. Gunn. Secondary standard stars for absolute spectrophotometry. *The Astrophysical Journal*, 266:713–717, March 1983. ADS Bibcode: 1983ApJ...266..713O.

[111] Lyndsay J. Old, Michael L. Balogh, Remco F. J. van der Burg, Andrea Biviano, Howard K. C. Yee, Irene Pintos-Castro, Kristi Webb, Adam Muzzin, Gregory Rudnick, Benedetta Vulcani, Bianca Poggianti, Michael Cooper, Dennis Zaritsky, Pierluigi Cerulo, Gillian Wilson, Jeffrey C. C. Chan, Chris Lidman, Sean McGee, Ricardo Demarco, Ben Forrest, Gabriella De Lucia, David Gilbank, Egidijus Kukstas, Ian G. McCarthy, Pascale Jablonka, Julie Nantais, Allison Noble, Andrew M. M. Reeves, and Heath Shipley. The GOGREEN survey: the environmental dependence of the star-forming galaxy main sequence at $1.0 < z < 1.5$. *mnras*, 493(4):5987–6000, April 2020. _eprint: 2002.11735.

[112] Yossi Oren, Viraj Pandya, Rachel S. Somerville, Shy Genel, Osase Omoruyi, and Amiel Sternberg. The Cosmic Baryon Cycle in IllustrisTNG: Flows of Mass, Energy, and Metals. *The Astrophysical Journal*, 999(2):259, March 2026.

[113] Donald E. Osterbrock and Gary J. Ferland. *Astrophysics of gaseous nebulae and active galactic nuclei*. January 2006. Publication Title: Astrophysics of gaseous nebulae and active galactic nuclei ADS Bibcode: 2006agna.book.....O.

[114] B. E. J. Pagel, M. G. Edmunds, D. E. Blackwell, M. S. Chun, and G. Smith. On the composition of H II regions in southern galaxies - I. NGC 300 and 1365. *Monthly Notices of the Royal Astronomical Society*, 189:95–113, October 1979. ADS Bibcode: 1979MNRAS.189...95P.

[115] Shannon G. Patel, Bradford P. Holden, Daniel D. Kelson, Garth D. Illingworth, and Marijn Franx. THE DEPENDENCE OF STAR FORMATION RATES ON SLAR MASS AND ENVIRONMENT AT z 0.8*, †, ‡, §. *The Astrophysical Journal*, 705(1):L67, October 2009.

[116] Y. Peng, R. Maiolino, and R. Cochrane. Strangulation as the primary mechanism for shutting down star formation in galaxies. *Nature*, 521(7551):192–195, May 2015.

[117] Bradley M. Peterson. *An Introduction to Active Galactic Nuclei*. Cambridge University Press, February 1997. Google-Books-ID: ok4EFlPMStwC.

[118] Max Pettini and Bernard E. J. Pagel. [O iii]/[N ii] as an abundance indicator at high redshift. *Monthly Notices of the Royal Astronomical Society*, 348(3):L59–L63, 2004. _eprint: https://onlinelibrary.wiley.com/doi/pdf/10.1111/j.1365-2966.2004.07591.x.

[119] Joanna M Piotrowska, Asa F L Bluck, Roberto Maiolino, and Yingjie Peng. On the quenching of star formation in observed and simulated central galaxies: evidence for the role of integrated AGN feedback. *Monthly Notices of the Royal Astronomical Society*, 512(1):1052–1090, December 2021. _eprint: https://academic.oup.com/mnras/article-pdf/512/1/1052/42960834/stab3673.pdf.

[120] Planck Collaboration, P. A. R. Ade, N. Aghanim, M. Arnaud, M. Ashdown, J. Aumont, C. Baccigalupi, A. J. Banday, R. B. Barreiro, J. G. Bartlett, N. Bartolo, E. Battaner, R. Battye, K. Benabed, A. Benoît, A. Benoit-Lévy, J.-P. Bernard, M. Bersanelli, P. Bielewicz, J. J. Bock, A. Bonaldi, L. Bonavera, J. R. Bond, J. Borrill, F. R. Bouchet, F. Boulanger, M. Bucher, C. Burigana, R. C. Butler, E. Calabrese, J.-F. Cardoso, A. Catalano, A. Challinor, A. Chamballu, R.-R. Chary, H. C. Chiang, J. Chluba, P. R. Christensen, S. Church, D. L. Clements, S. Colombi, L. P. L. Colombo, C. Combet, A. Coulais, B. P. Crill, A. Curto, F. Cuttaia, L. Danese, R. D. Davies, R. J. Davis, P. de Bernardis, A. de Rosa, G. de Zotti, J. Delabrouille, F.-X. Désert, E. Di Valentino, C. Dickinson, J. M. Diego, K. Dolag, H. Dole, S. Donzelli, O. Doré, M. Douspis, A. Ducout, J. Dunkley, X. Dupac, G. Efstathiou, F. Elsner, T. A. Enßlin, H. K. Eriksen, M. Farhang, J. Fergusson, F. Finelli, O. Forni, M. Frailis, A. A. Fraisse, E. Franceschi, A. Frejsel, S. Galeotta, S. Galli, K. Ganga, C. Gauthier, M. Gerbino, T. Ghosh, M. Giard, Y. Giraud-Héraud, E. Giusarma, E. Gjerløw, J. González-Nuevo, K. M. Górski, S. Gratton, A. Gregorio, A. Gruppuso, J. E. Gudmundsson, J. Hamann, F. K. Hansen, D. Hanson, D. L. Harrison, G. Helou, S. Henrot-Versillé, C. Hernández-Monteagudo, D. Herranz, S. R. Hildebrandt, E. Hivon, M. Hobson, W. A. Holmes, A. Hornstrup, W. Hovest, Z. Huang, K. M. Huffenberger, G. Hurier, A. H. Jaffe, T. R. Jaffe, W. C. Jones, M. Juvela, E. Keihänen, R. Keskitalo, T. S. Kisner, R. Kneissl, J. Knoche, L. Knox, M. Kunz, H. Kurki-Suonio, G. Lagache, A. Lähteenmäki, J.-M. Lamarre, A. Lasenby, M. Lattanzi, C. R. Lawrence, J. P. Leahy, R. Leonardi, J. Lesgourgues, F. Levrier, A. Lewis, M. Liguori, P. B. Lilje, M. Linden-Vørnle, M. López-Caniego, P. M. Lubin, J. F. Macías-Pérez, G. Maggio, D. Maino, N. Mandolesi, A. Mangilli, A. Marchini, M. Maris, P. G. Martin, M. Martinelli, E. Martínez-González, S. Masi, S. Matarrese, P. McGehee, P. R. Meinhold, A. Melchiorri, J.-B. Melin, L. Mendes, A. Mennella, M. Migliaccio, M. Millea, S. Mitra, M.-A. Miville-Deschênes, A. Moneti, L. Montier, G. Morgante, D. Mortlock, A. Moss, D. Munshi, J. A. Murphy, P. Naselsky, F. Nati, P. Natoli, C. B. Netterfield, H. U. Nørgaard-Nielsen, F. Noviello, D. Novikov, I. Novikov, C. A. Oxborrow, F. Paci, L. Pagano, F. Pajot, R. Paladini, D. Paoletti, B. Partridge, F. Pasian, G. Patanchon, T. J. Pearson, O. Perdereau, L. Perotto, F. Perrotta, V. Pettorino, F. Piacentini, M. Piat, E. Pierpaoli, D. Pietrobon,

S. Plaszczynski, E. Pointecouteau, G. Polenta, L. Popa, G. W. Pratt, and G. Prézeau. Planck 2015 results. XIII. Cosmological parameters. *åp*, 594:A13, September 2016. _eprint: 1502.01589.

[121] P Popesso, A Concas, G Cresci, S Belli, G Rodighiero, H Inami, M Dickinson, O Ilbert, M Pannella, and D Elbaz. The main sequence of star-forming galaxies across cosmic times. *Monthly Notices of the Royal Astronomical Society*, 519(1):1526–1544, November 2022.

[122] J. Xavier Prochaska, Joseph F. Hennawi, Kyle B. Westfall, Ryan J. Cooke, Feige Wang, Tiffany Hsyu, Frederick B. Davies, and Emanuele Paolo Farina. PypeIt: The Python Spectroscopic Data Reduction Pipeline. *Journal of Open Source Software*, 5(56):2308, 2020.

[123] Westfall Cooke Wang Hsyu Davies Farina Pelliccia J. Xavier Joseph Kyle Ryan Feige Tiffany Fred Emanuele Debora Prochaska, Hennawi. PypeIt, October 2025.

[124] Naveen A. Reddy, Mariska Kriek, Alice E. Shapley, William R. Freeman, Brian Siana, Alison L. Coil, Bahram Mobasher, Sedona H. Price, Ryan L. Sanders, and Irene Shivaei. The MOSDEF Survey: Measurements of Balmer Decrements and the Dust Attenuation Curve at Redshifts z \raisebox-0.5ex\textasciitilde 1.4-2.6. *apj*, 806(2):259, June 2015. _eprint: 1504.02782.

[125] Alvio Renzini and Ying-jie Peng. An Objective Definition for the Main Sequence of Star-forming Galaxies. *apjl*, 801(2):L29, March 2015. _eprint: 1502.01027.

[126] Ian D. Roberts, Maojin Lang, Daria Trotsenko, Ashley R. Bemis, Sara L. Ellison, Lihwai Lin, Hsi-An Pan, Alessandro Ignesti, Sarah Leslie, and Reinout J. van Weeren. LoTSS Jellyfish Galaxies. IV. Enhanced Star Formation on the Leading Half of Cluster Galaxies and Gas Compression in IC3949. *The Astrophysical Journal*, 941:77, December 2022. ADS Bibcode: 2022ApJ...941...77R.

[127] Ian D. Roberts and Laura C. Parker. Ram pressure stripping candidates in the coma cluster: evidence for enhanced star formation. *Monthly Notices of the Royal Astronomical Society*, 495:554–569, June 2020. ADS Bibcode: 2020MNRAS.495..554R.

[128] Morton S. Roberts. Integral Properties of Spiral and Irregular Galaxies. *The Astronomical Journal*, 74:859–876, September 1969. ADS Bibcode: 1969AJ.....74..859R.

[129] Elke Roediger and Marcus Brüggen. Ram pressure stripping of disc galaxies orbiting in clusters – I. Mass and radius of the remaining gas disc. *Monthly Notices of the Royal Astronomical Society*, 380(4):1399–1408, September 2007.

[130] Tobias A Russell, Neva Dobric, Nathan J Adams, Christopher J Conselice, Duncan Austin, Thomas Harvey, James A A Trussler, Leonardo Ferreira, Lewi Westcott, Honor Harris, Rogier A Windhorst, Dan Coe, Seth H Cohen, Simon P Driver, Brenda Frye, Norman A Grogin, Nimish P Hathi, Rolf A Jansen, Anton M Koekemoer, Madeline A Marshall, Rafael Ortiz III, Nor Pirzkal, Aaron Robotham, Russell E Ryan, Jake Summers, Jordan C J D'Silva, Christopher N A Willmer, and Haojing Yan. Cosmic stillness: high quiescent galaxy fractions across upper mass scales in the early Universe to $z = 7$ with *JWST*. *Monthly Notices of the Royal Astronomical Society*, 544(4):4482–4504, November 2025.

[131] Ryan L. Sanders, Alice E. Shapley, Mariska Kriek, William R. Freeman, Naveen A. Reddy, Brian Siana, Alison L. Coil, Bahram Mobasher, Romeel Davé, Irene Shivaei, Mojegan Azadi, Sedona H. Price, Gene Leung, Tara Fetherolf, Laura de Groot, Tom Zick, Francesca M. Fornasini, and Guillermo Barro. The MOSDEF Survey: A Stellar Mass-SFR-Metallicity Relation Exists at z 2.3. *The Astrophysical Journal*, 858:99, May 2018. ADS Bibcode: 2018ApJ...858...99S.

[132] Ryan L. Sanders, Alice E. Shapley, Michael W. Topping, Naveen A. Reddy, and Gabriel B. Brammer. Direct T e-based Metallicities of z = 29 Galaxies with JWST/NIRSpec: Empirical Metallicity Calibrations Applicable from Reionization to Cosmic Noon. *The Astrophysical Journal*, 962:24, February 2024. ADS Bibcode: 2024ApJ...962...24S.

[133] Paola Santini, Adriano Fontana, Marco Castellano, Marcella Di Criscienzo, Emiliano Merlin, Ricardo Amorin, Fergus Cullen, Emanuele Daddi, Mark Dickinson, James S. Dunlop, Andrea Grazian, Alessandra Lamastra, Ross J. McLure, Michał. J. Michałowski, Laura Pentericci, and Xinwen Shu. The Star Formation Main Sequence in the Hubble Space Telescope Frontier Fields. *The Astrophysical Journal*, 847(1):76, September 2017.

[134] Alice E. Shapley, Naveen A. Reddy, Mariska Kriek, William R. Freeman, Ryan L. Sanders, Brian Siana, Alison L. Coil, Bahram Mobasher, Irene Shivaei, Sedona H. Price, and Laura de Groot. The MOSDEF Survey: Excitation Properties of z 2.3 Star-forming Galaxies. *The Astrophysical Journal*, 801:88, March 2015. ADS Bibcode: 2015ApJ...801...88S.

[135] Hiroko Shinnaga, Thomas G. Phillips, Ray S. Furuya, and Yoshimi Kitamura. Warm Extended Dense Gas Lurking At The Heart Of A Cold Collapsing Dense Core. *The Astrophysical Journal*, 706(2):L226–L229, December 2009. arXiv:0910.0463 [astro-ph.GA].

[136] Beverly J. Smith, Peter Wagstaff, Curtis Struck, Roberto Soria, Brianne Dunn, Douglas Swartz, and Mark L. Giroux. The Hot Gas Exhaust of Starburst Engines in Mergers: Testing Models of Stellar Feedback and Star Formation Regulation. *The Astronomical Journal*, 158(4):169, October 2019. arXiv:1908.09402 [astro-ph.GA].

[137] David Sobral, Philip N. Best, Ian Smail, James E. Geach, Michele Cirasuolo, Timothy Garn, and Gavin B. Dalton. The dependence of star formation activity on environment and stellar mass at z 1 from the HiZELS-H survey: Star formation, environment & mass at z1. *Monthly Notices of the Royal Astronomical Society*, 411(1):675–692, October 2010.

[138] David Sobral, Andra Stroe, Yusei Koyama, Behnam Darvish, João Calhau, Ana Afonso, Tadayuki Kodama, and Fumiaki Nakata. The nature of H\ensuremath\alpha star-forming galaxies at z \ensuremath\sim 0.4 in and around Cl 0939+4713: the environment matters. *mnras*, 458(4):3443–3454, June 2016. _eprint: 1603.00462.

[139] Linda S. Sparke and John Sill Gallagher. *Galaxies in the Universe: An Introduction*. Cambridge University Press, August 2000. Google-Books-ID: tzNF79roUfoC.

[140] Joshua S. Speagle, Charles L. Steinhardt, Peter L. Capak, and John D. Silverman. A Highly Consistent Framework for the Evolution of the Star-Forming "Main Sequence" from z˜0-6. *The Astrophysical Journal Supplement Series*, 214(2):15, September 2014. arXiv:1405.2041 [astro-ph.GA].

[141] Elizabeth Taylor, Omar Almaini, Michael Merrifield, David Maltby, Vivienne Wild, William G Hartley, and Kate Rowlands. The role of mass and environment in the build-up of the quenched galaxy population since cosmic noon. *Monthly Notices of the Royal Astronomical Society*, 522(2):2297–2306, April 2023.

[142] E. Tempel, E. Tago, and L. J. Liivamägi. Groups and clusters of galaxies in the SDSS DR8. Value-added catalogues. *åp*, 540:A106, April 2012. _eprint: 1112.4648.

[143] Stephanie Tonnesen and Greg L. Bryan. GAS STRIPPING IN SIMULATED GALAXIES WITH A MULTIPHASE INTERSLAR MEDIUM. *The Astrophysical Journal*, 694(2):789, March 2009.

[144] Stephanie Tonnesen, Greg L. Bryan, and J. H. van Gorkom. Environmentally Driven Evolution of Simulated Cluster Galaxies. *The Astrophysical Journal*, 671(2):1434, December 2007.

[145] Christy A. Tremonti, Timothy M. Heckman, Guinevere Kauffmann, Jarle Brinchmann, Stephane Charlot, Simon D. M. White, Mark Seibert, Eric W. Peng, David J. Schlegel, Alan Uomoto, Masataka Fukugita, and Jon Brinkmann. The Origin of the Mass-Metallicity Relation: Insights from 53,000 Star-forming Galaxies in the Sloan Digital Sky Survey. *The Astrophysical Journal*, 613(2):898–913, October 2004.

[146] James Trussler, Roberto Maiolino, Claudia Maraston, Yingjie Peng, Daniel Thomas, Daniel Goddard, and Jianhui Lian. Both starvation and outflows drive galaxy quenching. *Monthly Notices of the Royal Astronomical Society*, 491(4):5406–5434, February 2020.

[147] Freeke van de Voort, Yannick M. Bahé, Richard G. Bower, Camila A. Correa, Robert A. Crain, Joop Schaye, and Tom Theuns. The environmental dependence of gas accretion on to galaxies: quenching satellites through starvation. *Monthly Notices of the Royal Astronomical Society*, 466:3460–3471, April 2017. ADS Bibcode: 2017MNRAS.466.3460V.

[148] Pieter van Dokkum, Gabriel Brammer, Ivelina Momcheva, Rosalind E. Skelton, and Katherine E. Whitaker. 3D-HST Data Release v3.0: Extremely Deep Spectra in the UDF and WFC3 Mosaics in the 3D-HST/CANDELS Fields. *arXiv e-prints*, page arXiv:1305.2140, May 2013. _eprint: 1305.2140.

[149] M. B. Vila-Costas and Michael Edmunds. The nitrogen-to-oxygen ratio in galaxies and its implications for the origin of nitrogen. *Monthly Notices of the Royal Astronomical Society*, 265:199–212, 1993.

[150] R. von Steiger and T. H. Zurbuchen. SOLAR METALLICITY DERIVED FROM IN SITU SOLAR WIND COMPOSITION. *The Astrophysical Journal*, 816(1):13, December 2015.

[151] Benedetta Vulcani, Bianca M. Poggianti, Rose A. Finn, Gregory Rudnick, Vandana Desai, and Steven Bamford. COMPARING THE RELATION BETWEEN STAR FORMATION AND GALAXY MASS IN DIFFERENT ENVIRONMENTS. *The Astrophysical Journal Letters*, 710(1):L1, January 2010.

[152] Risa H. Wechsler and Jeremy L. Tinker. The Connection Between Galaxies and Their Dark Matter Halos. *Annual Review of Astronomy and Astrophysics*, 56(Volume 56, 2018):435–487, September 2018.

[153] Katherine E. Whitaker, Pieter G. van Dokkum, Gabriel Brammer, and Marijn Franx. The Star-formation Mass Sequence out to z=2.5. *The Astrophysical Journal*, 754(2):L29, August 2012. arXiv:1205.0547 [astro-ph.CO].

[154] Katherine E. Whitaker, Marijn Franx, Joel Leja, Pieter G. van Dokkum, Alaina Henry, Rosalind E. Skelton, Mattia Fumagalli, Ivelina G. Momcheva, Gabriel B. Brammer, Ivo Labbé, Erica J. Nelson, and Jane R. Rigby. Constraining the Low-mass Slope of the Star Formation Sequence at $0.5 < z < 2.5$. *apj*, 795(2):104, November 2014. _eprint: 1407.1843.

[155] Martin White. The mass of a halo. *Astronomy & Astrophysics*, 367(1):27–32, February 2001. arXiv:astro-ph/0011495.

[156] E. Wisnioski, N. M. Förster Schreiber, M. Fossati, J. T. Mendel, D. Wilman, R. Genzel, R. Bender, S. Wuyts, R. L. Davies, H. Übler, K. Bandara, A. Beifiori, S. Belli, G. Brammer, J. Chan, R. I. Davies, M. Fabricius, A. Galametz, P. Lang, D. Lutz, E. J. Nelson, I. Momcheva, S. Price, D. Rosario, R. Saglia, S. Seitz, T. Shimizu, L. J. Tacconi, K. Tadaki, P. G. van Dokkum, and E. Wuyts. The KMOS^{3d} Survey: Data Release and Final Survey Paper. *apj*, 886(2):124, December 2019. _eprint: 1909.11096.

[157] Ruby J. Wright, Rachel S. Somerville, Claudia del P. Lagos, Matthieu Schaller, Romeel Davé, Daniel Anglés-Alcázar, and Shy Genel. The baryon cycle in modern cosmological hydrodynamical simulations, February 2024.

[158] Eva Wuyts, Emily Wisnioski, Matteo Fossati, Natascha M. Förster Schreiber, Reinhard Genzel, Ric Davies, J. Trevor Mendel, Thorsten Naab, Bernhard Röttgers, David J. Wilman, Stijn Wuyts, Kaushala Bandara, Alessandra Beifiori, Sirio Belli, Ralf Bender, Gabriel B. Brammer, Andreas Burkert, Jeffrey Chan, Audrey Galametz, Sandesh K. Kulkarni, Philipp Lang, Dieter Lutz, Ivelina G. Momcheva, Erica J. Nelson, David Rosario, Roberto P. Saglia, Stella Seitz, Linda J. Tacconi, Kenichi Tadaki, Hannah Übler, and Pieter van Dokkum. THE EVOLUTION OF METALLICITY AND METALLICITY GRADIENTS FROM z = 2.7 TO 0.6 WITH KMOS^{3d}. *The Astrophysical Journal*, 827(1):74, August 2016.

[159] Gregory R. Zeimann, S. A. Stanford, Mark Brodwin, Anthony H. Gonzalez, Conor Mancone, Gregory F. Snyder, Daniel Stern, Peter Eisenhardt, Arjun Dey, and John Moustakas. H STAR FORMATION RATES OFz> 1 GALAXY CLUSTERS IN THE IRAC SHALLOW CLUSTER SURVEY. *The Astrophysical Journal*, 779(2):137, December 2013.

[160] I. A. Zinchenko and J. M. Vílchez. Different behaviour of the gas-phase and stellar metallicity in the central part of MaNGA galaxies. *Astronomy & Astrophysics*, 690:A13, October 2024.

[161] Ying Zu and Rachel Mandelbaum. Mapping stellar content to dark matter haloes – II. Halo mass is the main driver of galaxy quenching. *Monthly Notices of the Royal Astronomical Society*, 457(4):4360–4383, March 2016. _eprint: https://academic.oup.com/mnras/article-pdf/457/4/4360/18513526/stw221.pdf.

APPENDICES

Appendix A

Additional Plots

A.1 Supplementary Informational Plots

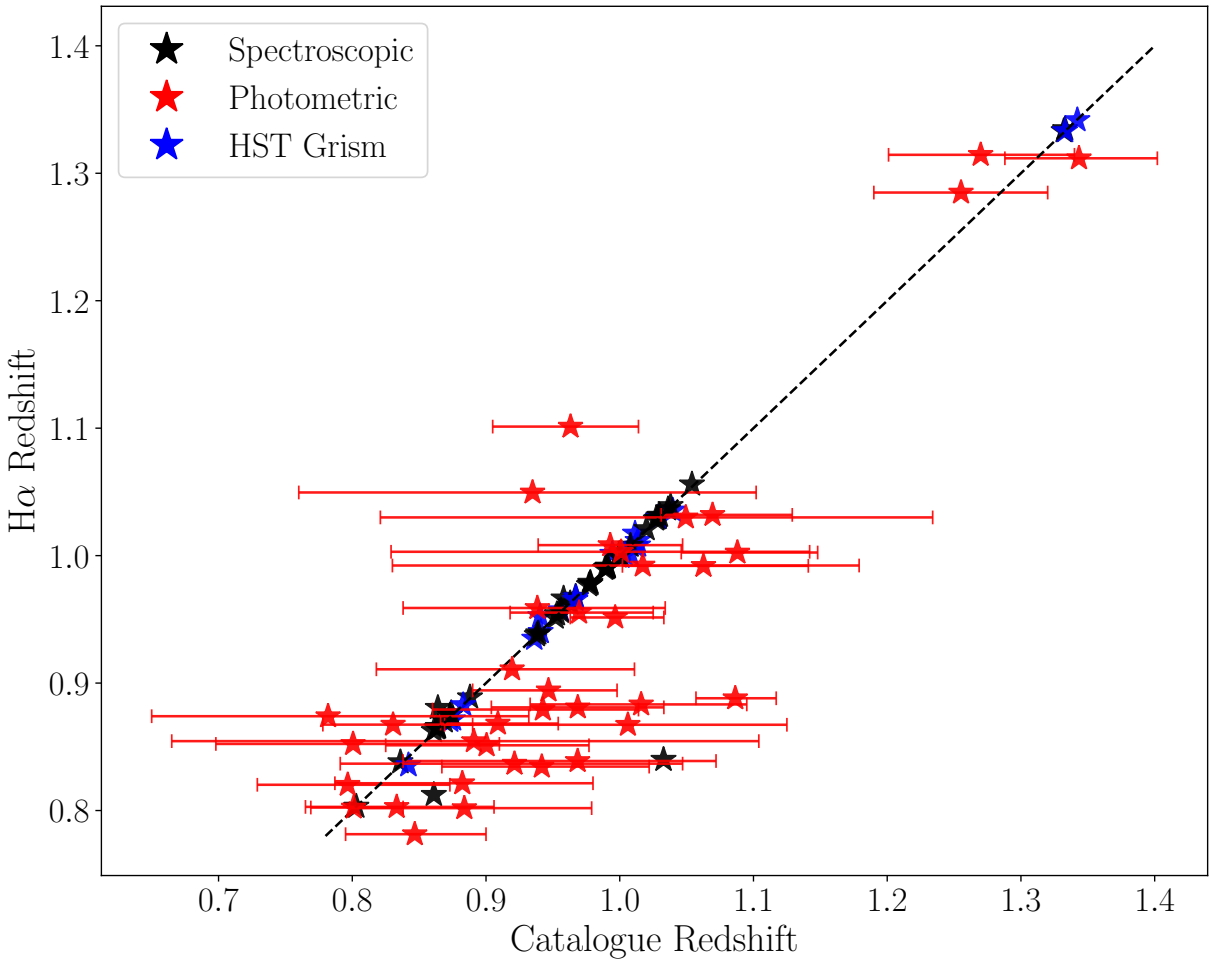


Figure A.1: Redshift parameter fit as a function of the GOGREEN catalogue redshift. Objects in black have spectroscopic redshifts from GOGREEN; blue points have a redshift measured from HST Grism; and red points have only photometric redshifts. The photometric redshifts have relatively large redshift uncertainties and have a scatter about the 1-to-1 line of $\sigma = 0.071$, while the grism and spectroscopic redshifts have a scatter of $\sigma = 0.004$ and $\sigma = 0.008$, respectively (excluding a spectroscopic extreme outlier at $z \sim 1.05$).

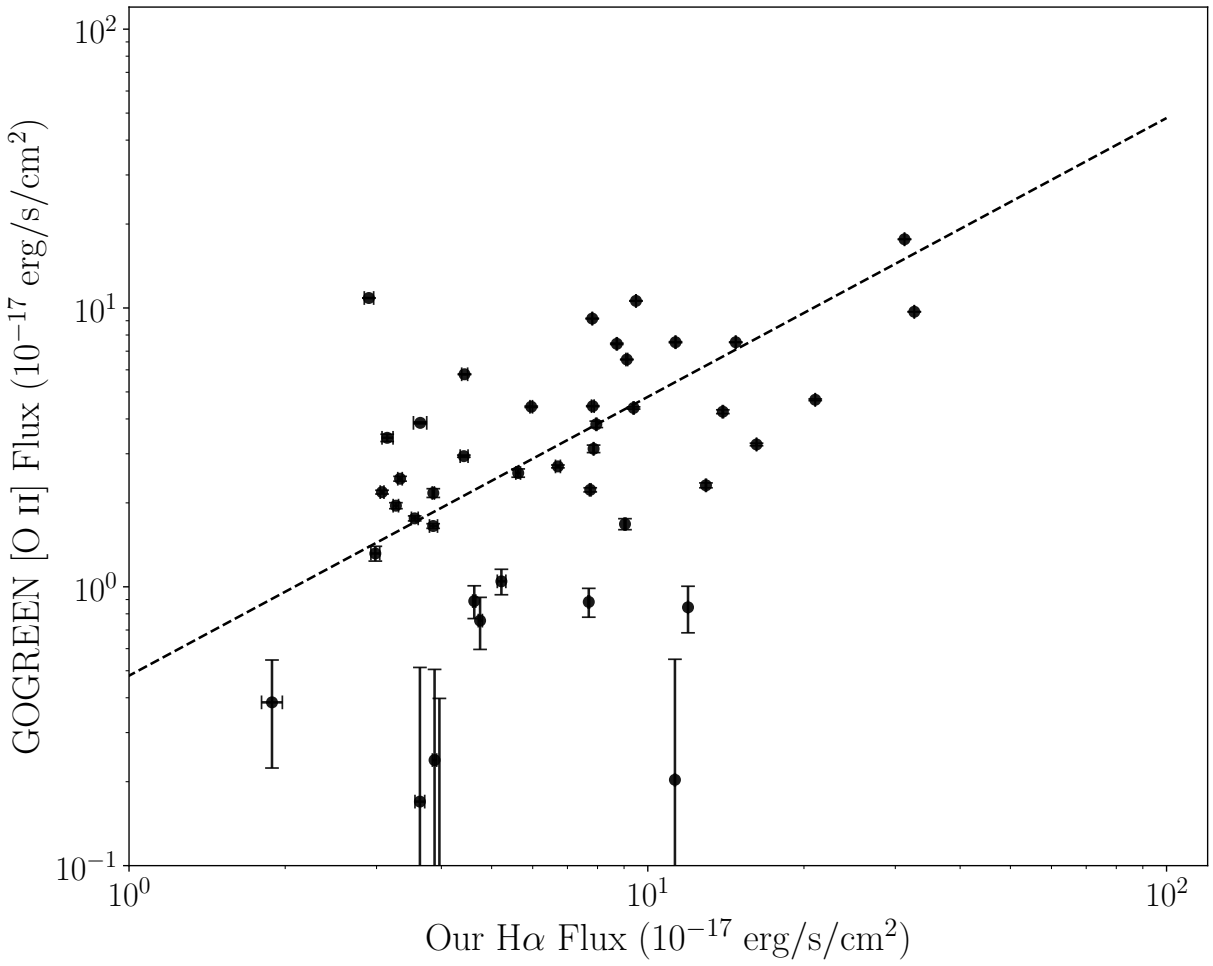


Figure A.2: We show [O II] fluxes from [111] as a function of our measured Hα fluxes. The large scatter is likely dominated by differences in extinction [47]; the [O II] emission line also depends on metallicity. We show a measurement from [47], where they calculated $[O\,\textsc{ii}]/H\alpha = 0.48$, shown as the black dotted line. We compare with [111] in the discussion.

A.2 Cluster Selection

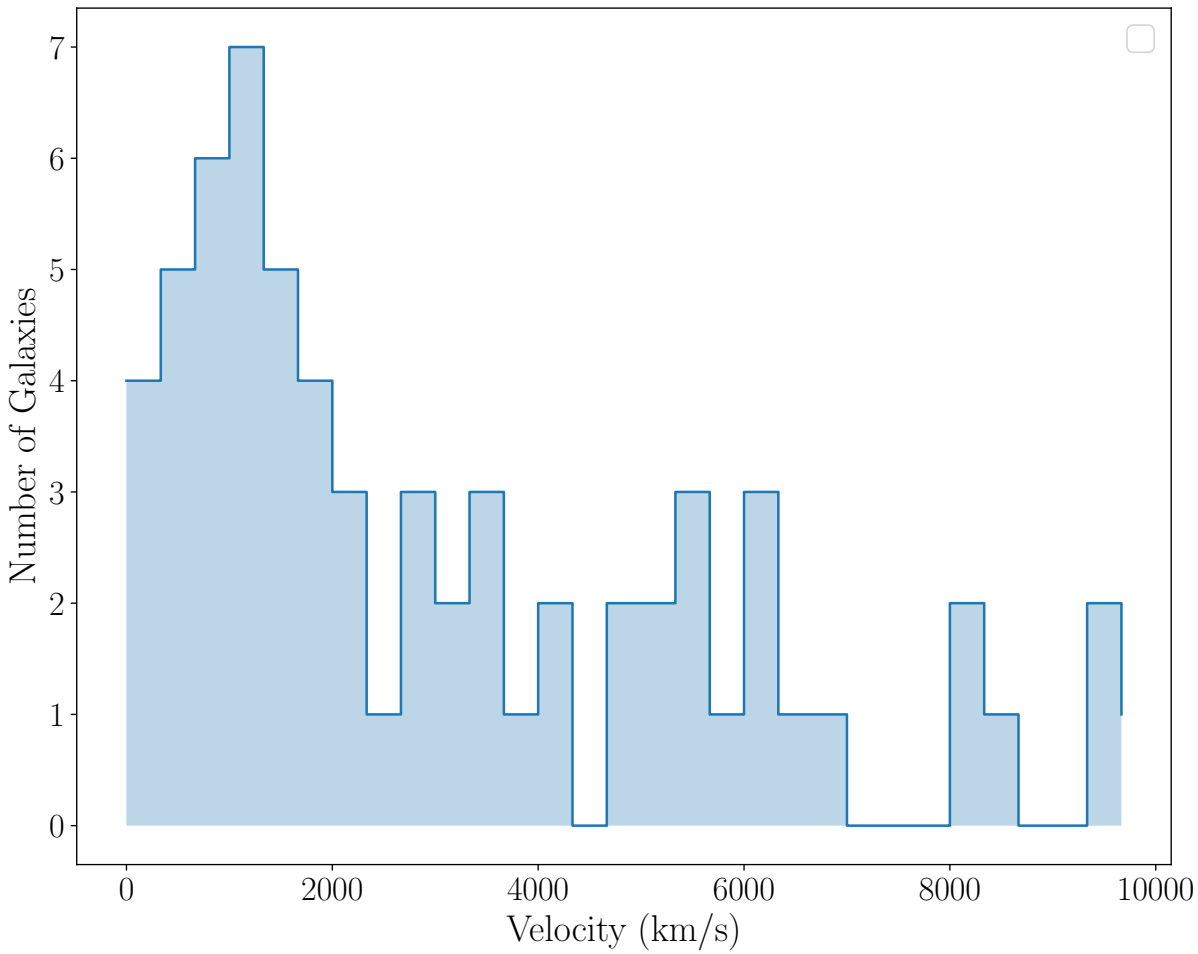


Figure A.3: Histogram of the number of galaxies within various velocity bins. There is a modest population of galaxies with $\Delta V < 2000$ km/s. We infer that using a $\Delta V \leq 3000$ km/s cut is a reasonable estimate for cluster members.

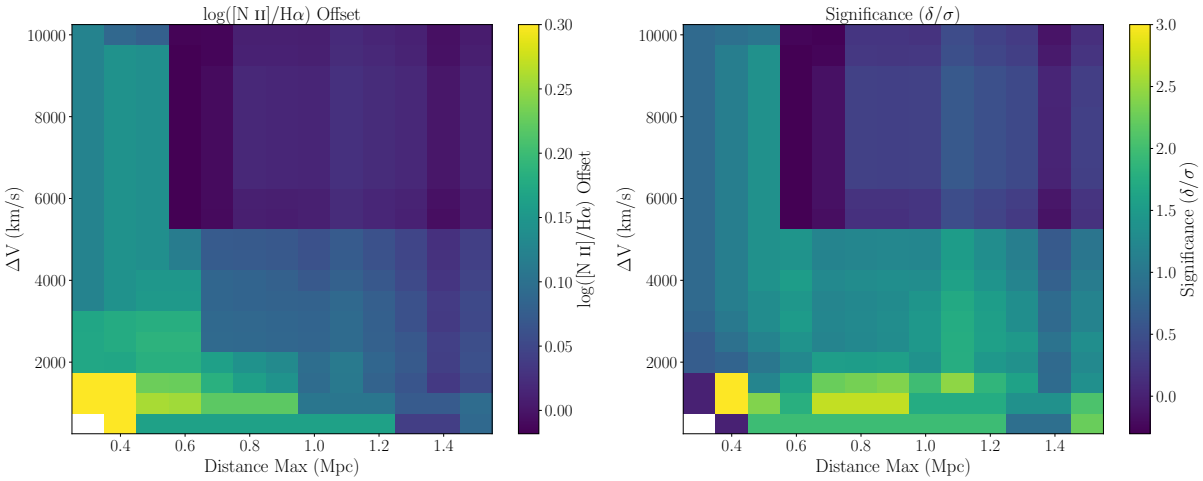


Figure A.4: We examine the magnitude and significance of the offset in log([N II]/Hα) as a function of cut used. We show the magnitude and significance as the colour bar, with each grid square indicating a different cut. For example, for our cuts at x = 1.0 and y = 3000, the magnitude and significance of the offset is larger than if the cuts were at a larger value of x and y.

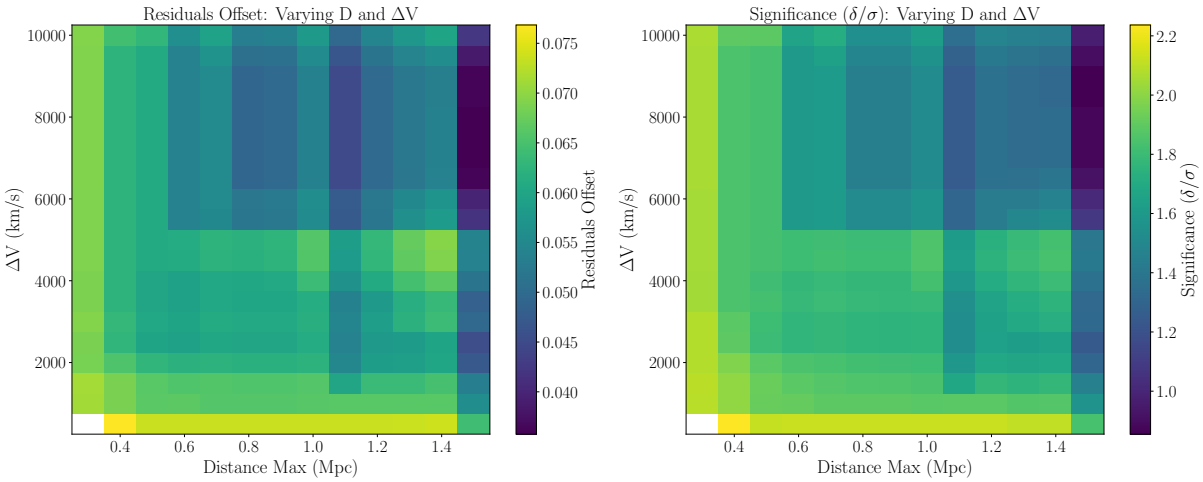


Figure A.5: We examine the magnitude and significance of the offset in the residuals plot (Figure 2.7) as a function of cut used. We use the same colouration method as the previous plot. For both, our cuts at x = 1.0 and y = 3000 show a fairly large significance and offset.

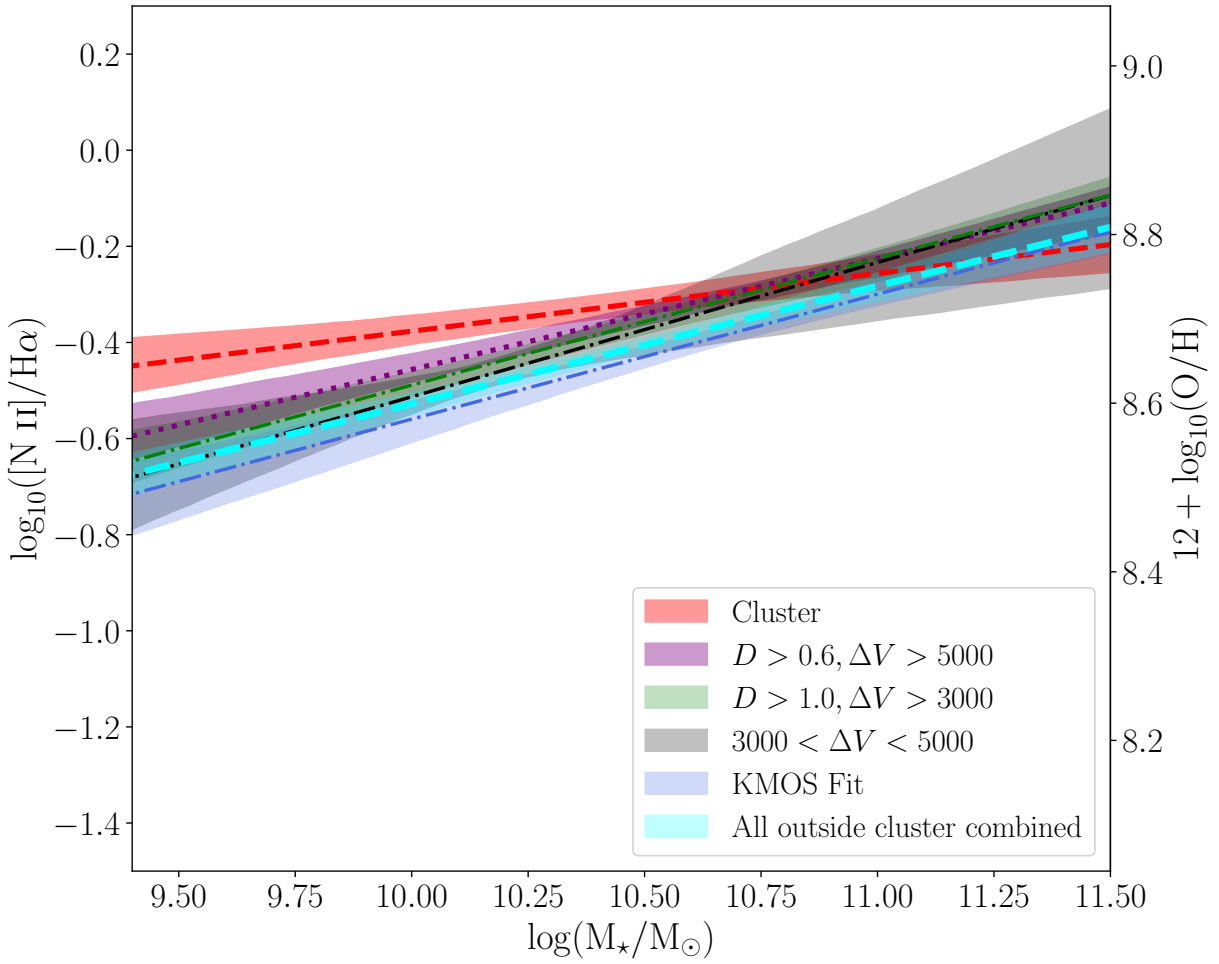


Figure A.6: We show the fit to our $\log([\mathrm{N\,II}]/\mathrm{H}\alpha)$ data for a variety of cuts. In red, we show our cluster with the current cuts. In purple, we show galaxies that we would expect to be part of the field; galaxies that have $D < 0.6$ Mpc *and* $\Delta V > 5000$ km/s. In green we show what we are currently using as the field, so everything not included in the red sample. The black shows transition galaxies, so galaxies that do not fit into the red or the purple. In blue we show the KMOS fit, and the cyan shows the fit we compare our results to. No matter the choice, we always see an offset between models and the error bars all overlap.

A.3 Alternative Plots

In Figure A.7, we consider blended $H\alpha + [N\,\textsc{ii}]$ equivalent width as a function of stellar mass. While our data has sufficient spectral resolution to resolve Hα and [N II] , we plot the sum of the equivalent widths for all three emission lines, Hα and both [N II] lines, in order to compare with the large 3D-HST field samples as well as data from [94]. Our cluster sample is represented by the red stars, and the purple stars represent the field members. The blue points represent HST field sample from [94] and the background gray points are from 3D-HST [148]. We observe a weak trend with stellar mass.

The equivalent width distribution between our sample and the two comparison samples are similar. Our sample selection is heterogeneous, which complicates quantitative analysis. Furthermore, because we prioritized SF galaxies, we are strongly biased against the low equivalent width objects in the [94] and 3D-HST catalogues. Nonetheless, the median and relative scatter of our SF sample is in good qualitative agreement with the field main sequence.

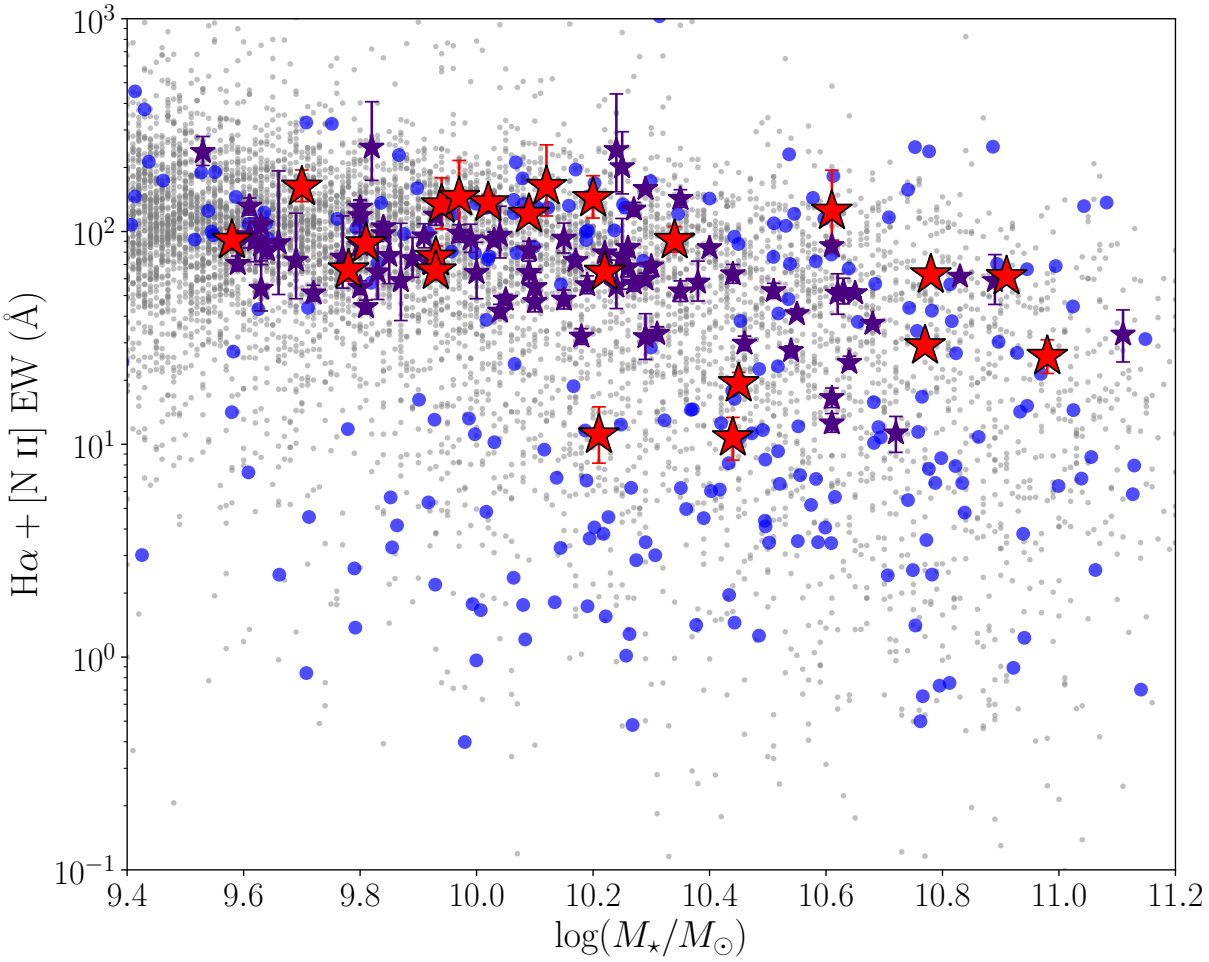


Figure A.7: We show rest frame Hα + [N II] equivalent width as a function of stellar mass. Our cluster sample is shown with the red stars, while our field sample is shown in purple. We compare to the 3D-HST field sample shown as the gray background points, which is limited to the same redshift and mass range as our sample. We also show the data from [94] in blue, where we limit their sample to only cluster galaxies using the velocity dispersion.

We also look at Hα luminosity of field samples compared to our cluster sample as a function of stellar mass. The Hα luminosity will be affected by dust, but we do not perform any corrections for dust to any sample plotted in Figure A.8. MOSDEF points are blue triangles and KMOS is the blue diamonds, while our cluster points are the stars colour coded by redshift and the gray points are our field. The blue and green line are Hα luminosities calculated in [154] which are star formation rates calculated with Hα using 3D-HST data. The two colours correspond to different redshift ranges, with blue and green corresponding to $0.7 < z < 1.1$ and $1.1 < z < 1.5$ respectively. [94] found strong consistency with this dataset, although their SFR were slightly elevated.

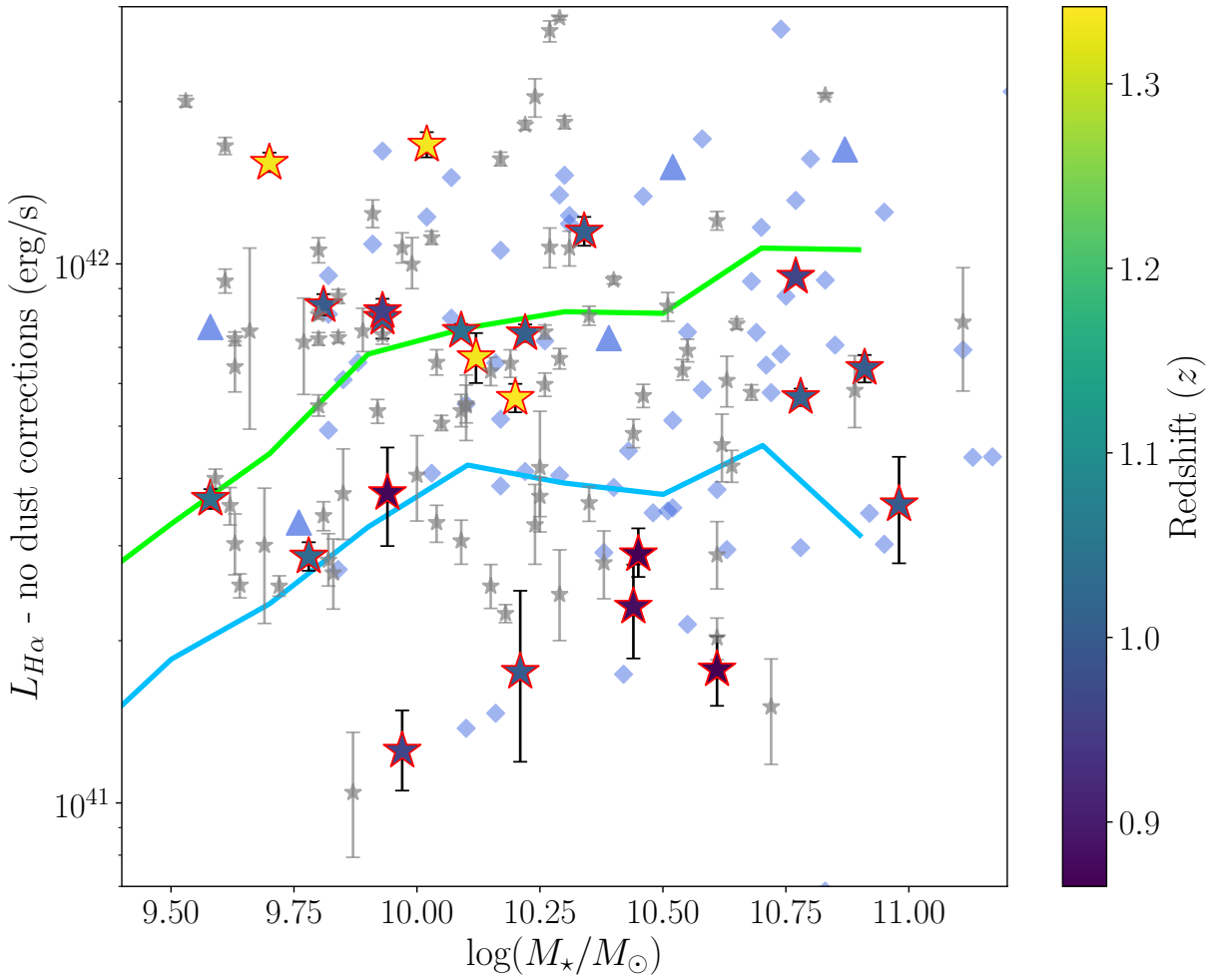


Figure A.8: We show Hα luminosity (uncorrected for dust extinction) as a function of stellar mass for our data, MOSDEF, 3D-HST, and work from [154] - which was calculated using 3D-HST data. The coloured stars with red outlines are our data, with the blue triangles representing the $z < 1.4$ MOSDEF sample. The green and blue lines are the Hα luminosities for two different redshift ranges from [154]. The results were consistent with the conclusions of [94], but [94] had a slight elevation of SFR. We find that our Hα luminosities are consistent with all the field samples. Furthermore, the redshift effect present in the lines from [154] is also present within our sample, with the higher redshift objects on average possessing slightly higher Hα luminosities than the low redshift galaxies.

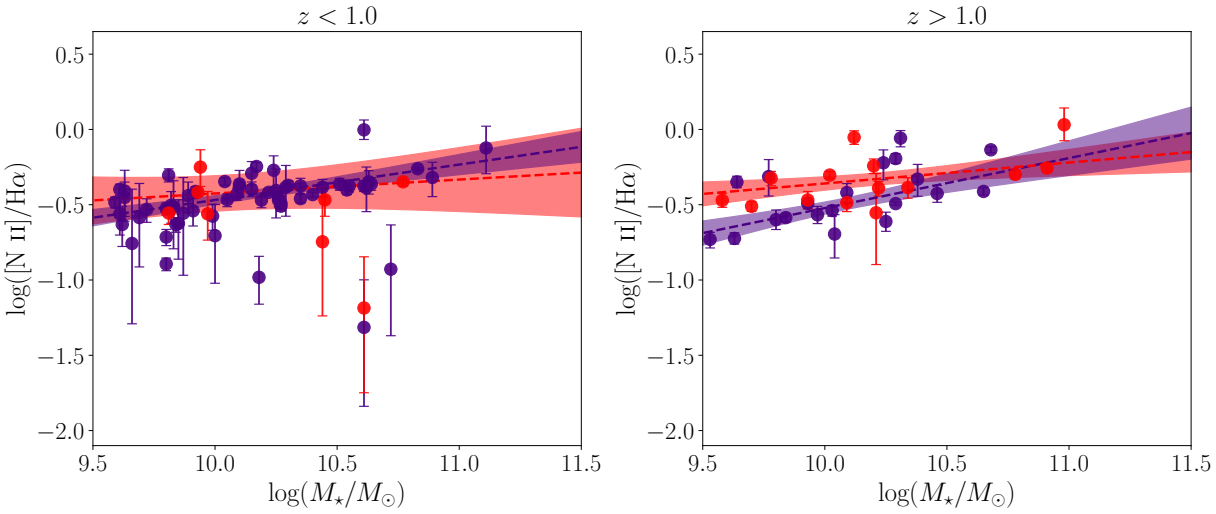


Figure A.9: We show $[N\,\textsc{ii}]/H\alpha$ as a function of stellar mass in two different redshift bins on either side of $z = 1$ and colour-coded by cluster membership. The red points are cluster galaxies while the purple points are field galaxies. We see an offset between $[N\,\textsc{ii}]/H\alpha$ for the field and cluster samples at higher redshifts of 0.13 ± 0.06 measured at $10^{10.2}$ $M_\odot$. We see a similar offset to that of [89].

A.4 Redshift Dependence within our Sample

In Figure A.9, we split our data into two different bins of redshift. On the left hand side, we show galaxies within our sample where $z < 1.0$, and on the right hand side $z > 1.0$. At $z < 1.0$, the offset between the two samples is consistent with zero. However, at $z > 1.0$ the offset between cluster and field is far greater. This offset, measured at $M = 10^{10.2} M_\odot$, is 0.125 ± 0.057 dex. This is comparable with [89] at $z \sim 1.5$. We found previously that our cluster sampled exhibited higher metallicities than the field and from [89] and our work, this could have a significant dependence on redshift.

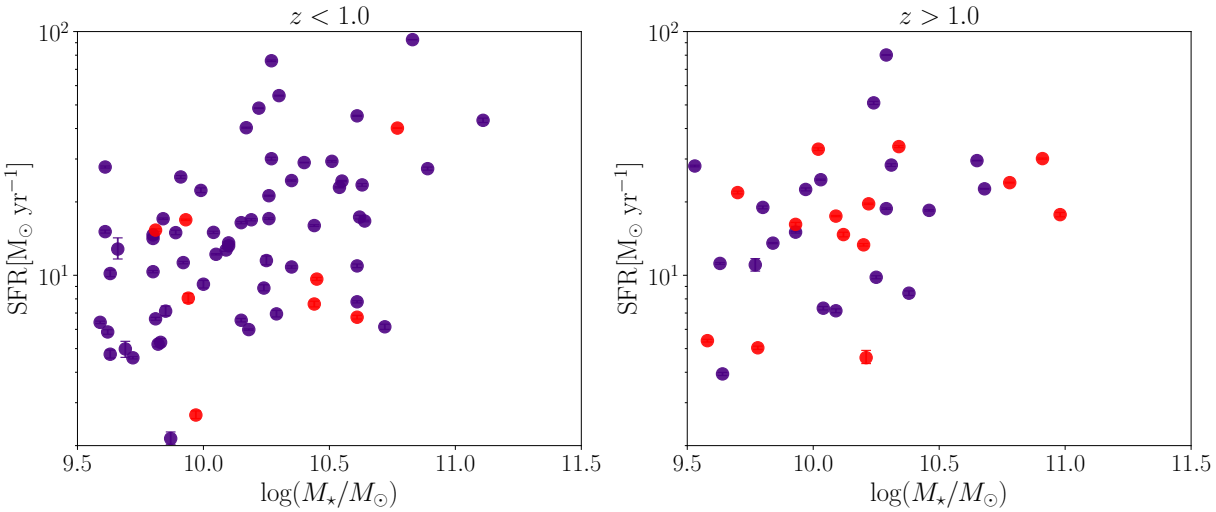


Figure A.10: We show SFR as a function of stellar mass in two different redshift bins on either size of $z = 1$ and colour-coded by cluster membership. The red points are galaxies within the cluster while the purple points in the field. We see no evidence for an offset in SFR width between the cluster and field galaxies in either redshift bin within our sample.

As we see this slight offset in metallicity, we also check for an offset SFR. In Figure A.10, we show our SFR as a function of stellar mass separated at $z = 1$ and split by cluster membership. We see no significant dependence on redshift and environment for SFR within our data.

Appendix B

Aperture Corrections

B.1 Continuum Corrections

In Figure B.1, we show the continuum flux at Hα from our MCMC fits to the spectrum. The fit underestimates the broad band total magnitude from GOGREEN by 80% on average.

We attribute this to two reasons: the narrower aperture used for spectroscopy and the bright flux contribution from Hα in the broadband image. We estimate the stellar continuum flux in the broadband by using the Hα equivalent width measured from our spectroscopy (Section 2.1.4), as

$$f'_{BB} = \frac{f_{BB}}{(1 + EW/\Delta\lambda)}$$

where f'_{BB} the rescaled broadband continuum flux, f_{BB} is the broadband flux, EW is the H$\alpha + [N\,\textsc{ii}]$ equivalent width, and $\Delta\lambda$ is the width of the filter's transmission window. We then calculate an average continuum correction factor, $\bar{\beta}_c = f'_{BB}/f_c = 1.32$. (Figure B.2)

We therefore scale our flux-calibrated spectra by this factor to ensure agreement, on average, with the ground-based magnitudes. We checked against different methods of measuring the continuum, and found good agreement with any method used, one such method shown in Figure B.3.

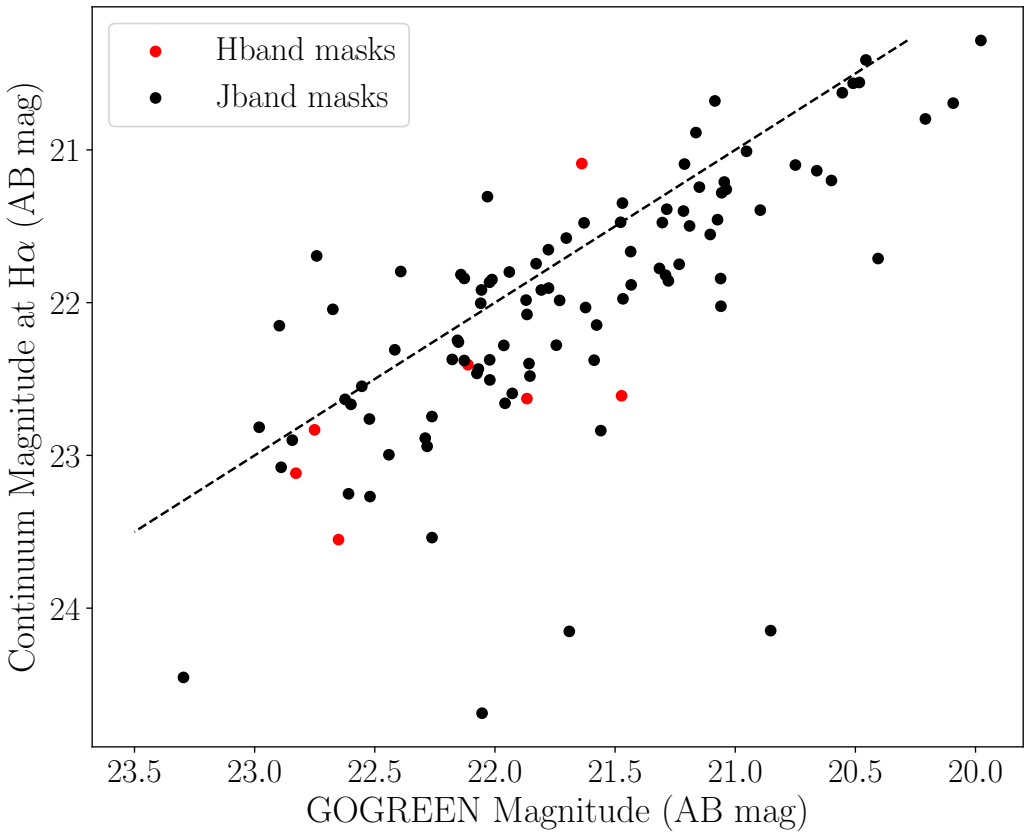


Figure B.1: We show our continuum magnitudes at $H\alpha$ measured directly from the spectra as a function of broad-band total magnitudes from GOGREEN. The points in red correspond to galaxies with Hα lies in the H-band. On the x-axis is the corresponding H-band magnitude for these points, while the rest of the points in black we use the corresponding J-band magnitudes. GOGREEN does not have H-band magnitudes, so we converted to H-band by fitting a line to a colour-colour diagram ($H_{grism} - J_{grism}$ vs $J_{grism} - K_{GG}$ and using the J and K magnitudes of GOGREEN to predict the H-magnitude. Dashed line is the 1-to-1 line. The continuum flux (c_D) was calculated using the linear MCMC fit of the continuum around Hα, and converted to an AB magnitude. When excluding the extreme outliers, the ground-based magnitudes from GOGREEN are systematically ~ 0.20 magnitudes larger than the continuum magnitudes measured at Hα with a scatter of $\sigma = 0.366$. We attribute this difference to the effect of our bright emission lines within the transmission window of the filters used for the ground-based magnitudes. In other words, because Hα is extremely bright compared to the continuum, this would inflate the magnitudes such that the broadband magnitude is larger than our magnitudes calculated using the continuum flux at Hα.

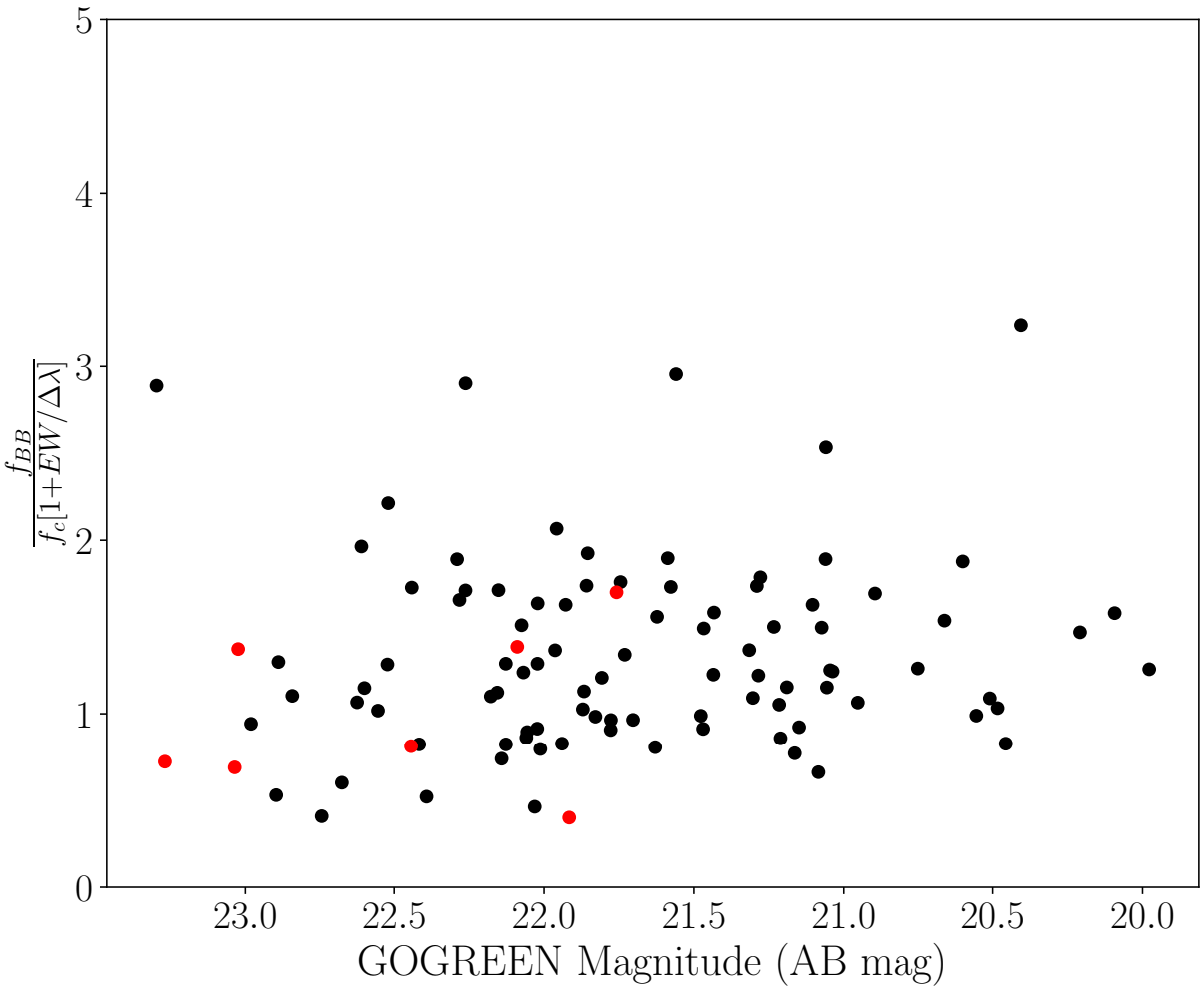


Figure B.2: We show our continuum flux correction factor as a function of broadband magnitude. The mean continuum correction factor is $\beta_c = 1.32$ with a standard deviation about this mean of $\sigma = 0.53$. We interpret this correction as the contribution from the large flux added to the broadband magnitude by the Hα emission line and therefore scale by a factor of $1/(1 + EW/\Delta\lambda)$. We show $f_{BB}/f_c(1 + EW/\Delta\lambda)$ on the y-axis, which should be scattered around 1 if this is the only correction needed. We decide to apply the mean correction factor to every galaxy, which will shift our equivalent widths down by a factor of $1/\beta_c$.

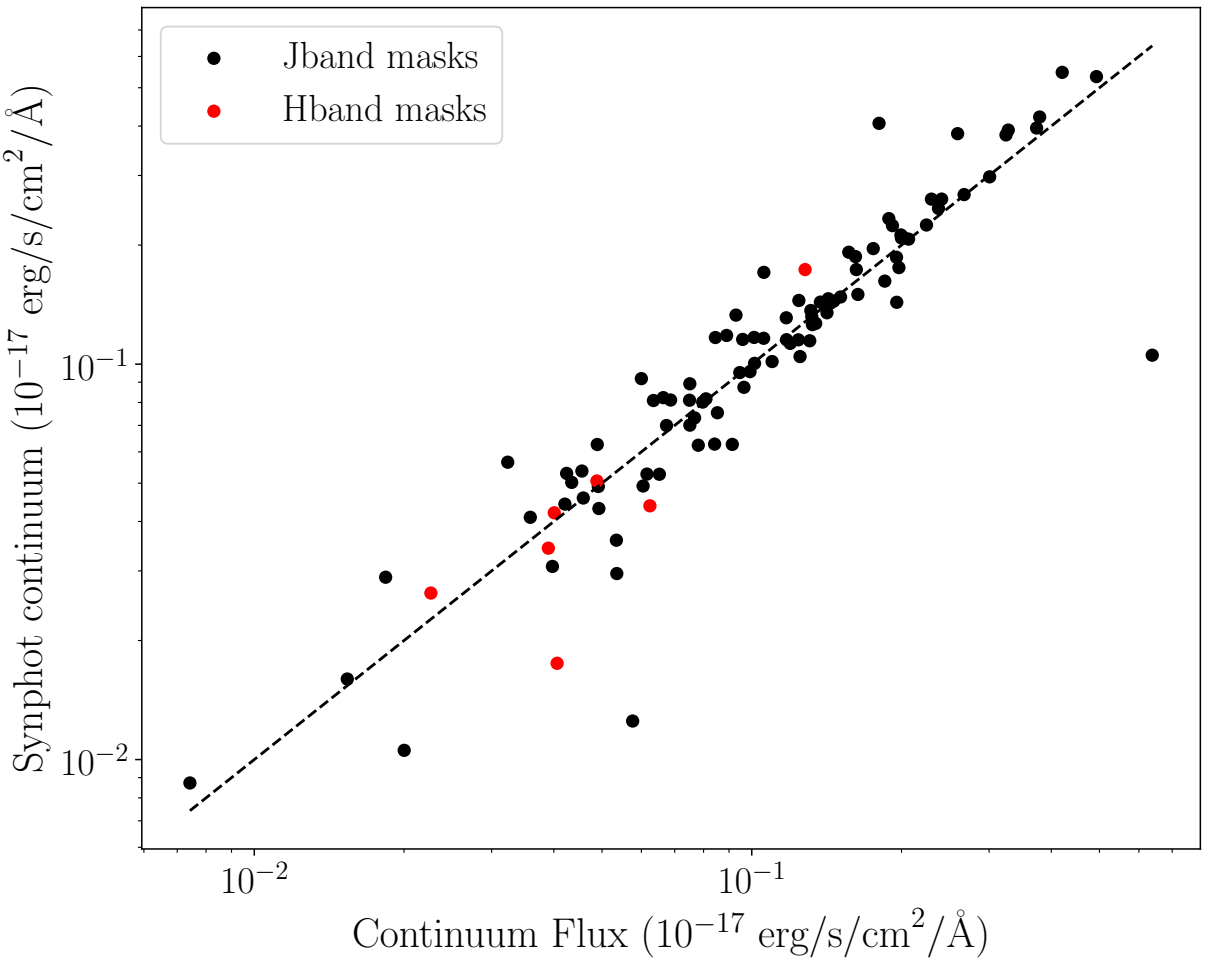


Figure B.3: We experimented with various methods of measuring the continuum. This plot shows the broad-band continuum estimated with *synphot* compared with the continuum fit at Hα we obtain from MCMC (Figure B.1) For spectra with large skyline residuals or other systematic uncertainties, *synphot* produced larger deviations from the photometric magnitudes. However, for the objects that were successful with *synphot*, the measurements were consistent between the methods, as demonstrated with the strong correlation in this plot, with a scatter of $\sigma = 0.15$.

B.2 Flux and EW Corrections

While these corrections apply to the stellar continuum, the same correction may not necessarily hold for line fluxes, which originate from star forming regions. To calculate the scale of this correction, we compare our measurements of $H\alpha$+[N II] with the overlapping grism observations from [94]. We derive an average flux correction factor, $\bar{\beta}_{H\alpha} = 1.52$, which is then applied to all of our line fluxes. We scale our equivalent widths in Equation 2.4 by $\beta_{H\alpha}/\beta_c = 1.16$. The following plots show the uncorrected fluxes followed by the corrected fluxes and the same for the equivalent widths.

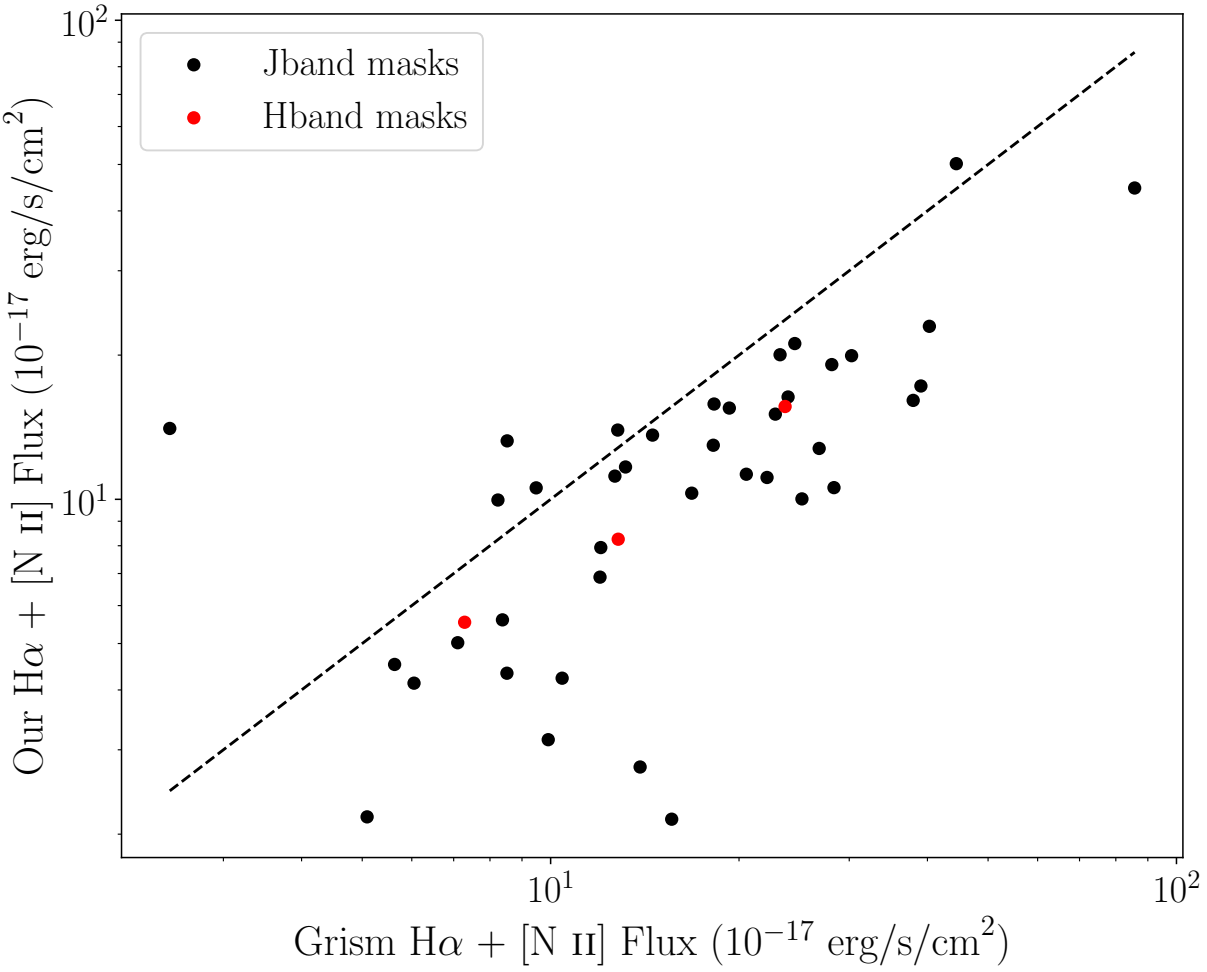


Figure B.4: When comparing our Hα+[N II] fluxes with the Grism sample from [94] for duplicate objects, our flux is lower. We interpret this as an aperture effect.On average, the fluxes from [94] are higher by factor of $\bar{\beta}_{H\alpha} = 1.52$, or ~ 0.5 mag. The scatter is $\sigma = 0.242$.

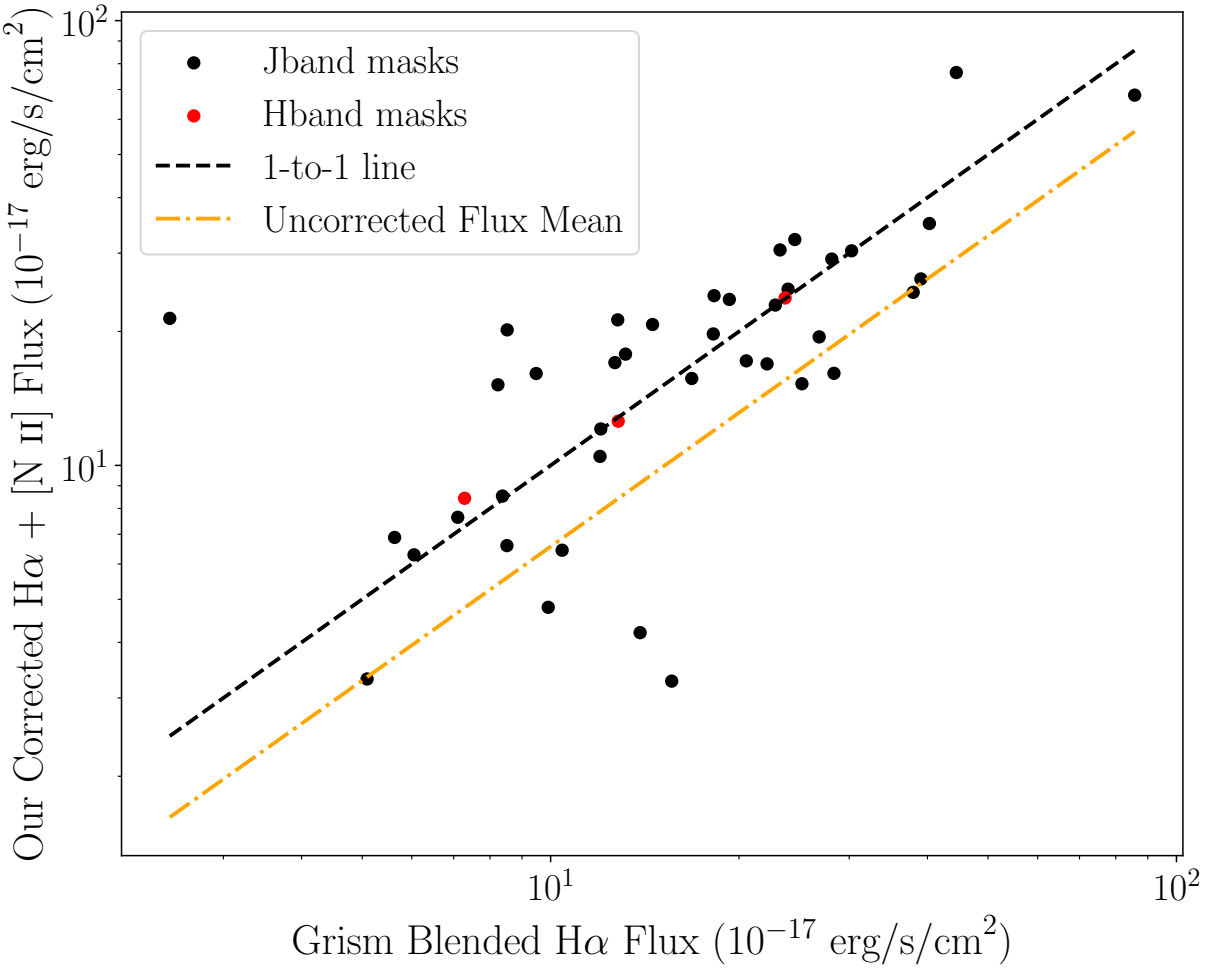


Figure B.5: Our Hα+[N II] line flux is shown after applying the flux aperture correction as a function of blended line flux from the HST grism data.We multiply our fluxes by $\bar{\beta}_{H\alpha} = 1.52$ to scale our fluxes to match that of the HST Grism fluxes. By definition, the difference in the means is now zero, while the scatter is unchanged. We show an orange line to indicate the old mean of the fluxes, while the 1-to-1 line is the new mean after applying corrections.

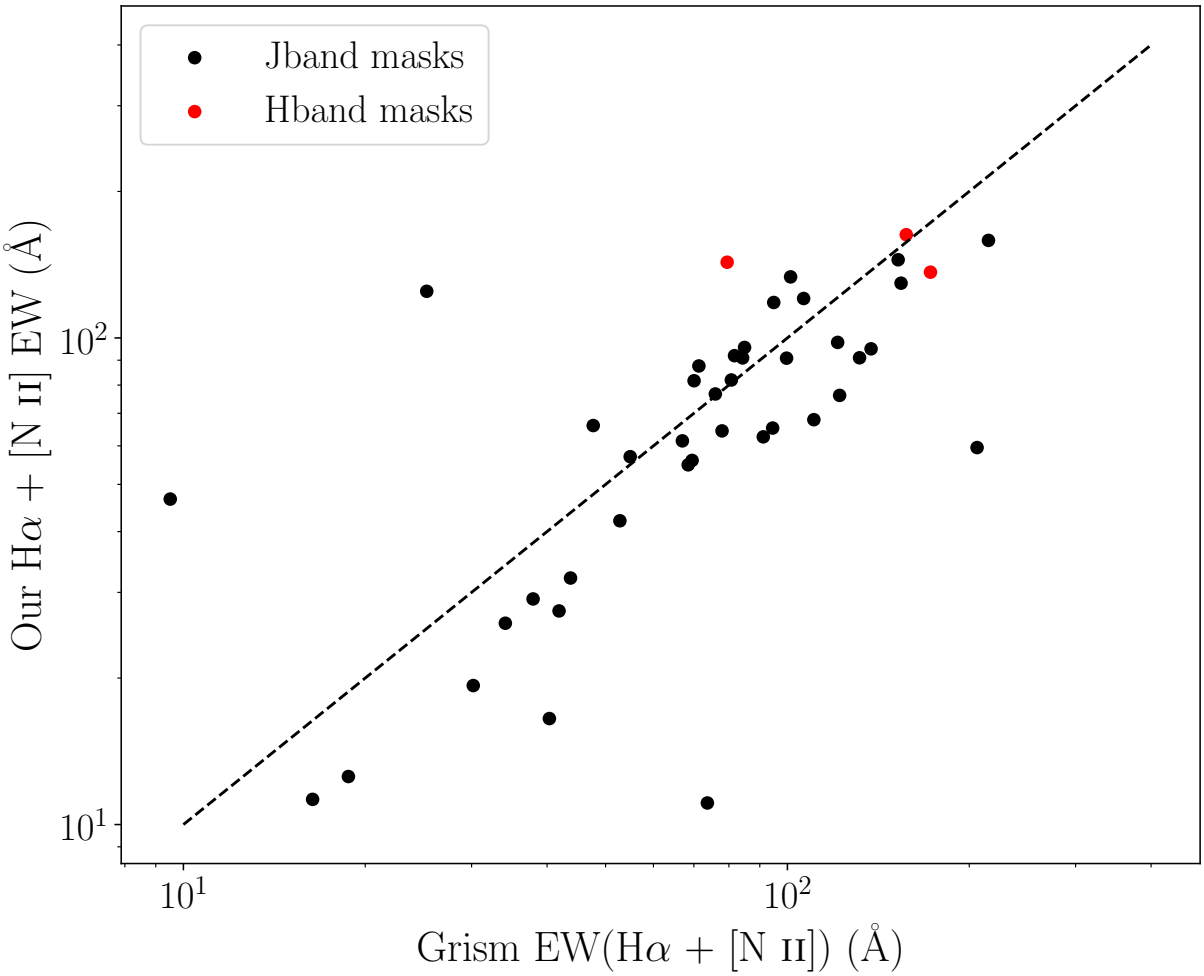


Figure B.6: Our observed Hα+[N II] equivalent widths (uncorrected for any aperture effects) are lower than those measured from the HST grism data by a factor of $\bar{\beta}_{EW} = 1.16$ (without excluding outliers). Since Figure B.4 shows our slit-based line fluxes would need to be multiplied by an average factor of $\bar{\beta}_{H\alpha} = 1.52$, this implies that the aperture correction is larger enough to correct for this offset, potentially with some slight over correction. With the outliers included, we measure a dispersion of $\sigma = 0.248$.

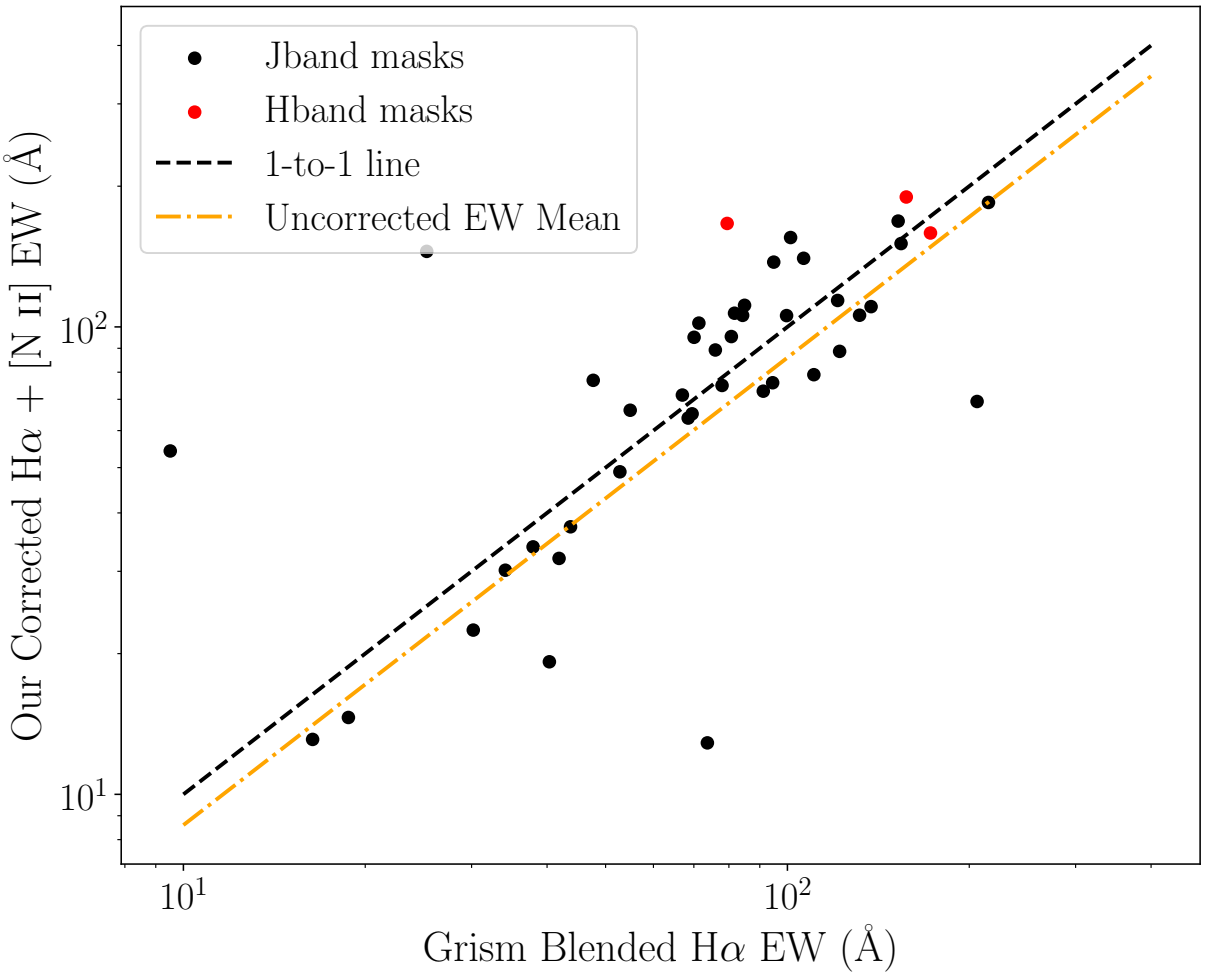


Figure B.7: We show our measured equivalent width after applying the continuum corrections and the flux corrections to our data. We multiply by $\bar{\beta}_{H\alpha}/\beta_c$ which shifts our equivalent widths up to closely align with the 1-to-1 line against the equivalent widths from [94].